Universita' degli Studi di Napoli Federico II,
Italy Dipartimento di Fisica "Ettore Pancini"
Research Doctorate (PhD) in Experimental
Particle Physics XXXIII Cycle

Real-time monitoring and diagnostics of crystal-based collimation of particle accelerator beams

Supervisors:
Prof. Pasquale Arpaia
Prof. Giovanni La Rana

PHD Candidate:
Zahoor ul Islam
2018-2021

PhD Coordinator:
Prof. Salvatore Capozziello

In the name of Allah, The Most Gracious and The Most Merciful

All praise is due to Allah, Lord of the worlds

The Entirely Merciful, the Especially Merciful

◆

O Allah, let Your Blessings come upon the Prophet Muhammad (Peace Be Upon Him) and the family of The Prophet Muhammad (Peace Be Upon Him), as you have blessed Ibrahim and his family. Truly, You are Praiseworthy and Glorious. Allah, bless the Prophet Muhammad and the family of the Prophet Muhammad, as you have blessed Ibrahim and his family. Truly, You are Praiseworthy and Glorious.

Dedicated to:

My Father Ain ud Din, and
to.........
The Shine of happiness in his eyes at the moment that he heard my birth news...

Special Thanks to:

Guido Celentano,
For his regular help and support, you made it possible "Boss"

Abstract

The beam collimation represents one of the important items for the future upgrade of the Large Hadron Collider (LHC) at CERN. An effective collimation system is particularly required at higher beam intensities, as even a relatively small number of particles impinging on the superconducting magnets can cause quenching (a sudden loss of superconducting condition). Although the currently used collimation system at CERN is working properly, it presents some limitations which can be overcome by future upgrades. One of these limitations is due the particle diffraction from heavy absorbers.

An alternative option to the current collimation system at CERN is represented by the use of bent crystals. These latter are expected to be very effective in beam collimation. In fact, they have the advantage to guide halo particles of the beam on a single absorber. This allows the improvements to the cleaning performance as well as to the impedance of the collider as compared to the multi-stage collimation systems, consisting of large blocks made of amorphous material, placed around the beam. In this framework, UA9 Experiment at CERN is carrying on since many years an R&D on various types of crystals. The aim is to find the best solution to overcome the limitations of the currently used collimation system at CERN, in view of future upgrades of the collider. The first part of this PhD work has been devoted, within the UA9 collaboration, to the characterization of some new crystals to be used in LHC and in the Super Proton Synchrotron (SPS) for collimation. The radiation hardness for high energy neutrons were also tested for these crystals.

Beam collimation monitoring is performed in the UA9 crystal based system using a Cherenkov detector for high energy protons going through the fused silica. Presently, classical PMTs are in use to collect the Cherenkov light, but its dark count rate is directly affected by the high intensity radiation. With the aim to face this limitation, the second part of this PhD project focused on the characterization of ZnO material, which resulted to be very promising for realizing alternative photodetectors. In this respect, Cherenkov detector/setup used in UA9 could be updated with more functional sensor systems which are radiation resistant and compatible with vacuum requirements in the beam pipe.

Another important aspect in collimation systems is the real time monitoring of collimated beams inside the accelerators, especially when using a crystal based collimation system as in UA9. A

good approach to face this aspect is to develop a machine learning based real time framework to analyze the signal and detect the faults. The last aim of this work is to present a preliminary study of data acquisition as a starting point to develop a real time framework to be built in the future. This work has been carried out using a SiPM sensor (which competes with the PMTs) with a fast ADC digitizer in real time.

List of Abbreviation & Acronyms

LHC	Large Hadron Collider
SPS	Super Proton Synchrotron
UA9	Underground Area 9
CpFM	Cherenkov Proton Flux Monitor
BCT	Beam Current Transformer
BTF	Beam Test Facility
PMT	Photomultipliers Tubes
SiPM	Silicon Photomultiplier
PDE	Photon Detection Efficiency
ZnO	Zinc Oxide
ADC	Analog to Digital Conversion
LSS5	Long Straight Section 5
MAPD	Micropixel Avalanche Photo Diodes
MPPC	Micro-Pixel Photon Counters
APD	Avalanche photodiode
DCR	Dark Count Rate
ICR	Input Count Rate
OCR	Output Count Rate
PSD	Pulse Shape Discrimination
CFD	Constant Fraction Discrimination
DC	Dechanneling
VC	Volume Capture
VR	Volume reflection

List of Figures

List of Tables

Table of Contents

INTRODUCTION AND OUTLINE

It is due to atomic potential that charged particles impinging on crystals having a small angle to the lattice planes are enforced to go between the planes of crystal. The trapped particles follow the bending path in bent crystals and are deflected correspondingly, practicing the planar channeling effect. Hence, using bent crystals as primary collimators have changed the pattern as compared to the current multi-stage-collimation system, in which about 1 MJ beam is lost by massive blocks of the primary collimator and scattered out on the secondary collimators (made also of massive blocks of nebulous material). In crystal-based collimation, the main (primary) collimators are replaced by bent crystals used to steer halo particles on top of only one targeted block, enhancing the beam cleaning with less impedance than the multi-stage collimation system presently used.

UA9 Experiment at CERN SPS is working on crystal collimation using the areas assigned in LSS5 (Long Straight Section 5) and H8 beam lines. The main work of this thesis has been carried out in the framework of UA9 experiment. In particular, this dissertation focuses on three main aspects: (i) characterization of Silicon crystals for beam collimation (ii) Tests of ZnO based photo detectors to be used in radiation hard environment and finally (iii) SiPM (silicon photomultiplier) signal analysis, this sensor being an alternative of classical PMTs for upgrading of the Cherenkov detector.

An introductory view about accelerator physics is given in **Chapter 1**. This includes fundamental physics & methods of the machine operation that is useful to introduce some basic aspects related to this work. In particular, the SPS is treated in more details as UA9 collaboration has long experimental section in this machine.

A summary of the major theories and concepts of charged particles channeling in crystals are described in **Chapter 2**. The concept that proper directions inside the crystal can be extra transparent to the particles as compared to any amorphous material was first introduced by Stark [1]. In this chapter we illustrate the basic physics behind crystal channeling for collimation. In the **Chapter 3** we described UA9 Experiment at CERN devoted to the study of beam collimation by crystals. In this chapter are also described the results coming from the tests of some crystals irradiated by high intensity flux of neutrons and then characterized for collimation.

One of the important parts of this PhD work is the characterization of some crystals in UA9 Experiment which is discussed in **Chapter 4** in detail. In this chapter, crystals characterization and testing techniques and its results are given which described that before being used at the SPS or LHC accelerators, how each crystal checked many times to verify the stability of the deflection angle and other characterizing parameters in time, and after heating (baking). These tests are performed at H8 beam line using protons, pions or ion beams with several energies.

In **Chapter 5** we present the working principles of the Cherenkov Proton Flux Monitor (CpFM) in detail, it also worth noting that our main work in addition to the characterization of various types of crystals is to improve the performance of CpFM with SiPM as an alternative option for PMTs currently in used. In **Chapter 6,** the alpha and gamma radiation effects on ZnO material based Photodetectors are described; in particular, these sensors have been tested to check their working ability in high radiation environment. The results of these measurements are presented in this chapter.

Finally, **Chapter 7** is devoted to the analysis and measurements of signals recorded by a commercial Silicon Photomultipliers (SiPM). The main purpose of the work is to start making a ground for the development of a real time monitoring framework for Cherenkov detectors.

Chapter 1

ACCELERATOR PHYSICS

In this chapter, the physics of synchrotron accelerator at basic level is described; this work being related to SPS and LHC at CERN. Comprehensive information about physics of accelerators can be found in "*The Physics of Particle Accelerators"*[2].

1.1. Transverse Beam Dynamics

1.1.1. Equation of motion

The essential issues that need to be faced to produce and accelerate particles are:

i. How to maintain a particle inside the beam pipe
ii. Boosting particles energy
iii. Storage of the beam for long time

These questions have a best solution in the form of strong focusing synchrotrons, which consist of accelerating resonant cavities, dipole and quadrupole magnets. The dipole magnet is used to deflect particles trajectory to maintain it on a circular/round path. The exact orbit of the particle is identified as reference path or designed orbit and all other coordinates of particles inside the beam are considered from these reference particles (given in Figure: 1.1). The quadrupole magnetic field is used to manage the beam size and divergence. Principally, one quadrupole magnet get centralized particle beam in a specific plane like XS for example and decentralizes in the other orthogonal plane (YS). To maintain the high-energy particles beam with no increase in its cross-section for long distance and time, a set of both the focusing & defocusing magnets is required, which will make a structure of FODO cell [30], which represents the main elementary accelerator lattice. For the purpose to accelerate the particles, Resonant cavities are used which also compensate for the energy losses occurring because of the synchrotron radiation inside the machine.

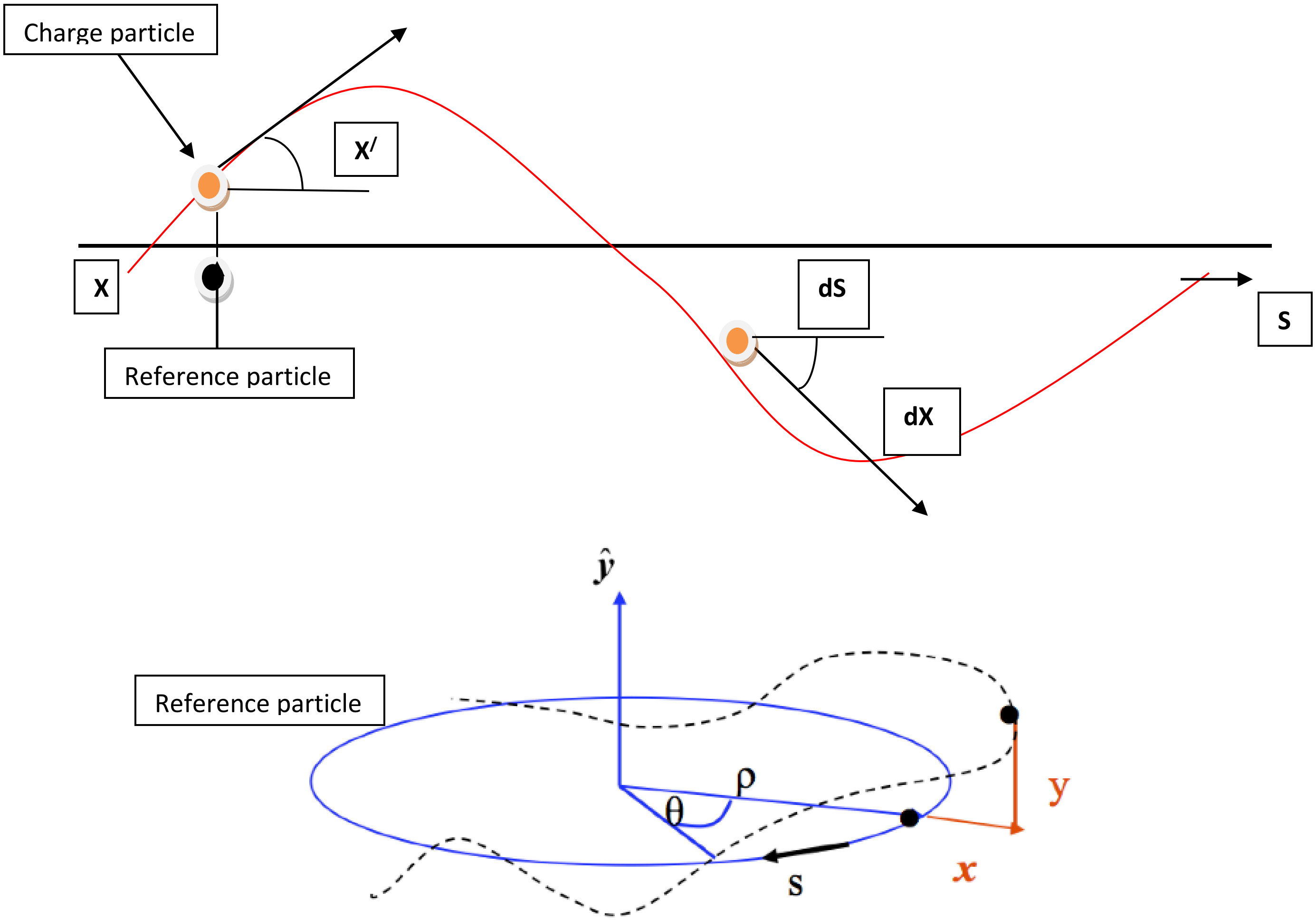

Figure: 1. 1 The sketch of Particle coordinates in circular machine.

Using Maxwell's equations let us write down the equation of particles motion inside the accelerator magnetic system. The reference system shown in Figure: 1.1 can be chosen. The situation of a particle is hereby given with six dimensional phase-space-vector: $(x, x', y, y', s, \delta)$, and (see fig 1.1) x, y represent transverse coordinates with respect to the mentioned reference particle, longitudinal position is given by s for the particle on the reference orbit, the transverse angles are $x' = dx/ds$ & $y' = dy/ds$, $\delta = (p - p_0)/p_0 = \Delta p/p_0$ is the momentum offset (relative) considering a total momentum "p" of the particle and the reference momentum given by $p_0 = m_0 v_0 \gamma$. To fix reference particle route we can consider the Lorentz force, acting on the particle with charge e, having velocity $\vec{v}$:

$$\vec{F} = e\left(\vec{E} + \vec{v} \times \vec{B}\right) = \frac{d\vec{p}}{dt}. \tag{1.1}$$

Assuming relativistic particle, if **E = cB,** then **E** (electric field) & **B** (magnetic field) will provide an equal outcome. Therefore, because of the easy production of **B** of about 1 T as compared to the equivalent E of about 3 x 10^8 V/m, magnetic field is the best option to be used for beam steering in the new accelerators. Hence, ignoring **E** and rewriting the Eq. 1.1 in the shown reference frame (in Figure: 1. **1**) we obtain:

$$\frac{d^2\vec{r}}{dt^2} = \frac{e}{m}\left(\frac{d\vec{r}}{dt} \times \vec{B}\right) \tag{1.2}$$

The general derivation to solve equation 1.2 in detail is given in Appendix A. Beam rigidity is another important parameter of particle accelerator, given by:

$$R = B.\rho = \frac{p}{q} \tag{1.3}$$

where ρ denotes orbit's bending radius because of given dipole magnetic field, p is the momentum and q represents charge of particle. In Eq 1.3 can be written in a more convenient way for single charge as follows:

$$R = B[T].\rho[m] \cong \frac{p[\frac{GeV}{c}]}{0.3} \tag{1.4}$$

Equation 1.4 gives the relation between the maximum particle momentum and the magnetic field of the machine. As an example, for particle of 7000 GeV/c momentum and 8.3 T of magnetic field is required in LHC with a value of ρ = 2800 m.

General solution of equation 1.2 can be seen in Appendix A and in [2] in more detail, but for quadrupole magnets and dipole magnets (linear machine), particle coordinates in transverse planes can be written as:

$$x''(s) + \left(\frac{1}{R^2(s)} - k(s)\right) \mathrm{x}(s) = \frac{1}{R(s)}\frac{\Delta p}{p} \tag{1.5}$$

$$y''(\mathrm{s}) + \mathrm{k(s)y(s)} = 0 \tag{1.6}$$

Equations 1.5 & 1.6 describing the magnetic fields use the energy invariant dipole power 1/R(s) and quadrupole strength k(s). Supposing a reference particle (for which Δp/p = 0) the factor (1/R(s))(Δp/p) becomes zero in Eq. 1.5 and the equations are then called "Hill's differential equations" of motion. The path functions x(s) & y(s) illustrates the transverse oscillation in the orbit, which is called betatron oscillation [2].

1.1.2. Twiss Parameters

The general solution for particle ($\left(\frac{\Delta p}{p} = 0\right) reference\ particle$) route is given by,

$$x(s) = A\sqrt{\beta_s}\cos(\emptyset_x(s) + \emptyset_0) \tag{1.7}$$

It is applicable for xy plane (Figure: 1.1), here β(s) represents an amplitude function of betatron oscillation, ϕ(s) denotes a phase advance and is given by:

$$\emptyset(s) = \int_0^s \frac{d\sigma}{\beta_x \sigma} \tag{1.8}$$

We can also introduce other two parameters:

$$\propto_x (s) = -\frac{\beta'(s)}{2} \tag{1.9}$$

$$\gamma_x (s) = \frac{1 + \alpha_x^2(s)}{\beta_x(s)} \tag{1.10}$$

The relation 1.9 and 1.10 together with β(s), describe Twiss or Courant-Snyder parameters. The amplitude factor A in Eq. 1.7 can be replaced by emittance (√ε). The equation of motion with the Twiss Parameters can be written as:

$$x(s) = \sqrt{\varepsilon}\sqrt{\beta_s}\cos(\emptyset_x(s) + \emptyset_0) \tag{1.11}$$

$$x'(s) = -\frac{\sqrt{\varepsilon}}{\sqrt{\beta_s}}[\alpha(s)\cos(\emptyset_x(s) + \emptyset_0)\ \sin(\emptyset_x(s) + \emptyset_0)] \tag{1.12}$$

For explaining the particle motion in the phase space x-x' (shown in Figure: 1.2), we eliminate the phase $\emptyset_x$ terms and we obtain a general equation of an ellipse in this plane (x- x'):

$$\gamma(s)x^2(s) + 2\,\alpha(s)x(s)x'(s) + \beta(s)x'^2(s) = \varepsilon \tag{1.13}$$

Here "ε" has the definite meaning of the Courant-Snyder invariant of action. This provides the parametric equation of the ellipse in the x – x' space, where the ellipse shape and the orientation are represented by Twiss parameters (α, β & γ). The **"π . ε"**, is the area of the ellipse which is an inherited parameter of the beam and can't be altered by the focal property.

For the calculation of beam envelope size one can statistically suppose entire Beam emittance **ε_b**, which has a Gaussian distribution in transverse plane:

$$\sigma_x(s) = \sqrt{\varepsilon_b \beta_x(s)} \tag{1.14}$$

$$\sigma_x'(s) = \sqrt{\varepsilon_b \gamma_x(s)} \tag{1.15}$$

here $\sigma_x(s)$ is the standard deviation (RMS or STD) of the betatron and $\sigma_x'(s)$ is the divergence of the beam,

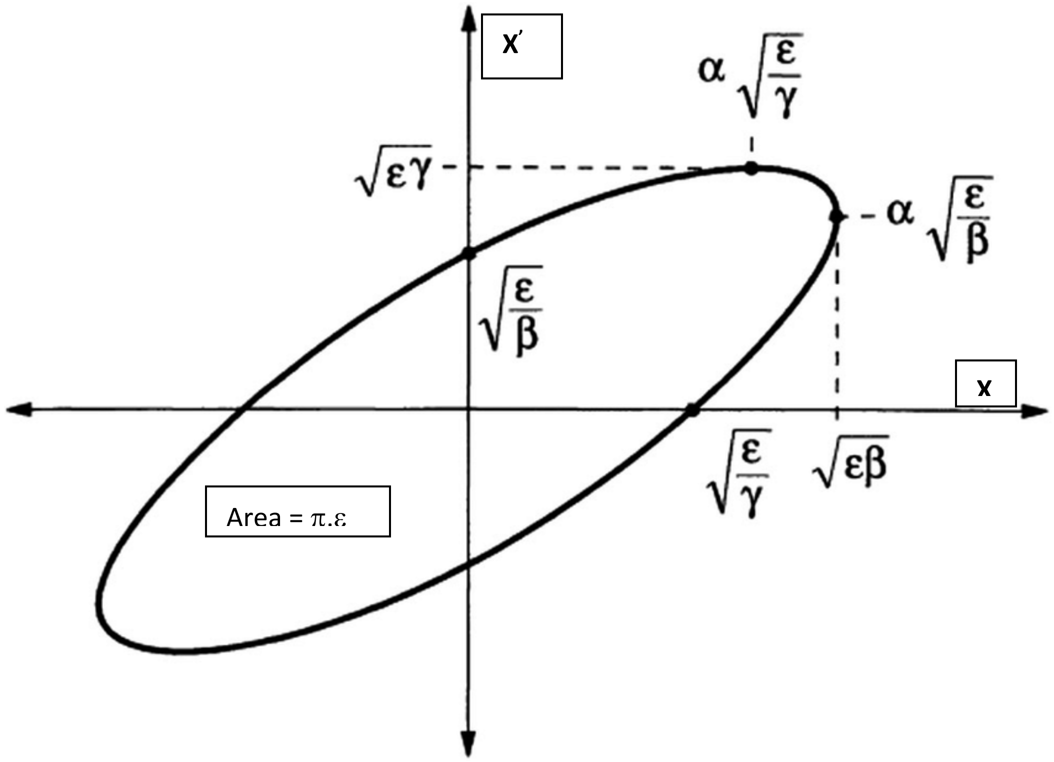

Figure: 1. 2 Particle Motion Phase space ellipse in the x – x' [2]

1.1.3. Accelerator Tune

In circular accelerators, each turn of particle beam passes through the similar magnet lattice. We have to consider, that any flaw can cause particle instability in the machine, for example, quadrupole fields may increase the amplitude of oscillations of particle causing an increment in the size of the beam (transversely) in every rotation and finally resulting to beam losses. This event is called “optical resonance”. Optical resonance strongly depends on the betatron phase, in one entire revolution of particle we have: $\Delta\emptyset = \emptyset(s+L) - \emptyset(s)$ where L represents circumference length of the accelerator. As a result we describe the accelerator’s tune “Q” as following:

$$Q = \frac{\Delta\emptyset}{2\pi} = \frac{1}{2\pi}\int_0^L \frac{ds}{\beta(s)} = \frac{1}{2\pi}\oint \frac{ds}{\beta(s)} \tag{1.16}$$

Q represents the number of betatron oscillations done by particle in one complete turn. An integer value of Q indicates dipole field error while a small rational number ½ and 1/3 may indicates beam instability because of resonant oscillator circumstances, quadrupole and sextupole fields respectively. The limited mechanical strength and the magnets finite pole size imply that the previously faults due the multipole fields can be present in the accelerator. Consequently, here are resonances at mQ = p all the time, where m and p are integers. It must be kept in mind that all accelerators have Q_x and Q_y values of tune, in horizontal plane and vertical plane respectively. Generally, these values are not similar; therefore in these planes there are resonance circumstances. The strength of this latter in one plane depends on the position of beam in the other plane (for higher multipole fields), which results to the coupling among the betatron oscillations in both planes and also to the coupling with the resonances. In such planes the condition for optical resonance may hence be given as follow:

$$\mathrm{mQx} + \mathrm{nQy} = \mathrm{p} \text{ (m, n and p are integers)} \tag{1.17}$$

Here in 1.17, the sum of |m| and |n| is known as resonance order. In support of stable processes, a couple of appropriate values of Q_x & Q_y have to be selected to avoid optical resonances. This pair of values constitutes the working point. Power of the resonance decreases rapidly with the order, hence selecting a working point one should normally pay attention to resonances up to (about) 5th order.”[2]

1.1.4. Transfer Matrix Formalism

To describe the motion of particles inside the accelerator we can use a matrix formalism which is based on the Twiss-parameters. We can find the transverse position of particle at some point on orbit s_2 from any other position of the machine s_1, with the help of transfer matrix $M(s_1|s_2)$:

$$\begin{pmatrix} x(s_2) \\ x'(s_2) \end{pmatrix} = M(s_1|s_2) \begin{pmatrix} x(s_1) \\ x'(s_1) \end{pmatrix} \tag{1.18}$$

To derive the matrix $M(s_1|s_2)$, we start from general path/trajectory solution (Eq 3.7) given as follow:

$$x(s) = a\sqrt{\beta_x(s)}\,\sin(\emptyset_x(s)) + b\sqrt{\beta_x(s)}\,\cos(\emptyset_x(s)) \tag{1.19}$$

Assuming that coordinates at s_1 are given, then:

$$a = x(s_1)\left[\frac{\sin(\emptyset_x(s_1)) + \alpha_x(s_1)\cos(\emptyset_x(s_1))}{\sqrt{\beta_x(s_1)}}\right] + x'(s_1)\sqrt{\beta_x(s_1)}\,\cos(\emptyset_x(s_1)) \tag{1.20}$$

$$b = x(s_1)\left[\frac{\cos(\emptyset_x(s_1)) - \alpha_x(s_1)\sin(\emptyset_x(s_1))}{\sqrt{\beta_x(s_1)}}\right] - x'(s_1)\sqrt{\beta_x(s_1)}\,\sin(\emptyset_x(s_1)) \tag{1.21}$$

Putting the eq 1.19/1.21 in Eq: 1.18 the transform matrix for the assessment of particle coordinate at S_2 can be obtained:

$$M(s_1|s_2) = \begin{pmatrix} \sqrt{\frac{\beta_2}{\beta_1}}\,(\cos(\emptyset_{21}) + \alpha_1\sin(\emptyset_{21})) & \sqrt{\beta_2\beta_1}\,\sin(\emptyset_{21}) \\ -\frac{1+\alpha_1\alpha_2}{\sqrt{\beta_2\beta_1}}\sin(\emptyset_{21}) + \frac{\alpha_1-\alpha_2}{\sqrt{\beta_2\beta_1}}\cos(\emptyset_{21}) & \sqrt{\frac{\beta_1}{\beta_2}}\,(\cos(\emptyset_{21}) - \alpha_2\sin(\emptyset_{21})) \end{pmatrix} \tag{1.22}$$

where $\emptyset_{21} = \emptyset_2 - \emptyset_1$ is the phase advance between spot s_2 and s_1, $\beta_i = \beta_x(s_i)$, $\alpha_i = \alpha_x(s_i)$ and $\emptyset_i = \emptyset_x(s_i)$ (with i equals to 1, 2). By means of the acquired transfer matrix it is possible to calculate the particle coordinates in any place along the machine, if Twiss-parameters are given:

$$M(s_k|s_m) = \prod_{i=0}^{k-m-l} M(s_{k-i}|s_{k-i-1}) \tag{1.23}$$

To compute the deflected particle trajectory (by crystal) at S_1, one can estimate the kick θ for particle as following:

$$\begin{pmatrix} x(s_1) \\ x'(s_1) \end{pmatrix} = \begin{pmatrix} x(s_1) \\ x'(s_1) + \theta \end{pmatrix} \tag{1.24}$$

Hence the transverse coordinate of particle at any place s_2, once the crystal kicked, is given as following:

$$x(s_2) = \sqrt{\frac{\beta_2}{\beta_1}}\,(\cos(\emptyset_{21}) + \alpha_1 \sin(\emptyset_{21}))x(s_1) + \sqrt{\beta_2\beta_1}\,\sin(\emptyset_{21})\,(x'(s_1) + \theta) \tag{1.25}$$

Using the equation Eq. 1.25, it is possible to work out the kick on s_1 of deflected beam for specified coordinate $x(s_2)$ in the machine:

$$\theta = \frac{1}{\sqrt{\beta_2\beta_1}\,\sin(\emptyset_{21})}\left(x_2 - \sqrt{\frac{\beta_2}{\beta_1}}\,(\cos(\emptyset_{21}) + \alpha_1 \sin(\emptyset_{21}))x_1 - \sqrt{\beta_2\beta_1}\,\sin(\emptyset_{21})\,x_1'\right) \tag{1.26}$$

1.2. Longitudinal beam dynamics

As it is discussed above, the resonant cavities pay compensation to the energy losses (produced by synchrotron radiation) and also accelerate the energy ramp of particles in the apparatus. The RF cavities potential is sinusoidal with the frequency which is proportional to the revolution frequency of the machine. The role of this potential is to generate stable region in the beam which is called "bucket". Within each bucket particles produce bunches. Particle energy gain in every turn through the RF cavities is given by:

$$\Delta E = qV_{RF}\sin(\emptyset(t)) \tag{1.27}$$

In equation 1.27 $\emptyset(t)$ is the "relative phase" between RF and particle with q charge, V_{RF} represents maximum RF potential. For the particles with exact energy ($\emptyset(t) = \pi n$; n = 0, 1, 2…) RF field doesn't operate while for off-momentum particles which have (i.e $\emptyset(t) \neq \pi n$,), the energy gets increased and decreased in each passage. This motion of particles is actually synchrotron motion. This phenomenon is illustrated in Figure: 1.3.

Hence, for particle's acceleration to be in the RF cavity with $0 < \phi < \pi/2$, the relativistic effect is given by,

$$\Delta p = \frac{\Delta E}{c} \tag{1.28}$$

Due to momentum offset, the orbit variation is:

$$\frac{\Delta L}{L} = \alpha_c \frac{\Delta p}{p} \tag{1.29}$$

Where α_c is the “momentum-compaction factor”. Knowing that the revolution time decreases because of the shrinking of the particle’s trajectory and in parallel the revolution time will increase when the particles slow down under the increase in relativistic mass, we have a correlation linking orbit distance and a revolution frequency (phase-focusing) given by:

$$\frac{\Delta T}{T} = \left(\alpha_c - \frac{1}{\gamma^2}\right) \frac{\Delta p}{p} \tag{1.30}$$

In Eq 1.30 T denotes the revolution time period and γ represents the relativistic factor. The known gamma transition (γ_{tr}) factor which corresponds to $\frac{\Delta T}{T} = 0$ at any $\Delta p/p$ is defined as:

$$\gamma_{tr} = \sqrt{\frac{1}{\alpha_c}} \tag{1.31}$$

This situation $\frac{\Delta T}{T} = 0$ ought to be evaded, therefore gamma transition defines two regimes: for $\gamma < \gamma_{tr}$ ($\alpha_c - (\frac{1}{\gamma^2})$) <0) we have a regime when the particle has to enter in the RF with $0 < \phi < \pi/2$ and for $\gamma > \gamma_{tr}$ (i.e $\alpha_c - (\frac{1}{\gamma^2})$)>0) a different regime when the same particle has to enter with the values $\pi/2 < \phi < \pi$ (Figure: 1.3).

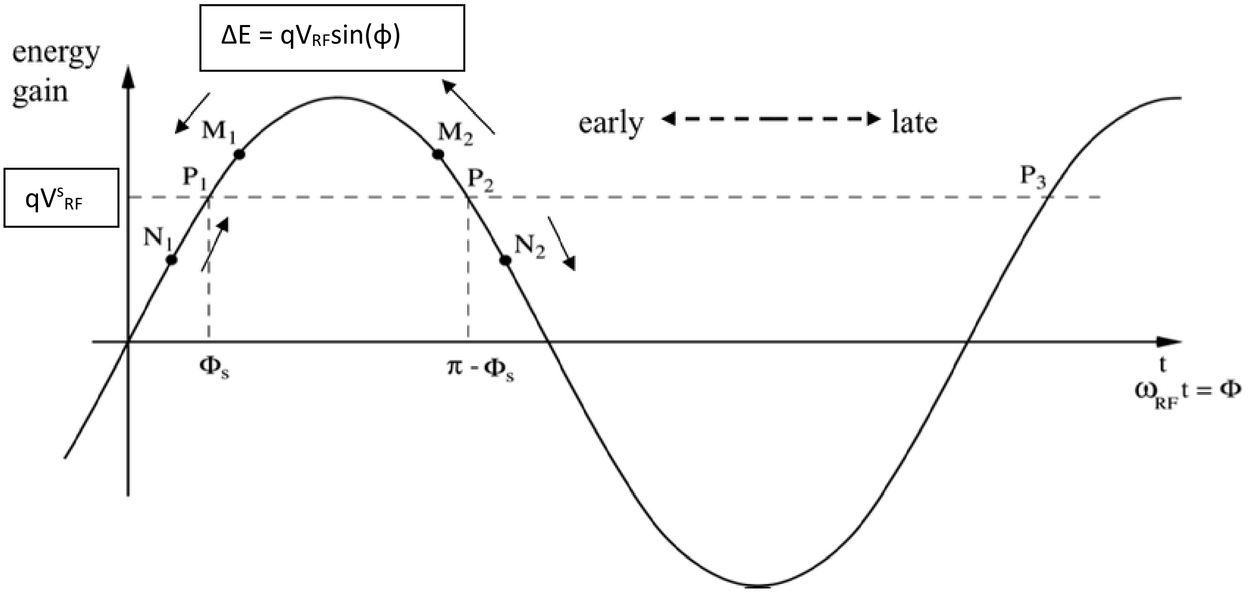

Figure: 1. 3 Design of the phase stability theory. Particle 1 is accelerated with high ΔE; bellow the $\boldsymbol{\gamma_{tr}}$ $\left(\boldsymbol{\frac{\Delta T}{T} = 0}\right)$, an increment in energy means an increment in revolution frequency; this particle arrives before – tends toward ϕs. Particle 2 is accelerated with low ΔE; decrease in energy means decrease in revolution frequency; this particle arrives afterward, (tends towards ϕs similarly to P1)

Now, let us suppose that the motion of energy oscillation in E - ϕ phase space is governed by the equation:

$$\ddot{\Phi} + \frac{\Omega_s^2}{\cos(\Phi_s)}(\sin(\Phi) - \sin(\Phi_s)) \tag{1.32}$$

where Ω_s is synchrotron angular frequency. multiplying the Eq. 1.32 by $\dot{\Phi}$ and after integration we obtain the invariant of motion [3].

$$\frac{\dot{\Phi}^2}{2} - \frac{\Omega_s^2}{\cos(\Phi_s)}(\cos(\Phi) + \Phi\sin(\Phi_s)) = const. \tag{1.33}$$

Therefore, we get harmonic energy oscillations about the ostensible value of a particle with very small value of Δp/p. In Figure: 1.4, stable and unstable regions in E – Φ phase space are shown graphically.

The stable section is known as “Separatrix” which defines the energy acceptance of the device, given by FWHM of the RF bucket:

$$\Delta E_b = k\sqrt{1 - \left(\frac{\pi}{2} - \varphi_s\right) tg(\varphi_s)} \tag{1.34}$$

k is constant in 1.34 , particle motion is usually not stable in the exterior of separatrix. Details about the longitudinal beam dynamics can be found in [3].

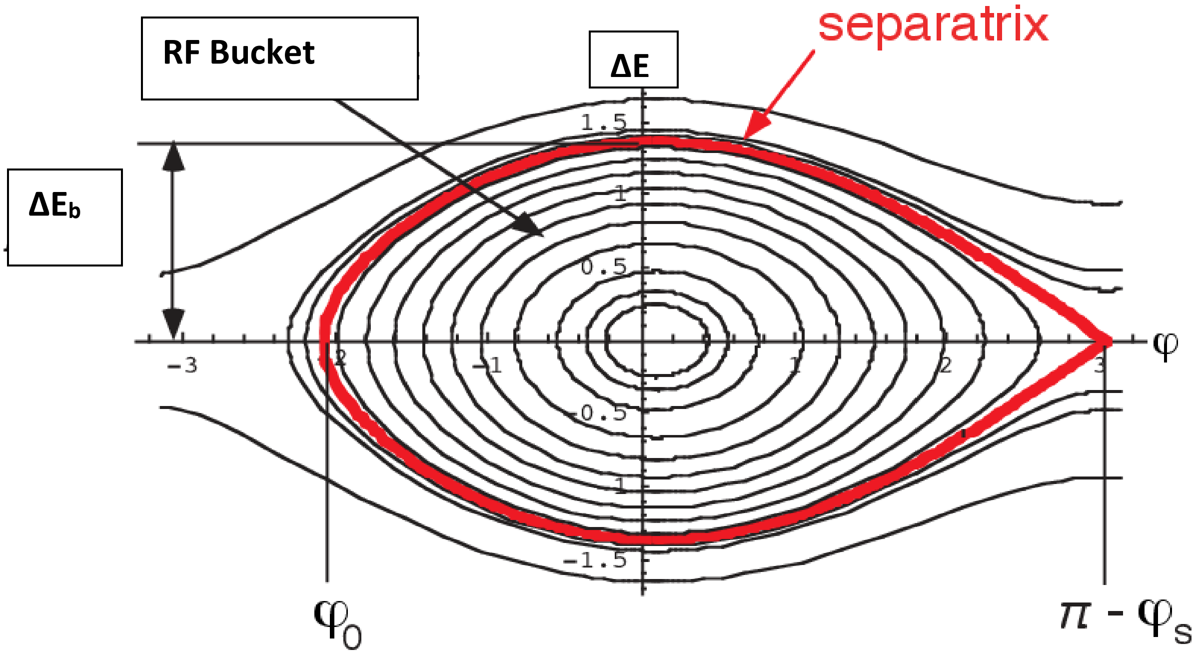

Figure: 1. 4 Stable phase space particle longitudinal routes. Red line indicates stable motion separatrix.

1.3. Dispersion

In this section a summarizing sketch of dispersion function and its influence on the particle path inside the circular machine is given. Until here, for only transverse beam dynamics we have focused on the monochromatic particle beam ($\Delta p = p - p_0 = 0$, momentum offset), which is not appropriate in real situations. There is little momentum spread among all particles ($\Delta p \neq 0$). Considering Eq. 1.3, Figure: 1.5 demonstrates the dipole field effect for two particles with different momentum taken from the reference momentum (p_0). The relationship in momentum and transverse position of particle is called dispersion, which represents the dipole magnet's intrinsic quality.

1.3.1. Solution of the inhomogeneous Hill's equation

The magnetic inflexibility as given (Eq.1.3), taking into consideration the particle momentum offset ($\delta = \Delta p/p_0$), can be written:

$$B\rho = \frac{p}{q} = \frac{p_0(1+\delta)}{q} = B\rho_0(1+\delta) \Rightarrow \rho = \rho_0(1+\delta) \qquad (1.35)$$

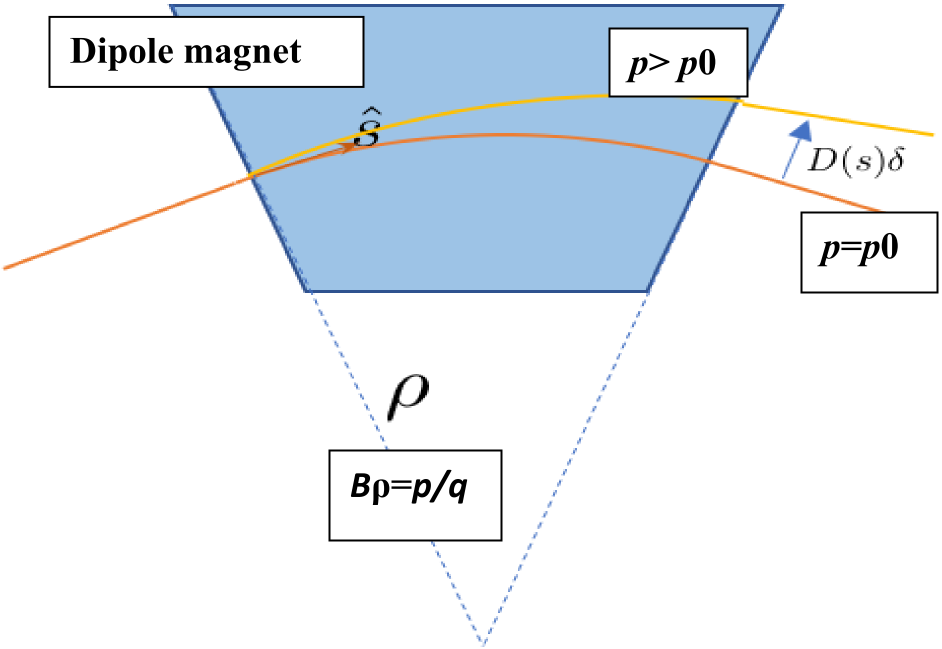

Figure: 1. 5 Dipole magnet Dispersion.

Equation 1.5 with ρ = R (s), is the inhomogeneous Hills equation, with a solution which can be written as following:

$$x(s) = x_\beta(s) + x_D(s) \tag{1.36}$$

where $x_D(s) = D(s)\frac{\Delta p}{p_0}$, $x_\beta(s)$ is the betatron amplitude for on-momentum particles with $\Delta p/p_0=0$, the dispersion function (D(s)) is a particular orbit where particle will have $\Delta p/p_0=1$. Therefore, $x_D(s)$ provides the deviation of new closed orbit for an off-momentum particle with a definite ΔP. To evaluate the D(s) it is essential to put Eq. 1.36 in Eq. 1.5. The Eq. 1.11 and Eq. 1.12 of the betatron are given as:

$$x(s) = \sqrt{\epsilon}\sqrt{\beta(s)}\,\cos(\varphi_x(s) + \varphi_0) + D(s)\frac{\Delta p}{p_0}, \tag{1.37}$$

$$x'(s) = -\frac{\sqrt{\epsilon}}{\sqrt{\beta(s)}}\left[\alpha(s)\cos\left(\varphi_x(s) + \varphi_0\right) + \sin\left(\varphi_x(s) + \varphi_0\right)\right] + D'(s)\frac{\Delta p}{p_0} \tag{1.38}$$

Chapter 2
PHYSICS OF CRYSTAL CHANNELING

Crystal channeling is the crystal property which occurs due to the extreme order of arranged atoms: the crystalline lattice. In crystals, coherent interactions are a wide field that have many applications; here just an introduction is discussed for the purpose of providing the basic concepts underlying the bent crystals which used in Accelerators, i.e. planar channeling. Planar channeling is the process which plays the main role in the coherent channeling (section 2.1); the opposite phenomena to planar channeling is dechanneling (section 2.2). More information about channeling physics can be found in [4, 5] .

2.1. Planar Channeling

The observations got by the physicists at the beginning of 20th century about the charged particles beam indicate that this latter emerges from crystal rather than to be completely absorbed by the crystal itself, like occurs in other material of amorphous structure with enough thickness. Stark[1] made the hypothesis from these observations that the crystal has as internal ordered structure. Therefore, following coherent interactions with the crystal lattice particles are allowed to come out from the crystals. Usually, in non-crystalline materials, the energy loss by ionization as a result of the huge number of arbitrary scatters causes the absorption of particles. Pattern of crystalline lattice structure is shown in Figure: 2.1, which is face-centered cubic (FCC) lattice feature of silicon crystals. Since silicon crystals are the most appropriate applicant to be employed in particle detectors, known for their fine developed manufacturing procedures which allow to provide crystalline structures roughly with no imperfections [6, 7], therefore, only Si crystals are explained here. If this crystalline structure of Si is properly positioned to the coming incident particles, the particles will perceive it either as atoms rows or ordered planes. Consequently, particles can experience coherent scattering and trapped among planes (known as planar-channeling) or on following the axis instead of planes (called axial channeling). High efficiency of the planar-channeling as compared to the axial one makes it more appropriate for many applications. This channeling is applicable for positive charged particles, which are our major focus point. The theoretical loom reported here next is based on a classical dealing of interactions among particles and crystals, instead of using quantum mechanics. It is justified by two major reasons:

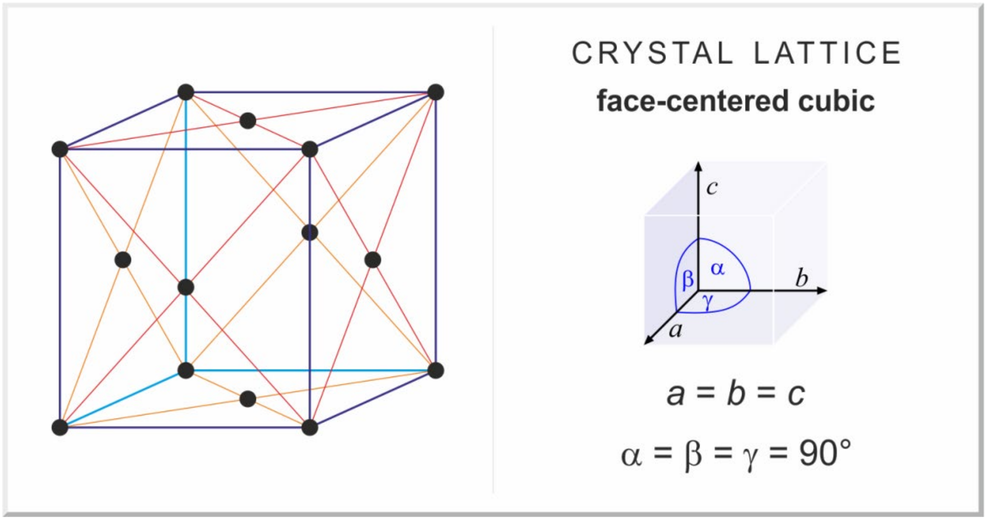

Figure: 2. 1 crystalline lattice of FCC (Face-centered cubic).

1. As given in section 2.1.1, trapped particles in crystalline plane vibrate in a harmonic potential. For that reason, their transverse-energy remains quantized and the energy levels are given by the formula [4]:

$$n = \frac{d_p}{h\sqrt{8}}\sqrt{U_{max} m\gamma} \tag{2.1}$$

In 2.1eq, d_p is the distance between two crystalline planes, U_{max} represents maximum potential well value and "m" denotes the particle's relativistic mass. For n >>1 here as continuous spectrum it can be estimated

2. Tunneling effect can be abandoned if the transverse de Broglie wavelength ($\lambda = h/p$, p is momentum of the particle) is much lower than width of the channel.

2.1.1. Straight Crystals

The main physical quantity to be considered in order to theoretically study the channeling phenomenon is the potential between an atom and particle. According to the "Thomas-Fermi model", this potential can be described as:

$$V(r) = \frac{Z_i Z e^2}{r} \Phi\left(\frac{r}{a_{TF}}\right) \tag{2.2}$$

where Z_{ie} is the impinging particle's charge, Z denotes the atomic number of targeted atom, r represents relative distance and $\Phi\left(\frac{r}{a_{TF}}\right)$ is a "Moliere-screening function" which considers the electronic cloud in the region of the nucleus [8] .

Lindhard states that "under the hypothesis of very small impact angle of the incident particles with respect to the crystalline planes, we can suppose the average potential produced by the total crystalline plane as a continuous potential" [9] described as:

$$U_p(x) = Nd \iint_{-\infty}^{+\infty} V(x, y, z) dy dz \, , \tag{2.3}$$

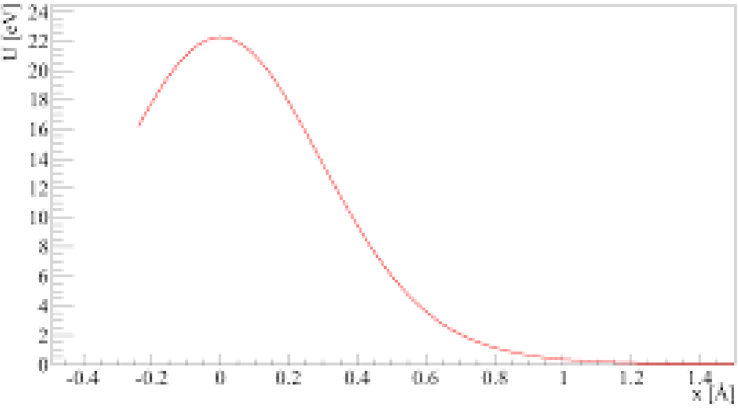

Figure: 2. 2 Potential specified by a single (110) silicon plane in the Moliere approximation (at room temperature).[10]

In equation (2.3) x is the perpendicular coordinate to crystal planes, N is atomic density, d is the distance between two planes and V (x, y, z) is the potential .

Taking into consideration this motion as independent of the position in the crystal and applying a Gaussian spatial distribution for the plane atoms, the potential is specified by the average above this distribution. Then the potential faced by positive charged particle from the whole crystalline plane is shown in Figure: 2.2.

Superimposing two planes it is easy to verify that the total potential near to the minimum experienced by a particle between them will be a harmonic potential. This follows from the assumption that particles are influenced only by the potential of the nearest planes; therefore the total potential well affecting the particle motion among crystalline planes can be estimated as following:

$$U(x) \approx U_p\left(\frac{d_p}{2} - x\right) + U_p\left(\frac{d_p}{2} + x\right) \approx U_{max}\left(\frac{2x}{d_p}\right)^2 \tag{2.4}$$

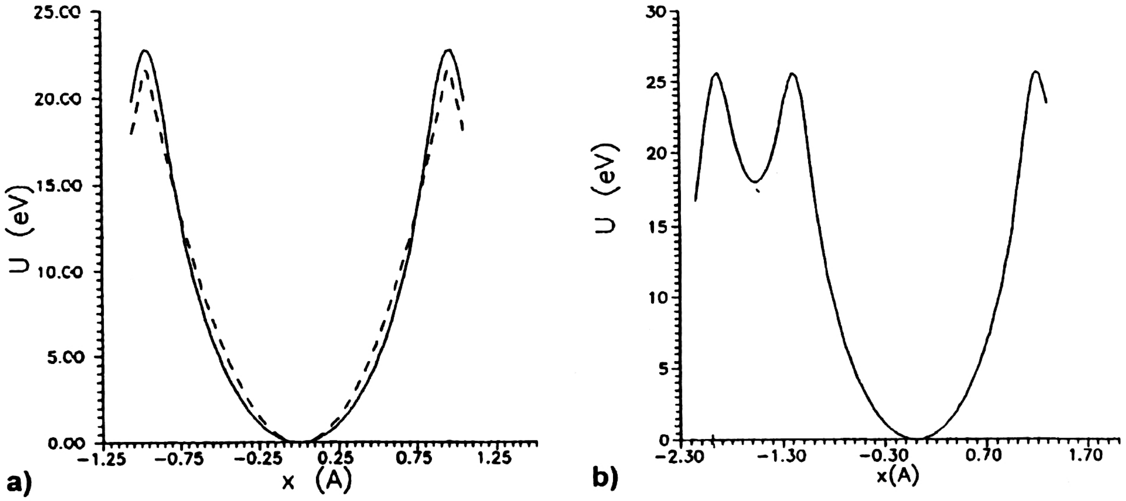

Figure: 2. 3 Potential experienced by a proton ingoing between crystalline planes at a little angle. (A) in silicon strip crystals where (110) planes are used, and with dashed line its harmonic approximation. (B) in silicon quasi-mosaic crystals where (111) planes are used, with their characteristic ratio 1:3 of subsequent planes [11].

The result of accurate calculations and the harmonic estimation of the potential above are shown in Figure: 2.3. It is important to introduce here the two major families of bent crystals: Strip (ST) and Quasi Mosaic (QM) crystals. Both crystals use anticlastic forces to persuade a secondary curve on the planes chosen to steer the particles [6]. The secondary bending is specified to the (110) planes in ST crystals, while in QM crystals the (111) planes are used. The major difference is that the (110) planes are equidistant, while a ratio 1:3 is present in subsequent (111) planes, resulting to the potential in Figure: 2.3 a) and b), respectively. This dissimilarity can be neglected in terms of channeling efficiency if protons are channeled, while it becomes important in case of channeling of heavy ions. The difference can be explained by the high probability to experience nuclear interactions when heavy ions are trapped in the smaller channel of QM crystals.

Defining a reference system as shown in Figure: 2.4 to be trapped, the particle needs a transverse momentum lower than the maximum value to overcome the potential well. Therefore, under the assumption of small impact angle $\theta \ll 1$, it can be written:

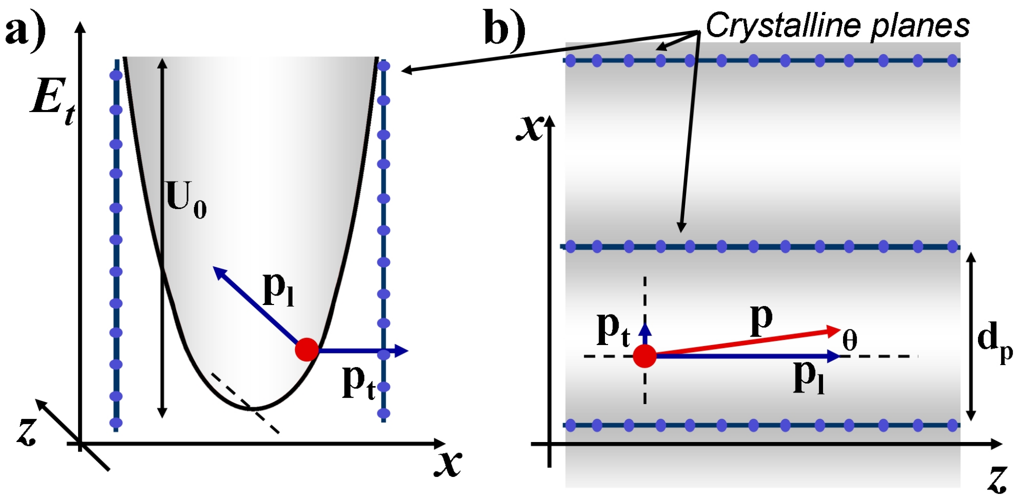

Figure: 2. 4 a) Particle contained in the interplanar crystalline potential. b) Top view of the channels with the same particle, its transversal (*pt*) and longitudinal (*pl*) (with respect to the planes direction) momentum components are shown. The angle q = *pt*/*pl* represents the small misalignment between the particle and the plane.[11]

$$\theta = \tan\frac{p_t}{p_l} \approx \frac{p_t}{p_l} \Rightarrow p_t \ll p_l \tag{2.5}$$

Here p_t is transverse and p_l longitudinal component of particle momentum. Total energy of the particle is conserved and given:

$$E = \sqrt{p_t^2 + p_l^2 + m^2c^4} + U(x) \cong \frac{p_t^2c^2}{2E_l} + E_l + U(x) \tag{2.6}$$

$E_l = \sqrt{p_l^2c^2 + m^2c^4}$ is the longitudinal energy which is conserved as well, since forces are acting in only transverse plane. Thus, to describe a conserved transverse energy as:

$$E_t = \frac{p_t^2c^2}{2E_l} + U(x) \approx \frac{p_l^2c^2}{2E_l}\theta^2 + U(x) \approx \frac{p^2c^2}{2E}\theta^2 + U(x) = constant \tag{2.7}$$

In Eq. 2.7, the θ ≈ $\frac{p_t}{p_l}$, $p_l \approx p$ and E_l =E, are used. Therefore, a particle should have to fulfill the following condition to undergo planar channeling:

$$\frac{p^2c^2}{2E}\theta^2 + U(x) \le U_{max} \tag{2.8}$$

Assume that a particle is entering in mid of the channel, using the relation $pc^2 = vE$ (v is velocity of particle), then the above equation can be simplified as follow:

$$\frac{pv}{2}\theta^2 \leq U_{max} \tag{2.9}$$

Here we can define the critical channeling angle (θ_c), the angle that after which particles will not be able to achieve stable planar channeling, even ingoing in same conditions. This angle depends on the particle momentum by the equation:

$$\theta_c = \sqrt{\frac{2U_{max}}{pv}} \tag{2.10}$$

Several critical angle values of Si crystals for proton beams are mentioned at some energies of interest in Table: 2.1: energies of SPS beam tests with coasting beams, H8 extraction energy, LHC injection and top energy.

Case	**Energy [GeV]**	$\boldsymbol{\theta_c[\mu rad]}$	**λ *[μm]***	**R_c [m]**
SPS coast	120	18.3	33.0	0.3
SPS coast	270	12.2	49.6	0.6
H8	400	10.0	60.3	1.0
LHC inj	450	9.4	64.0	1.1
LHC top	6500	2.5	243.2	15.6
LHC top	7000	2.4	252.3	16.8

Table: 2. 1 Critical channeling angle ($\boldsymbol{\theta_c}$), oscillation period (λ) and critical bending radius (Rc) for Si crystals at classic energies of interest.[10]

The equation of motion of a particle experiencing planar channeling can be obtained from the second derivative of the equation (2.7), which leads to:

$$pv\frac{d^2x}{dz^2} + \frac{8U_{max}}{d_p^2}x = 0 \tag{2.11}$$

In Eq.2.11, the harmonic estimate of the potential specified in Eq.2.4 has been used, with the equation $\theta = dx/dz$,(z is the longitudinal coordinate). In this approximation, the particle will go on sinusoidal path which is given in the following eq (2.12):

$$x(z) = \frac{d_p}{2}\sqrt{\frac{E_t}{U_{max}}}\sin\left(\frac{2\pi z}{\lambda} + \varphi\right) \tag{2.12}$$

Oscillation phase ϕ is find out by the conditions at the entrance of the crystal, and $\lambda = \pi d_p \sqrt{\frac{pv}{2U_{max}}}$ is the oscillation period in the channel. Some Useful values of λ are mentioned in Table: 2.1

Conclusively, particle following planar channeling will oscillate among crystalline planes, in comparatively empty space compared to what is inside an amorphous material. Channeling is one of the significant features of crystals, used in particle accelerators which coherently steer unwanted particles (known as halo particles) into a massive absorber.

2.1.2. Bent Crystals

Once a crystal gets bent, the performances of channeled particles do not vary significantly as compared to what happen in straight crystals. One can show that bent crystals can be replicated by adding a centrifugal force involvement to the potential described in the section [4]. Consequently, the motion equation (2.11) can be modified as:

$$pv\frac{d^2x}{dz^2} + U'(x) + \frac{pv}{R} = 0 \tag{2.13}$$

Where $\frac{pv}{R}$ is a term that represents the centrifugal force in the crystal with bending radius R. The route performed between crystal planes is sinusoidal but ranges about a new equilibrium summit because of the centrifugal force acting on these particles. Here, it is possible to write an effectual potential as:

$$U_{eff}(x) = U(x) + \frac{pv}{R}x \tag{2.14}$$

It is important to note here the reliance of this potential on the energy of particle and the bending radius of crystal. Such upshot is given in Figure: 2.5, whereas the equation 2.14 is given for straight crystals and two different values of the *pv/R*. As a result of this hence it is simple to deduce the occurrence of a critical bending radius depending on the particle's energy, after this the planar channeling is no longer possible to exist, for the reason of the inadequate depth of the potential well. The critical radius (R_c) is the radius for which the value of centrifugal force becomes equal to the maximum interplanar field:

$$\frac{pv}{R_c} = U'(x_{max}) \tag{2.15}$$

Therefore, it can be shown that the critical radius (R$_c$) for known particle energy can be estimated as:

$$R_c = \frac{pv}{U'(x_{max})} \approx \frac{pvx_{max}}{2U_{max}} \qquad (2.16)$$

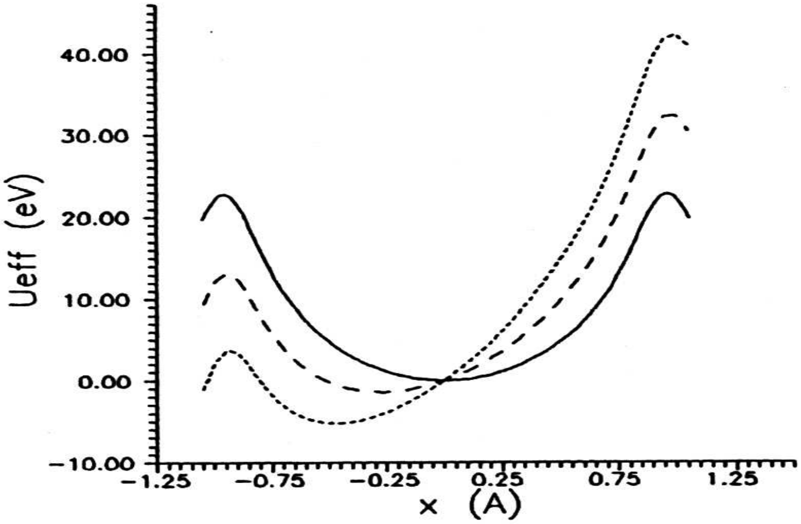

Figure: 2. 5 The interplanar silicon ((110) planes potential computed in the Moleıer approximation for: the straight crystal (solid line), a pv/R of 1 GeV/cm (dashed line) and 2 GeV/cm (dotted line).

In Eq. 2.16 , $U'(x_{max}) \approx 5GeV/m$ in Si crystals [12], and calculated in $x_{max} = \frac{d_p}{2} - a_{TF}$ and not in $x_{max} = \frac{d_p}{2}$ because of finite atomic charge allocation. Some helpful values for R$_c$ are specified in Table: 2.1.

Using the assumptions of Eq. 2.4 (put) in eq 2.14 replacing $\frac{d_p}{2}$ by x_{max}, we obtained:

$$U_{eff}(x) = U_{max}\left(\frac{x}{x_{max}}\right)^2 + \frac{pv}{R}x \qquad (2.17)$$

Furthermore, the location of the minimum potential of the above expression will be:

$$x_{min} = -\frac{pvx_{max}^2}{2RU_{max}} = -x_{max}\frac{R_c}{R} \qquad (2.18)$$

In this situation the reduced depth of potential well[1] can be considered as:

$$U_{max}^b = U_{eff}(x_{max}) - U_{eff}(x_{min}) = U_{max}\left(1 - \frac{R_c}{R}\right)^2 \qquad (2.19)$$

---

[1] The maximum transverse energy for which channeling is still possible

Also the bent crystal's critical angle is customized as:

$$\theta_c^b = \theta_c\left(1 - \frac{R_c}{R}\right) \tag{2.20}$$

Conclusively, the equation of motion for channeled particles among crystalline (bent) planes can be given as:

$$x = -x_{min} + x_{max}\sqrt{\frac{E_t}{U_{max}^b}}\,\sin\left(\frac{2\pi}{\lambda} + \varphi\right). \tag{2.21}$$

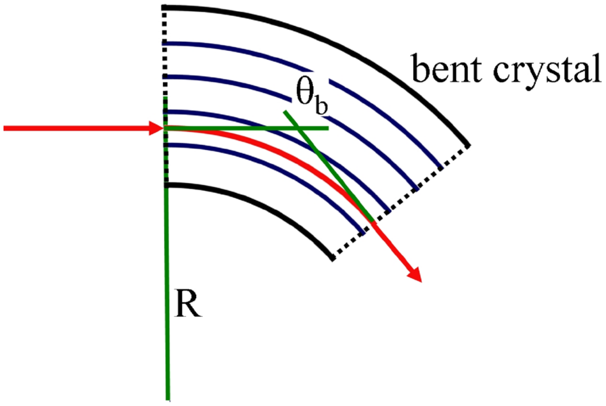

Figure: 2. 6 Bent crystal working principle

Eq. 2.21, explains a sinusoidal path as given in straight crystal, but oscillating about a new minimum x_{min} with different amplitude of ($x_{max}\sqrt{\frac{E_t}{U_{max}^b}}$), and similar oscillation periodλ. If the channeling regime is sustained for the entire length of the crystal, then the channeled particles are deflected by an angle that same to the crystal bending (geometrical).

$$\theta_b = \frac{l}{R} \tag{2.22}$$

where l is crystal length, given in Figure: 2. 6. Noticeably, this can just be got with the crystalline planes that maintain a consistent bending along the total crystal length, which is these days guaranteed by new bending methods and techniques [6, 13]. Example of crystal bending in ST (left) and QM (right) crystals is given in Figure: 2.7.

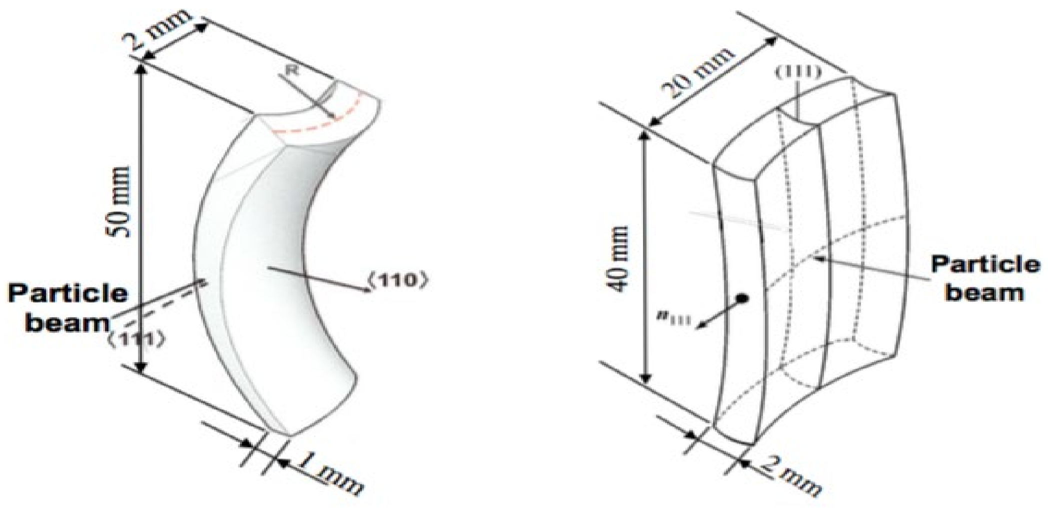

Figure: 2. 7 Geometrical bending of a strip [6] (right) and quasi-mosaic [13] (left) crystal, together with typical dimensions of crystals used for tests in the SPS.

2.2. Dechanneling and Volume Capture

Due to electrons and nuclei scattering, transverse energy of the channeled particles does not remain conserved between crystalline planes. Channeled particles may therefore change their transverse energy on each interaction and might be losing the channeling if the interaction outcomes in a total transverse energy over the maximum potential well. This state is dechanneling (DC) and decreases the initial number of channeled particles, as given in Figure: 2.8. It is more probable to occur for particles having large transverse oscillations (energy already near to the maximum value). In contrast, a particle can go into the crystal structure with energy a little more than the potential barrier. If the interaction gives in a whole transverse energy less than maximum value of the potential well, a fresh energy state similar with a bounded motion among crystalline planes can be attained. This procedure is known as volume capture (VC) (shown in Figure: 2.9). Hence, the dechanneling and volume capture processes can be deemed as mutual to one another.

As mentioned above, channeled particles can boost its transverse momentum because of dispersion from electrons (inside the channel), nuclei (in lattice) or probable imperfections. Assuming the well recognized manufacturing procedure, the existence of imperfections can be abandoned [7]. As mentioned in [4, 5], the dechanneling (DC) process can be explained as an exponential decay of the initial number of channeled particles, which can be therefore given as:

$$N(x) = N_0 exp\left(-\frac{x}{L_D}\right) \tag{2.23}$$

N_0 is the initial number of channeled particles and N(x) describes the number of particles that are still in the channeling regime after a path x, for a known typical dechanneling length. By means of diffusion theory it is doable to obtain the contribution of electron interactions in the crystalline channel [5], leading to the "*characteristic electronic dechanneling length*", this is given as:

$$L_D^e = \frac{256}{9\pi^2} \frac{pv}{\ln(2m_e c^2 \gamma / I)} \frac{a_{TF} d_p}{Z_i r_e m_e c^2} \tag{2.24}$$

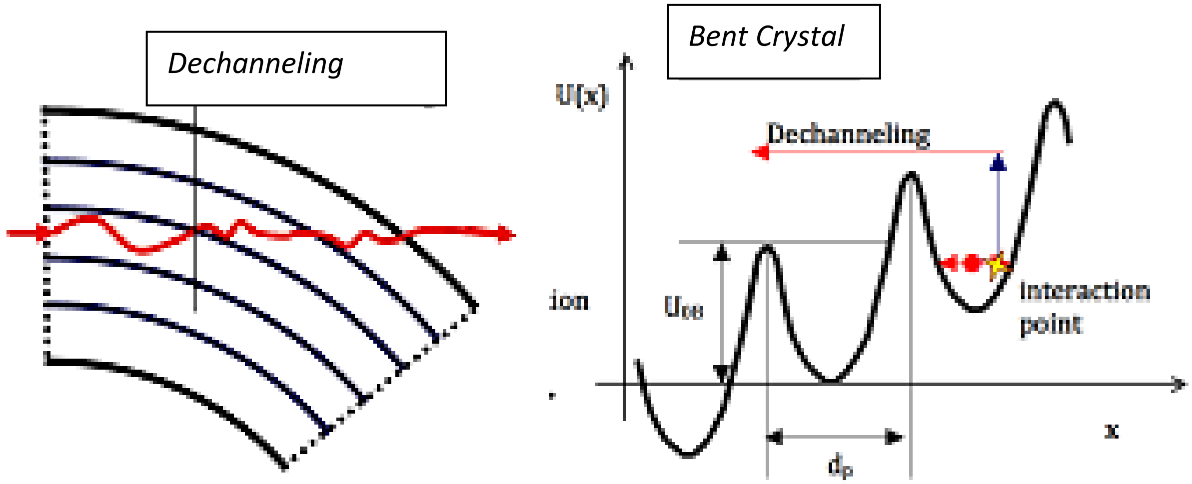

Figure: 2. 8 Design of the dechanneling procedure**.**

In Eq 2.24 ***I*** denotes the ionization potential (e.g ***I*** ≈ 172 eV in Silicon), Z_i the electric charge of the channeled particle, r_e and m_e are classical radius and rest mass of the electron, respectively. Electronic dechanneling just tells about a "slow" dechanneling regime, due to the very little deviation in momentum from scattering with electrons in the channel, leading to partial treatment of the entire process. Because hard scattering on nuclei can results to "fast" dechanneling even for single interaction. Thus, a typical nuclear dechanneling length should also be considered for a trustworthy parameterization of the complete dechanneling way. This typical length for nuclear dechanneling can be obtained by suitable scaling of the electronic value, based on very well tuning by experimental data.

Similarly, proper theoretical analysis is required to describe the possibility that incident particles will be captured inside the crystal volume. This detail can be found in [14], where the reliance of this kind of probability is derived as a function of particle energy "E" and crystal bending radius "R" i.e:

$$P_{VC} = k\left(\frac{R}{R_c} - 0.7\right)E^{0.2} \tag{2.25}$$

In equation 2.25, k is a constant tuned by means of comparisons between experimental and simulations data. As the particle get captured, it is dealt as channeled particle and the probability of a following dechanneling interaction should be considered as given in [10].

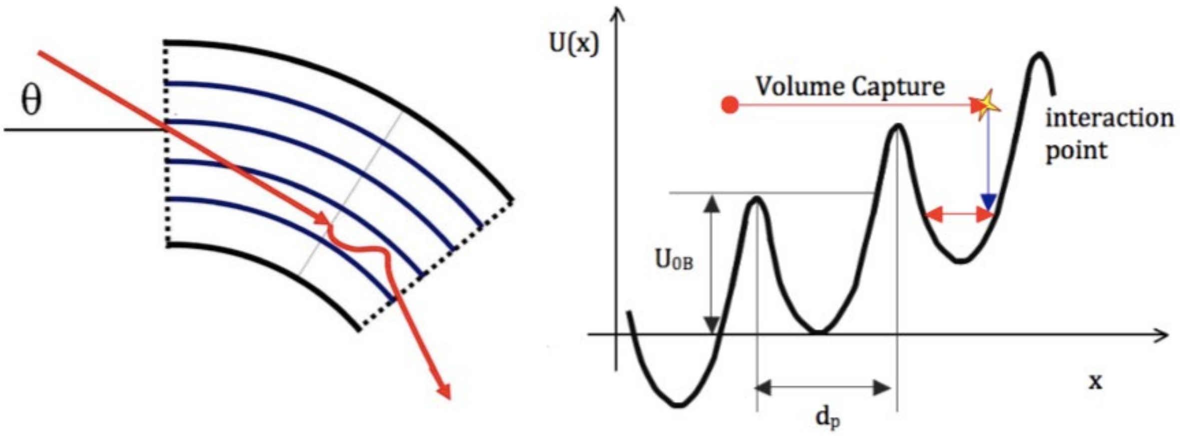

Figure: 2. 9 The volume capture process from a geometrical point of view (left) and using the effective potential in bent crystal (right). The red point represents the initial condition of the particle in the "transverse energy-transverse position space"

2.3. Volume Reflection

Particles that encroach on bent crystal with an incident angle ranges $\theta_c < \theta < \theta_b$, ($\theta_c$ is critical angle and θ_b is bending angle of the crystal), can practice the so called volume refection VR. Protons that experience this process are factually reflected by the contact with the averaged potential of crystalline planes. Actually the reflection occur when particles incidence on a crystalline plane with their momentum tangential to it. The expansion of the angular range on which this tangency circumstance can be achieved is determined by only geometrical considerations. This situation can be attained quite simply by ingoing particles to bent crystals[2] with an angle faintly above the critical angle (where bounded states are no longer possible). It is

---

[2] In direction of the bending

simple to suppose that if particles enter into a bent crystal with angle bigger than crystal bending, it will not possible to achieve a condition where the momentum is parallel to the crystalline planes. Example is given in Figure: 2.10.

For the above described reasons, one can anticipate that the reflection process is basically very efficient, with the probability of reflection > 90% for particles in the angular range [15].

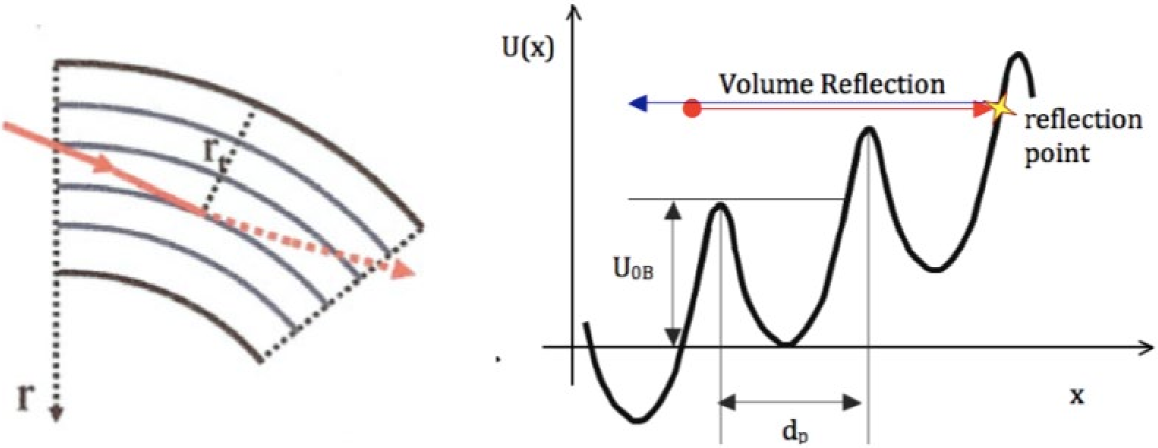

Figure: 2. 10 Reflection of a charged particle in the crystal volume at the turning radial coordinate r_t : a) graphical view of the crystal; b) phase space of the particle transversal energy as a function of the radial coordinate.

This quality can be very helpful if one desires to employ a crystal as particle deflector (average efficiency of channeling ≈ 60%); though the nuclear interaction rate of a reflected particle is five times more than for channeled particles, as calculated in [16]. The channeling efficiency may also be enhanced in storage rings credit to *the multi turn process*, attaining multi turn channeling efficiency analogous to the volume reflection in single pass. Another main feature of the reflection process is how much the incident angle is customized, which is associated to the critical channeling angle in straight crystals. From simulation studies [15] it is possible to obtain that, for crystals with $R \gg R_c$, the average deflection given to reflected protons is $\approx 1.6\ \theta_c$ [17], which make it feasible to derive the reliance of such deflections as a function of the significant crystal parameters. A good explanation [14] that hysterics experimental data for both the average deflection (θ_{VR}) and its spread($\Delta\theta_{VR}$), is:

$$\theta_{VR} = c_1 \theta_c \left(1 - c_2 \frac{R_c}{R}\right) \tag{2.26}$$

$$\Delta\theta_{VR} = c_3\theta_c\frac{R_c}{R} \tag{2.27}$$

c_1, c_2 and c_3 are empirical coefficients tuned to replicate experimental data. From these deliberations it is obvious that the deflection given during volume reflection (≈1.6 θ_c) is smaller than the value that can be achieved through planar channeling when a crystal is bent (θ_b). On the other hand, this can be solved by numerous reflections on several strip crystals, called multi-strip [18], which are not dealt here, and learning are continue to get multiple reflections in single crystals, in that way avoiding troubles of misalignment among strips.

The finest crystal process to fulfill the requirements of definite tasks, requisite from bent crystals in specific accelerator surroundings, must be dealt with balancing the various issues: efficiencies, nuclear interaction rates, and deflections required.

Chapter 3
UA9 EXPERIMENT AT CERN

3.1. Introduction

The UA9 (Underground Area 9) experiment was installed in March 2009 at CERN-SPS with the aim of investigating and verifying the usability of crystal channeling (see chapter 2) to improve the collimation of both proton and heavy ion beams in LHC.

Characterization of crystals for channeling is usually carried out in fixed target experiment setup located in the North Area of CERN at "the external beam line called H8". In the said area different types of crystals made by different groups in the collaboration such as INFN Ferrara, PNPI (Saint Petersburg) and IHEP (Protvino) are installed to test and verify the main fabrication parameters including Deflection angle, Efficiency, and Torsion etc. Few selected crystals are then installed in the Long Straight Section 5 (LSS5) of the SPS for collimation and other crystal-assisted manipulation studies.

3.2. Crystal Collimation

In large particle accelerators the beam collimation system has a progressively important role, which scales in significance with the collider performance. Detail about LHC present collimation (sketch is shown in Figure: 3.1) is given in [19] and its major limitations and the baseline for achievable upgrades in the HL-LHC period can be found in [20] however, here a brief discussion is given here below:

In spite of the brilliant performance of the current collimation system all through LHC run I and II, it may not be enough after the foreseen future machine improvements in particular for heavy ions. A collimation scheme based on bent crystals as a primary phase was considered one of the most capable approaches. The viability of such an inventive concept was established during the years 2009 – 2012 with experimental tests in the SPS carried out in the structure of the UA9 collaboration [21, 22].

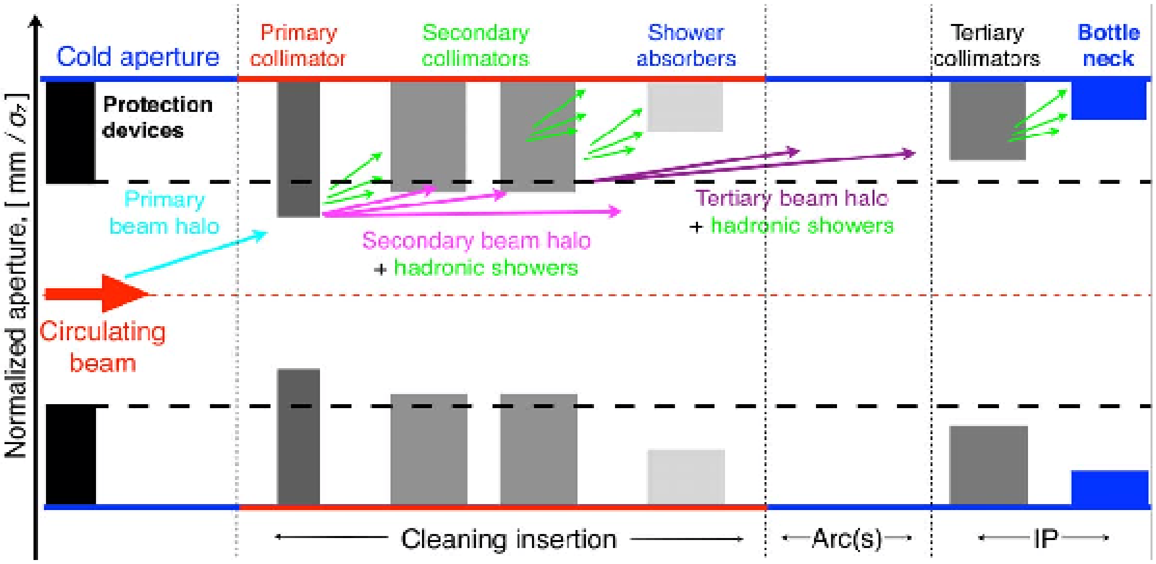

Figure: 3. 1 Working principle of the current collimation system.

The working theory of crystal-assisted collimation is given in Figure: 3.2 its basic concept is coherent steering of halo particles onto a massive and huge absorber using the phenomena of crystal channeling. Ideally, just one crystal per plane is required with a related absorber. They should be positioned at the boundary of the beam envelope, and angularly oriented to position the crystalline planes at the entry point parallel to the beam direction. This would be the best channeling orientation; furthermore, crystals must be positioned at a location of the lattice where the divergence of the intercepted halo particles is lower than the critical channeling angle.

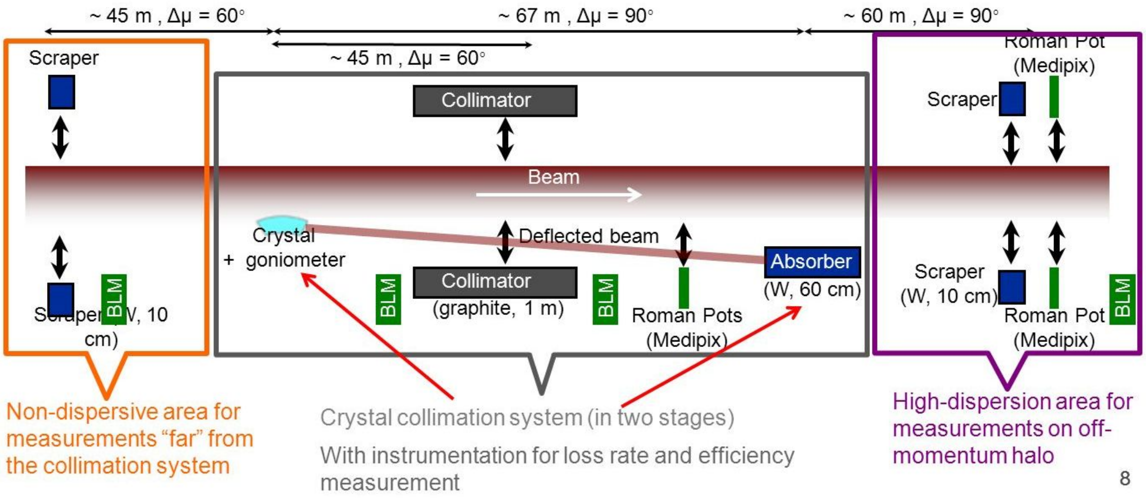

Figure: 3. 2 Crystal collimation scheme.

3.2.1. Main advantages of Crystal collimation

The main achievements of crystal collimation scheme with respect to the other given:

i. More compact system.

ii. Considerable decrease in inelastic interactions at the first collimation stage.

iii. Large deflections given to primary halo particles.

iv. Important reduction of the machine impedance due to contributions from the collimation system.

All the items above should allow a safe increase in the circulating beam intensity as planned in the future years in the LHC, to increase the luminosity distributed at the experimental points.

Indeed:

i. More compact system would be easier to grip and help in concentrating losses in a controlled and lesser area, starting from a small number of hundred meters to less than one hundred.

ii. The abridged probability at the primary point of single diffractive events in the case of protons, and fragmentation or dissociation in the case of ions, can mitigate considerably the main restriction of the present collimation process.

iii. A big deflection from a particular passage through a bent crystal would entail faster cleaning, allowing also a better transverse aperture of the subsequent collimation stage. Generally, only one massive absorber per crystal would be required. This will result in a reduction of the contribution to the impedance budget of the machine, as only a few mm of silicon crystal and few absorbers will surround the beam. Although the presence of more secondary collimators is required for reasons of phase space coverage for machine protection purposes, the bigger gaps that can be used should also lead to a considerable reduction of impedance.

3.2.2. Main challenges to Crystal collimation

The most important questions to be dealt with before committing to this innovative concept of beam collimation as a baseline for the HL-LHC upgrade are:

i. Can crystal collimation truly improve the current already better cleaning system?

ii. Can crystal collimation guarantee steady performance in any machine pattern (i.e. injection, ramp, squeeze, collision)?

iii. Is it compatible with protected operation in all beam conditions?

iv. Do crystal properties, experienced so far at lower beam energies, scale to the LHC energy as anticipated?

A test crystal-assisted collimation layout was developed for the LHC. Two goniometers with crystals were installed in the Interaction Region 7 (IR7) of the LHC Beam1, and first collimation tests were carried out in 2015. Later the system was replicated in Beam 2. Over the years, until the start of Long Shutdown 2 at the end of 2018, in a number of machine development runs, crystal collimation successfully proved to give better cleaning than the standard collimation scheme and to be stable in all machine configurations (i.e. injection at 450 GeV, ramp to 6.6 TeV, squeeze and collision) with both protons and heavy ions [23] [20] [24] [25].

For what concerns safety of operation, an operational crystal-based collimation system would include appropriate absorbers to cope with the highly concentrated high intensity proton beam halo without damage; such absorbers, sort of internal mini-dump, have not been studied yet and are not available in the LHC. In the case of heavy ions, instead, the beam power is much less; therefore crystal-assisted ion collimation has been included in the base-line for the High Luminosity LHC runs starting in 2027.

3.2.3. Damage to the crystalline structure

Another important point to be addressed is the damage to the crystalline arrangement, this could happen because of an unintentional beam dump on the crystal, or due to accumulate radiation dose through normal operation as a primary collimation phase. The nastiest accident that could occur is an asynchronous beam dump on a few mm lengthy silicon crystals.

Worsening of crystalline properties because of operating in primary collimation can only be put up with if reliable performance is achieved every year. An insignificant change in recital has been experienced for crystals that are installed in the SPS. Although these crystals are extensively stressed during tests, they are used for a few days per year. Though, other approximation can be made by seeing to NA48 experiment observations, where crystals were put to the radiation level corresponding to approximately five years of operation in LHC as a primary collimator. The deposited energy during the NA48 experimental run resulted to a decline of channeling efficiency by about 30 % [26]. Therefore crystals could endure operational doses but should be substitute at every long shutdown. These experimental results can be elucidated by the truth that what is actually hazardous for our intention is the energy provided to the crystalline structure. This is mostly because of loss in ionization energy, since the rest of the energy lost in the crystals moves into production of hadronic showers. In LHC case, energy loss by ionization from 7 TeV protons in miss-oriented silicon crystals is in a few MeV, whereas that deposited by lead ions is in the order of a few GeV. Hence, flawed orientation with respect to the beam envelope must be shunned any time, principally when ions get injected inside the machine. Several irradiation experiments have been carried out on the SPS crystals to simulate the effect of an accidental beam dump in LHC.

A number of tests were carried out at the HiRadMat facility at CERN where a high intensity pulsed beam of 440GeV is available. The main outcome was that in case of accidental beam dump, such crystals would survive exclusive of breaking down, so without causing contamination that could seriously degrade the main vacuum of the LHC [27] [28]. Nevertheless, additional tests are foreseen to study the exact damage in crystalline structure.

Some other crystals were also exposed to neutrons from the SCK-CEN BR2 reactor in Belgium, and the experiment outcome will be discussed in Chapter 4.

3.3. UA9 experimental areas

The CERN North Area consists of three experimental halls and provides 8 beam extraction lines for scientific purpose [29] (Figure: 3.3). H8 beam line is located in EHN1 Hall of North Area. Few times per year the UA9 collaboration conducts tests of the silicon crystals using the beam of this line. The experimental setup is situated upstream the test beam line which means that UA9 is the main user of the beam during their tests. Beam parameters can vary due to the type of particles and their energy. Typical intensity is 2 x 10^8 particles per spill and its length is 4.8-9.6 s [30]. The setup used to characterize the crystals in H8 is shown in Figure: 3.3.

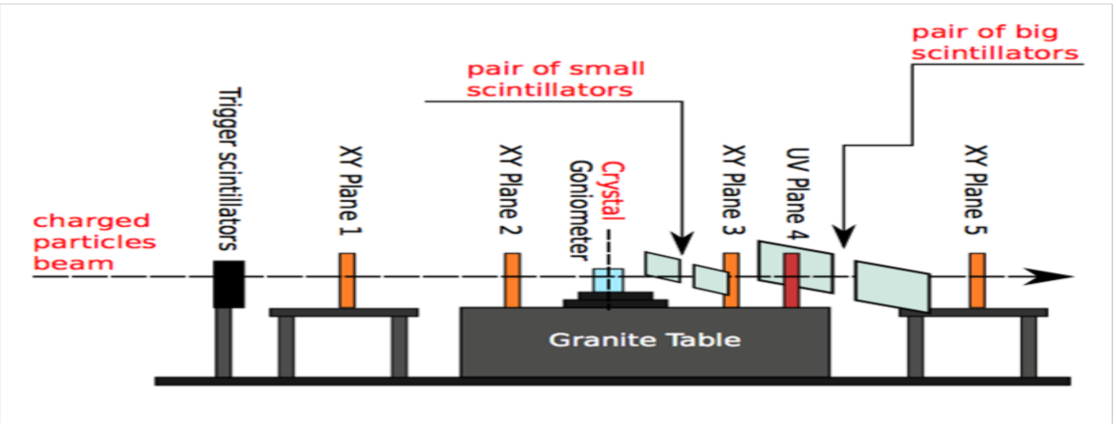

Figure: 3. 3 The scheme of the UA9 Experimental layout at the H8 beamline in EHN1.

The complete layout of the CERN accelerator complex is given in Figure: 3.4 top a & b; while Figure: 3.4 bottom shows the position of H8 line in schematic layout of EHN1.

3.4. UA9 Layout

Since 2009 the UA9 experiment installed in the SPS Long Straight Section 5 (LSS5) (Figure: 3.4) of the CERN SPS accelerator to investigate the use the bent crystal channeling for the development of the crystal-based collimation performance for LHC. The characterization of the crystals including channeling efficiency investigations takes place at H8 extraction beam line of the SPS North Area (NA) (Figure: 3.4).

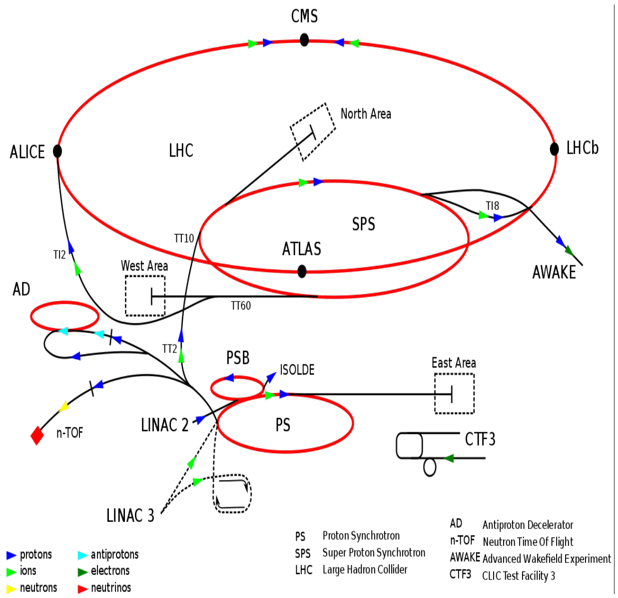

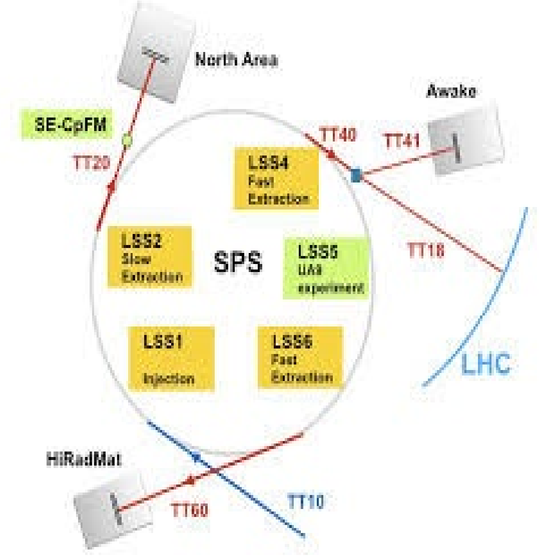

(a) CERN accelerator facilities.

(b) CERN SPS with marked NA and LSS5 zones

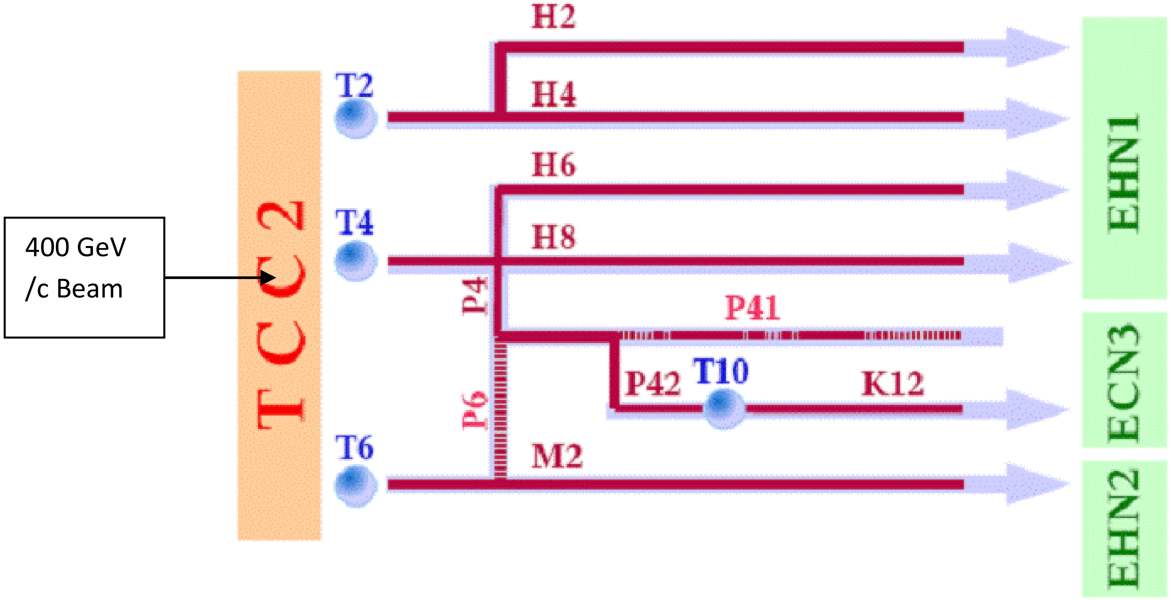

I North Area Beam Lines
Figure: 3. 4 Experimental locations of UA9 at CERN SPS.

Detail about H8 Beam lines experimental setup can be found in [31].

3.4.1. UA9 instrumentation in SPS

The layout of the experiment in SPS has been upgraded year by year; the latest layout is shown in Figure: 3.5. Detailed information of the SPS UA9 components alignment process is well explained in [32]. The design of the UA9 experiment (Figure: 3.4) comprises two IHEP goniometers (with a pair of bent silicon crystals for each goniometer). Goniometer gives crystals horizontal linear and rotational movements with a designed angular resolution of 1 *µrad* and accurateness (repeatability) near to10 *µrad.*

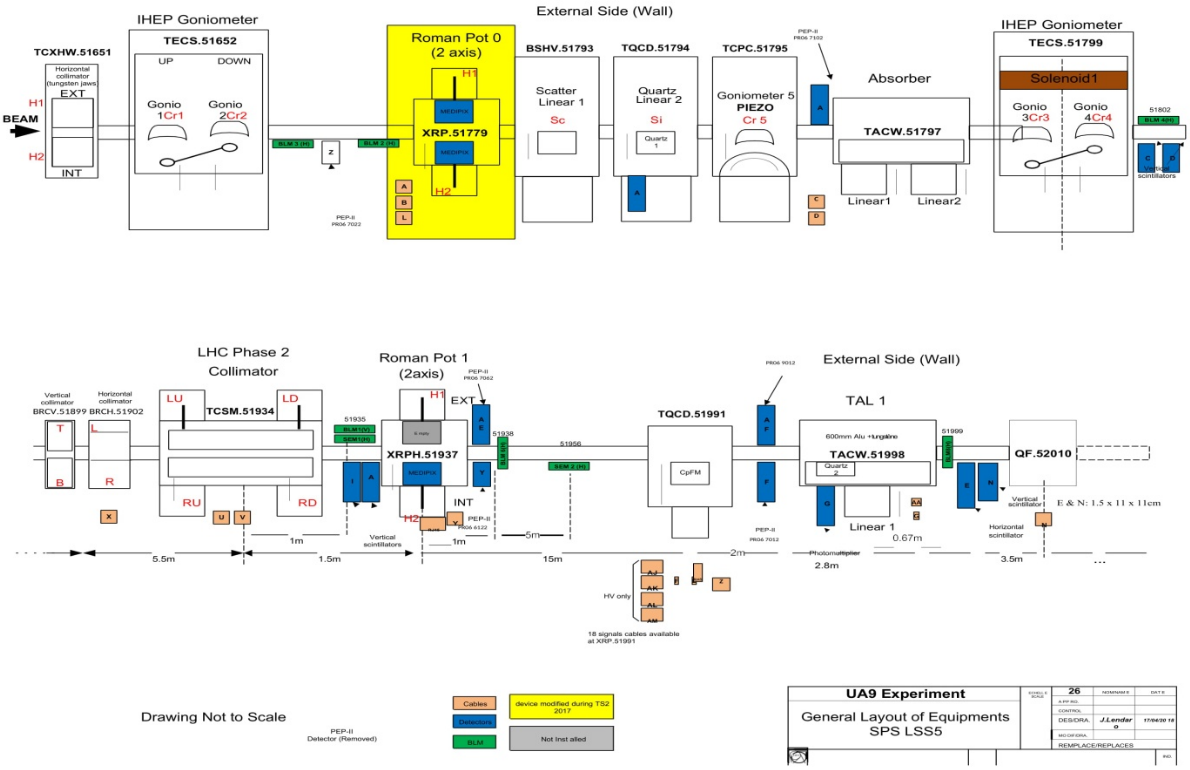

(a) UA9 collimation schematic of general layout 2018 data taking

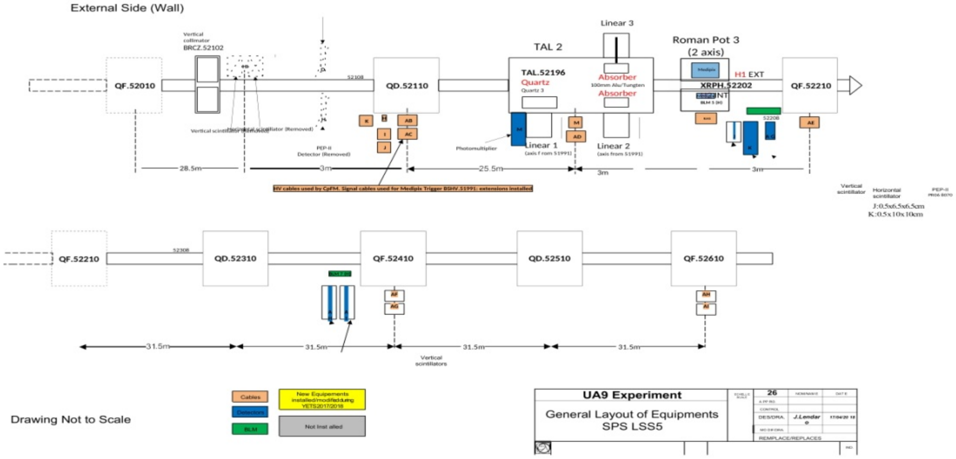

(b)

Figure: 3. 5 UA9 collimation schematic of general layout 2018 data taking

Tungsten absorber (TACW) is used to intersect the deflected beam; it is a 60 cm long moveable absorber which has *70 x 60* mm^2 cross-section. It is located around 60 m downstream the crystals with a 60^0 phase advance approximately for the purpose to maximize the parting between channeled and primary beams (Eq. 1.25). Between crystals and TACW there is LHC-type collimator (TCSM) along with two horizontal graphite (1 m long) jaws is placed. At the distance of 1.5 m downstream the collimator there is a Roman Pot 1 (RP1) tank with a Timepix detector fixed in secondary vacuum. A horizontal mechanical linear axis is used for the detector alignment. The Roman pot has 0.2 mm thin aluminum walls and is 3.4 cm wide alongside the beam direction. There are various types of detectors fixed close to each device, exterior the beam pipe, such as polystyrene scintillators and LHC-type BLMs[32, 33], which are composed of a 50 cm long cylinder having 9 cm diameter, filled with N_2 at 100 mbar overpressure and using an integration time of 1.2 s. A Beam Wire Scanners (BWS) [34] is a device used for the main beam profile measurements. Throughout the experiment the results of BWS measurements are taken for the beam emittance estimation, while the intensity of the beam in the machine is measured by means of a Beam Current Transformer (BCT).

3.4.2. UA9 Instrumentation at H8

Coordinate System

In the explanation which follows left-handed coordinate scheme is used with the z-axis in the direction of the incident beam and x- and y- directions referring to the horizontal and vertical displacements. Therefore the measurement locations are referred to as XY planes. The crystals adopted for channeling studies are generally positioned so that the expected displacement is in the horizontal plane and so the angular scan is about a vertical axis.

3.4.2.1. Telescope

Charged particle telescope is constructed for data taking in CERN 400 GeV/c proton beam line. It employs ten planes of silicon micro strip sensors, set as five pairs each measuring two orthogonal coordinates, with an active area of 3.8×3.8 cm^2. The purpose is to provide outstanding angular and spatial resolution for measuring the routes of particles incoming and then outgoing from a crystal after interaction with it[35]. Telescope Hardware:

i. Sensors
ii. Front end hybrid (detail can be found in [36])
iii. Optical Link
iv. Readout and control system

v. XY Plane construction

3.4.3. Data Acquisition System [35]

For the measurement of crystal channeling, the main aim is to do angular scans of a crystal mounted on the goniometer for the purpose to recognize the right orientation for channeling and to obtain enough data about that position. The Data Acquisition (DAQ) is obligatory to collect data from the telescope front end, design it for storage and supply online monitoring to verify data quality. In order to allow an automatic scan process to find the channeling direction, the DAQ must also interface with the goniometer to control its positioning and record its coordinates in the data stream. The essential factors should be considered when designing such a high rate DAQ system are event size, bandwidth bottlenecks, particle spill structure and period as well as available memory, buffer sizes, computational power and disk write speed.

Figure: 3. 6 XY Planes

3.4.4. Hardware Architecture

The hardware of the structure is developed around the CMS Tracker Front End Driver (FED) [37] which is responsible for the capture, digitization, processing and packaging of the analogue optical signals from the front end APV25 chips. Data is transmitted using the S-Link64 interface which significantly increases the readout rate as compared to VME. A FED Kit PCI card is fixed in a DAQ PC and obtains the S-Link data directly from the FED.

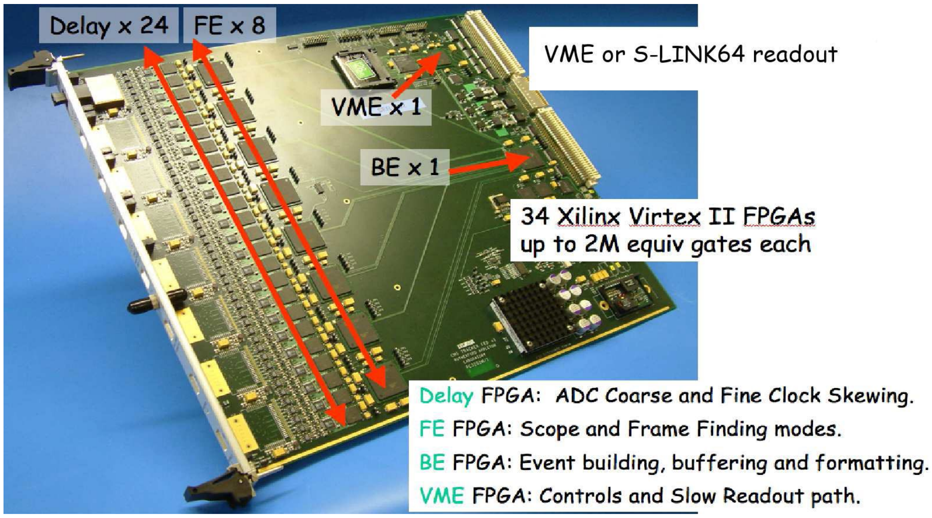

Figure: 3. 7 Photograph of a CMS Tracker FED. It is a 9U format VME board whose principal features are identified on the photograph.

3.4.5. Software and run manage

The software is generally written in C++ Object Oriented modules with some sustaining applications written in Java such as the Run Control Interface. The software can be divided into main three parts: DAQ online, run control user interface and data analysis.

3.5. Data Analysis Procedure

The analysis of the tracker data allows evaluating the bending angle of the crystal under test, the efficiency of the channeling process and the crystal torsion.

Data analysis procedure can be explained in following steps whereas the software / programs used as a tool are “Root” and “C++ Scripts”:

i. Analyze the alignment run of the tracker which gives the reference beam position and divergence for the run under analysis. Data are recorded with full experimental setup but without crystal.

ii. The second step is High statistics run in channeling position. The data collected in this run help to plot the $\Delta\theta_x$ **vs** x position graph which gives the position of the crystal in front of beam.

iii. The data must be cut geometrically in both x and y axis; in strip crystal the geometrical cut in x is the width of crystal which can be clearly seen in plot. The cut in y is usually the beam height which is ±3 mm.

iv. In order to measure the channeling bending angle the next step is to analyze and correct the torsion effect that is inherent in strip crystals. Indeed, the mechanical bender can induce a small undesired rotation of the crystalline planes about the y axis. This means that the deflection angle is different along the y axis. The torsion correction procedure is applied to get rid of this effect. The torsion effect can be estimated observing the relative channeling efficiency depending on the y impact position and deflection angle in x plane (Figure: 3.8). Then we apply linear regression of this plot and obtain the offset of the channeling spot and the torsion measured in $[\mu rad/mm]$. Then the deflection angle is corrected using the parameters obtained from linear fit.

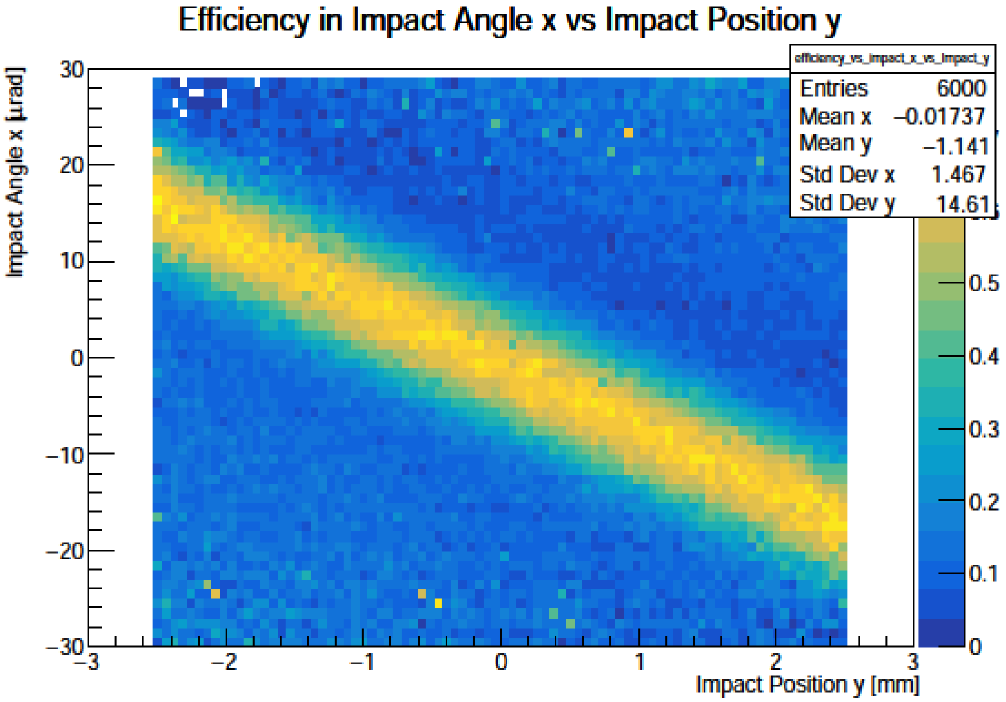

Figure: 3. 8 Efficiency map as a function of y and Δθx for STF 123 crystal tested in September 2018

v. The last point of the analysis procedure is to calculate efficiency and deflection angle of the channeled particles for various incoming angle cuts.

3.6. Other investigations by the UA9 Collaboration

Beyond crystal collimation the steering capability of bent crystals was also exploited in the slow extraction of the beam from SPS. Experimental test runs were made using the channeling effect in a bent crystal to steer the halo of the SPS beam into the electrostatic septum gap at the beginning of the extracted beam line [38].

A crystal in channeling orientation also proved successfully to be able protect the septum wires from impinging particles during resonant slow extraction, thus allowing decreasing the particle losses at the septum by over 40% [39]. This scheme will be made operational in 2021.

A high-energy beam extraction had already been investigated before. The initial successful research in this track were carried out at the SPS CERN accelerator by the RD22 Collaboration [40], at U-70 IHEP-Protvino accelerator [41] and at Fermi lab Tevatron accelerator in the E853 experiment [42]. The key outcome of these experiments is that efficiency (10-85 %) was reached for high-energy proton and ion beams (70-900 GeV).

Chapter 4
Characterization of crystals

Before being used at the SPS or LHC accelerators each crystal has to be tested and checked many times to verify the stability of the deflection angle and other characterizing parameters in time, and after heating (baking). These tests are performed at H8 beam line using proton, pion or ion beams with several energies.

One of the important parts of this PhD work is the characterization of some crystals in UA9 Experiment, which is given in detail as follow:

4.1. Experimental characteristic

4.1.1. Arrangement for experiment

Two main structures of silicon bent crystal have been considered for particle beam collimation: 1. Strip Crystal (ST) 2. Quasi-Mosaic (QM) crystal. In the first one, the crystal is bent throughout the crystalline axis (110) and in the second one through (111) crystalline axis. The main difference between these two crystals is the inter-planar potential. The ST crystals have equidistance crystalline plane so all channels have the equal size while QM have a ratio 1:3 for following planes [43]. Recently, the UA9 collaboration has focused the study on ST crystals, for possible application in both LHC and SPS.

The silicon micro strip telescope is installed upstream and downstream of the crystal to perform high resolution measurements (Figure: 4.2).

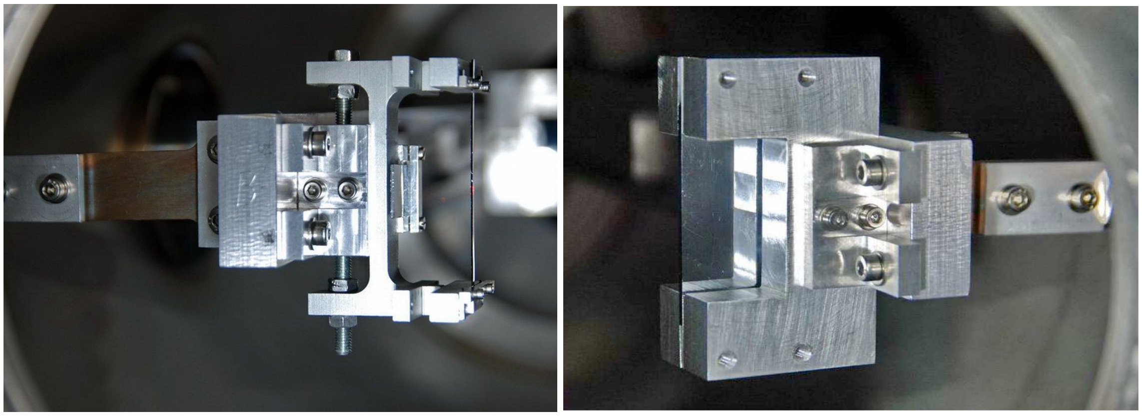

Figure: 4. 1 Cr1 strip crystal in CERN tank (left) and Cr3 quasimosaic crystal (right)

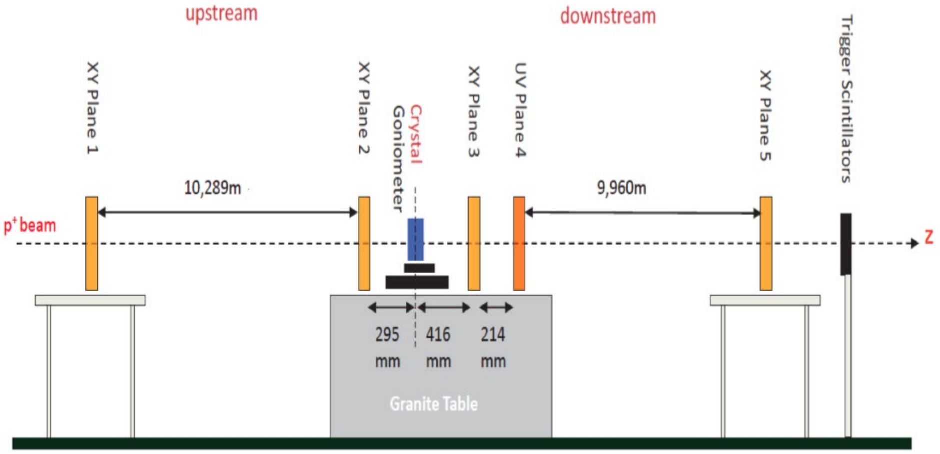

Figure: 4. 2 Side view of the experimental design in the H8 beam line. The UV plane represents the 45^0 rotated XY-planes.

The main input to the position resolution of the impact parameter at the crystal is due to the position resolution of the closest tracker plane to the goniometer position, whereas the angular resolution is mostly affected by the multiple dispersion of the particles with the sensors. The incoming track is rebuilt from an extrapolation of the line reconstructed with the points measured by the first two planes. The exit tracks are reconstructed fitting the points measured with the final three planes. The main condition for a particular trajectory is the same contact/impact point at the crystal position for the two tracks upstream and downstream of the crystal (see Figure: 4.3). Therefore, for each path, three free parameters for each projection on the orthogonal axis are given: the two angles $\boldsymbol{\theta_{in}}$ (incoming angle) and $\boldsymbol{\theta_{out}}$ (outgoing angle) and the impact point at the crystal position $\boldsymbol{d_0}$ (impact parameter at z = 0). The angular resolution of the telescope is measured in a precise alignment run. The resolution is calculated as the angular deflection of the particle $(\Delta\theta = \theta_{in} - \theta_{out}$) when the crystal is not present.

4.1.2. Alignment Run analysis

To estimate beam position and beam divergence before entering the crystal alignment run is performed. As just said, this run also helps to estimate the telescope resolution from angular resolution $(\Delta\theta = \theta_{in} - \theta_{out})$. The measured resolution is 11.4 μrad with protons/pions of 180GeV.

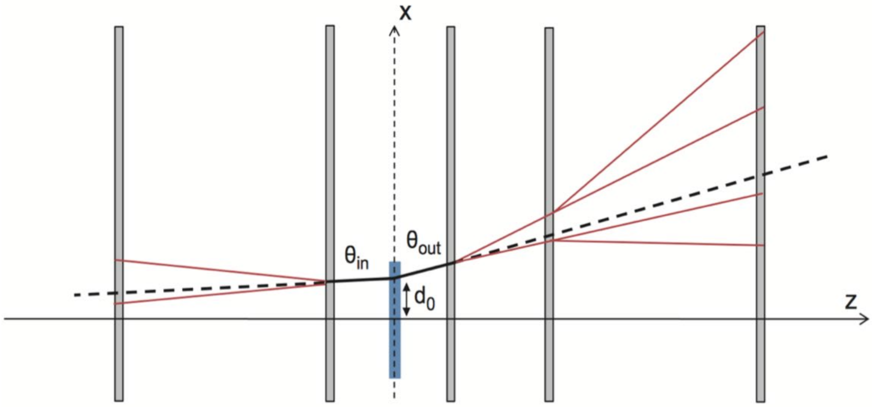

Figure: 4. 3 Top view of the track fitting method

4.1.3. High Static run analysis

After alignment run the next step is high statistics runs in channeling position. $\Delta\boldsymbol{\theta x}$ vs $\boldsymbol{x}$ and $\boldsymbol{y}$ plots help to center the crystal position with respect to the beam and specify geometrical cuts in x and y-axis. As it is mentioned above that for strip crystal the cut in x axis is the width of crystal which can be seen in plot. The cut in y is typically chosen to consider the beam height (from the Alignment run). The crystal is fixed so that the channeled particles are mostly incident in x plane. So the aim of applying cut in y is to select the most intensive part of the beam. In my analysis it was decided to consider the value of y cut equals to ±3 mm.

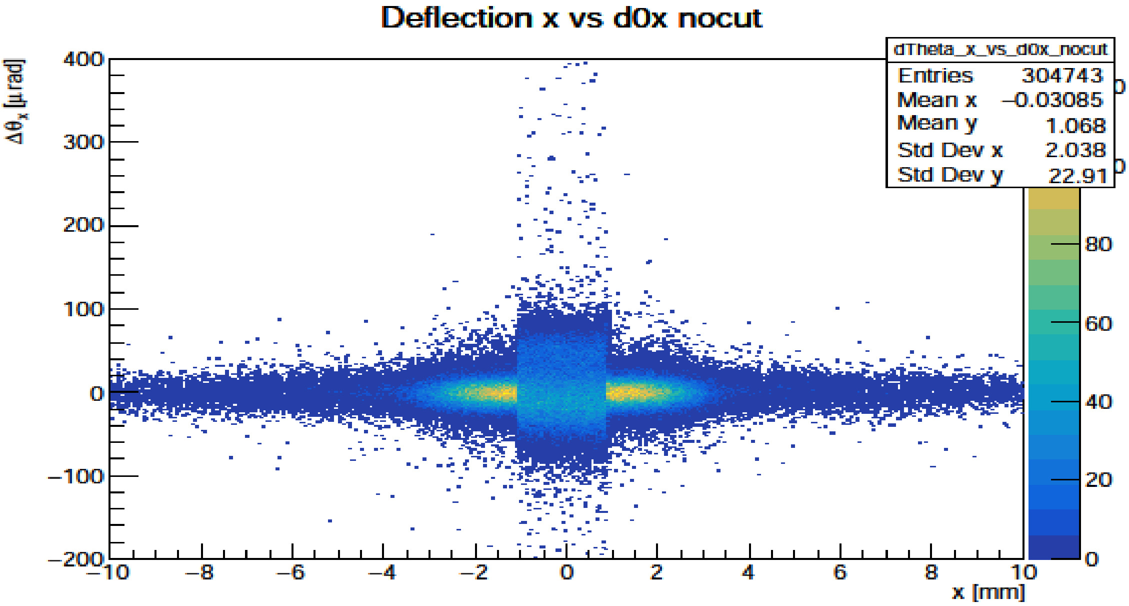

Figure: 4. 4 Geometrical cuts

4.1.4. Torsion Correction

Strip crystal tends to have a residual torsion which results in the rotation of the crystalline planes along the y-axis. It leads to a different relative angle between impinging beam and crystalline planes directions. This effect can be estimated and corrected through a special procedure. To do this from the relative channeling efficiency depending on the y impact position d_0y and deflection angle in x plane $\Delta\boldsymbol{\theta x}$ (see Figure: 4.5) we extort behavior of the mainly efficient $\Delta\boldsymbol{\theta x}$ respect to the d_0y. The slope of the line extracted from linear regression explains the torsion [μrad/mm], while as the abscissa is the offset angle that carries the relative angle in 0^0 (see Figure: 4.3). Then the incoming angle is corrected using the parameters obtained from linear fit.

Figure: 4. 5 Linear regression for STF 123

4.1.5. Channeling Efficiency and Deflection Angle

The ratio between the channeled particles and total incidence particles on the selected area of crystal face within known angular region is called channeling efficiency. For channeling efficiency critical angle θ_c is very important parameter which depend upon the energy of particles beam by equation.

$$\theta_c = \sqrt{\frac{2U_{max}}{pv}} \tag{4.1}$$

U_{max} is the maximum potential well, p is momentum and v is velocity of the particles.

For 180 GeV/c pion the value of critical angle is ***16 µrad*** [44] **.** There are mainly two ways to calculate the efficiency and deflection angle.

(i) When channeling and amorphous peaks are not merged for the largely bent crystals then Gaussian fit on the data in the range of expected channeling is performed. The amount of channeled particles is estimated as a counted sum of events in the range of ±3σ of the fitted function. The ratio between this number and the total number of events in the histogram describes channeling efficiency, when the mean value of the Gaussian peak represents the deflection angle.

(ii) The other way to calculate efficiency is to fit the angular distribution with double Gaussian. This approach permits to exclude contagion of events that come from amorphous peak and gives realistic results. In the cases where both methods can be applied the absolute difference of 1 % in efficiency and the same values of deflection angle within the uncertainty are observed.

4.2. Neutron Irradiation and Channeling Efficiency of Silicon Crystals[3]

The UA9 experiment CERN developed crystal technology for channeling in the last decade, this experiment has successfully obtained very promising results for the LHC collimation [24] and the SPS slow extraction [25, 38], beam splitting and focusing [45]. Monocrystalline silicon is broadly used for these purposes because of the lattice quality reached nowadays at a relatively low cost. In the present and future work such as High Luminosity (HL-LHC) and the Future Circular Collider (FCC), it is mandatory to study the crystal potential especially robustness during accelerator operations. Actually, high energy particles fluxes produce damage in crystal lattice which affects the channeling performance. There are three kinds of lattice defects which affect channeling efficiency mainly: point-like defects (impurities, interstitials and vacancies), linear dislocations and mosaicity. At high energies, a large number of atoms (~10^5) along the channeling planes are involved in one oscillation of the channeled particle, consequently the point-like defects effect is the least important. On the other hand, linear dislocations could decrease the channeling efficiency. Finally, the particle angular

---

[3] The detail work is submitted for publication" Channeling efficiency reduction in high dose neutron irradiated silicon crystals" by Marco Grattini (corresponding author)

dispersion due to mosaicity of monocrystalline and pure silicon crystals is much smaller than the channeling acceptance angle until tens of TeV.

It is therefore, in addition to aforementioned characterizations the neutron radiations effects on crystals are also checked. The rapid progress in accelerator technologies enabled significant improvements in beam intensity for the purpose of higher machine luminosity. In parallel, the crystal technology has an increasingly important role, raises new questions on the crystal robustness. It is therefore, nine samples of silicon crystals have been exposed in the SCK-CEN BR2 reactor in Belgium to 2.5 x 10^{21} neutrons/cm^2 with the energy spectrum shown in Figure: 4. **6**. An irradiation capsule is shown in Figure: 4. **7**. Their channeling efficiency before and after the irradiation has been measured.

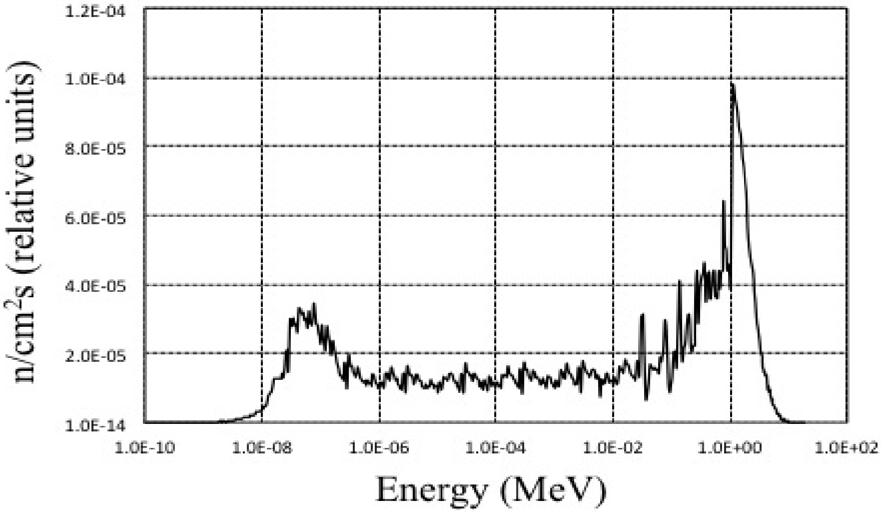

Figure: 4. 6 Energy spectrum of neutrons that have irradiated the nine crystal samples at the SCK-CEN BR2 neutron reactor.

Figure: 4. 7 Photograph of the nine silicon crystal samples wrapped in an aluminum protection foil (in the centre) ready to be closed in the irradiation capsule (up and down).

The novelty of this study is threefold. The first is the irradiation fluence, about one order of magnitude higher than the highest ever reached in the past. The second is the technique used to measure and compare the channeling efficiencies, based on the reconstruction of each single particle track using a high angular resolution telescope. This provide a more precise efficiency measurement if compared to the Rutherford backscattering (RBS) or particle flux counters used in the experiments previously reported. The third is the large number of identical samples tested (nine) that proves the repeatability and the reliability of the reported results.

The crystal thermo-mechanical robustness to a high intensity and high energy particle beam has been already studied at the HiRadMat facility at CERN, proving their reliability also in case of an accidental fast irradiation during injection or dumping operations in the LHC, or extraction ones in the SPS.

Conclusively, a detailed study of bent silicon crystal robustness up to 2.5x 10^{21} neutron irradiation has been carried out, which showed a reduction of ~8%in the channeling efficiency. Here it is a new and important proof for not only their reliability but also for application in high intensity machine such as SPS, LHC, HL-LHC and eventually FCC.

Recently, further tests have been carried out by UA9 at the CERN HiRadMat facility[28, 46, 47] to evaluate the robustness of crystal in case of accidental fast irradiation during machine operations. These crystals are of the same type used for LHC collimation and SPS extraction and they have been irradiated, bent by the original bending holder, with exactly the same proton beam extracted from the SPS or used to fill the LHC. The experimental results show no evident changes in beam steering performance after the irradiation, strengthening the conclusions reported here. The same HiRadMat test on the irradiated samples studied in this manuscript is scheduled. It will provide a robustness test in case of accidental fast irradiation at the end of their operational lifetime. Then, to evaluate the atomic structure damages, a deeper investigation after irradiation, (for example using the RBS technique) is planned.

The ultimate reliability test will be the performance study, at different energies, of high dose proton irradiated silicon crystals.

Table: 4. 1 Crystal Parameters

L_X [mm]	**L_Y [mm]**	**L_Z[mm]**	**Θ[μrad]**	**Eff. [%]**
1.00 ± 0.02	40.0 ± 0.1	2.00 ± 0.02	43-135 ± 1	69-66 ± 2

4.3. Results

We had the opportunity to analyze the data taken during the period from September 2018 to November 2018. There are eighteen crystals that are candidates for installing in LHC collimation system: TPC77, TPC79, APC79, APC80, APC84, APC85 and APC86, produced by Petersburg Nuclear Physics Institute (PNPI), and STF113, STF114, STF116, STF117, STF118, STF119, STF120, STF121, STF122 and STF123, produced by Instituto Nazionale di Fisica Nucleare (INFN-Fe)[48]. In addition, three candidates for installing in SPS, TCP72, ACP82, ACP83 and a new self-standing crystal STF115, with a special covering that produces self-bending, I analyzed the crystals STF123, STF126, ACP83 and ACP85 and found it very similar to the previous results reported in[49]. For example the results of STF126 and ACP85 (in comparison with the previous results) are given in Table: 4.2 and Table: 4.3 respectively. Similarly results of radiation tests for the aforementioned nine crystals are given in Table: 4.4.

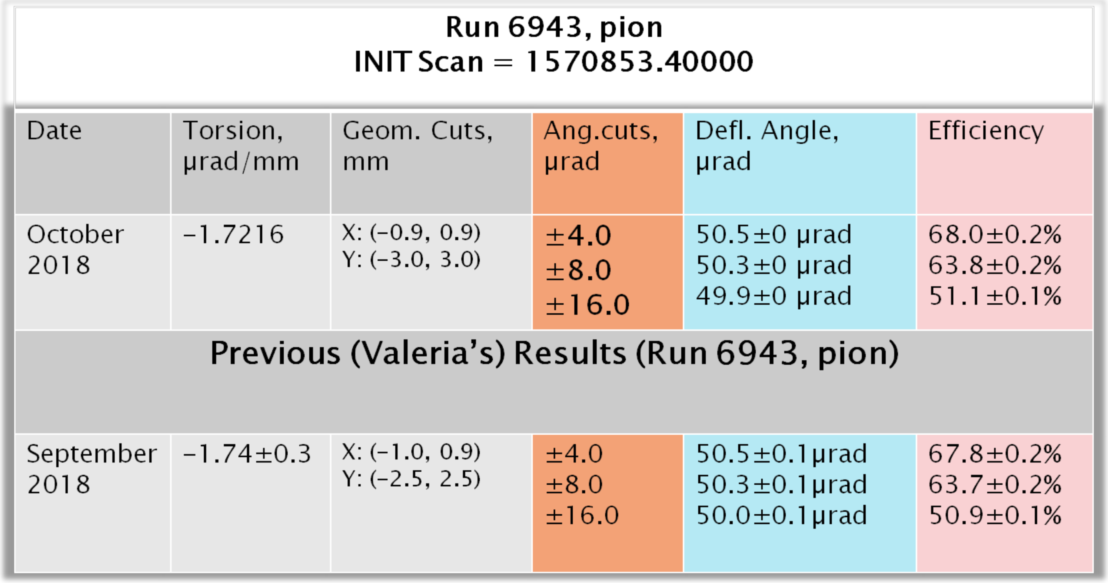

Run 6943, pion
INIT Scan = 1570853.40000

Date	Torsion, µrad/mm	Geom. Cuts, mm	Ang.cuts, µrad	Defl. Angle, µrad	Efficiency
October 2018	-1.7216	X: (-0.9, 0.9) Y: (-3.0, 3.0)	±4.0 ±8.0 ±16.0	50.5±0 µrad 50.3±0 µrad 49.9±0 µrad	68.0±0.2% 63.8±0.2% 51.1±0.1%

Previous (Valeria's) Results (Run 6943, pion)

Date	Torsion, µrad/mm	Geom. Cuts, mm	Ang.cuts, µrad	Defl. Angle, µrad	Efficiency
September 2018	-1.74±0.3	X: (-1.0, 0.9) Y: (-2.5, 2.5)	±4.0 ±8.0 ±16.0	50.5±0.1µrad 50.3±0.1µrad 50.0±0.1µrad	67.8±0.2% 63.7±0.2% 50.9±0.1%

Table: 4. 2 Analysis result of crystal STF126

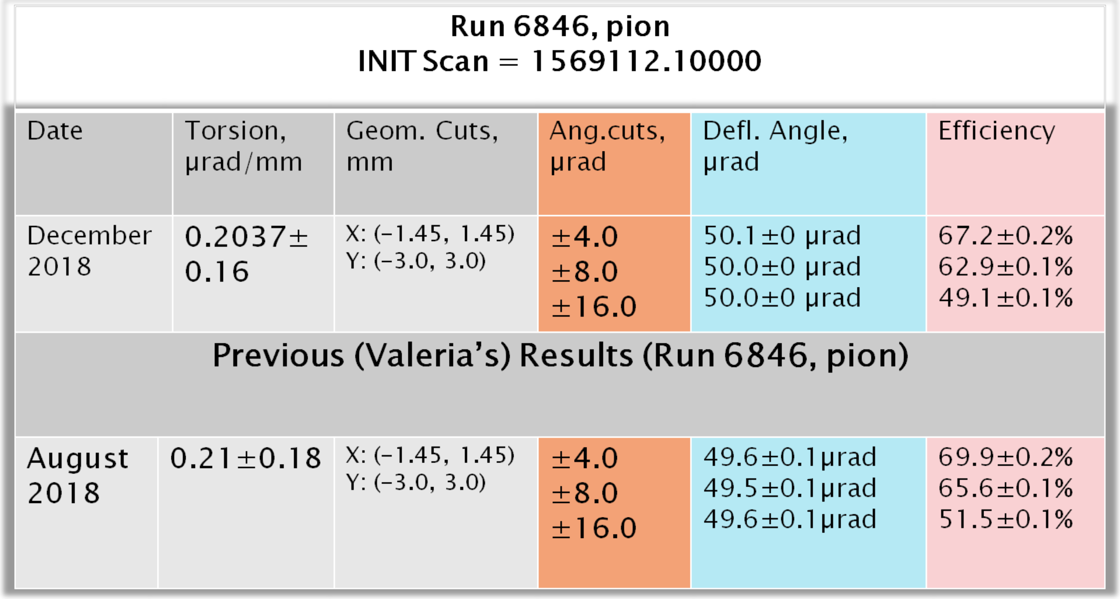

Run 6846, pion
INIT Scan = 1569112.10000

Date	Torsion, µrad/mm	Geom. Cuts, mm	Ang.cuts, µrad	Defl. Angle, µrad	Efficiency
December 2018	0.2037± 0.16	X: (-1.45, 1.45) Y: (-3.0, 3.0)	±4.0 ±8.0 ±16.0	50.1±0 µrad 50.0±0 µrad 50.0±0 µrad	67.2±0.2% 62.9±0.1% 49.1±0.1%

Previous (Valeria's) Results (Run 6846, pion)

Date	Torsion, µrad/mm	Geom. Cuts, mm	Ang.cuts, µrad	Defl. Angle, µrad	Efficiency
August 2018	0.21±0.18	X: (-1.45, 1.45) Y: (-3.0, 3.0)	±4.0 ±8.0 ±16.0	49.6±0.1µrad 49.5±0.1µrad 49.6±0.1µrad	69.9±0.2% 65.6±0.1% 51.5±0.1%

Table: 4. 3 Analysis result of crystal ACP85

Table: 4. 4 Efficiency before and after radiation

Crystal Sample	**$\Theta[\mu$rad] Before**	**Eff. [%] Before**	**$\Theta[\mu$rad] After**	**Eff. [%] After**
1	129 ± 1	66 ± 2	92 ± 1	60 ± 2
2	43 ± 1	69 ± 2	108 ± 1	58 ± 2
3	121 ± 1	66 ± 2	104 ± 1	57 ± 2
4	129 ± 1	66 ± 2	117 ± 1	57 ± 2
5	124 ± 1	67 ± 2	72 ± 1	60 ± 2
6	117 ± 1	66 ± 2	70 ± 1	60 ± 2
7	125 ± 1	66 ± 2	94 ± 1	59 ± 2
8	122 ± 1	66 ± 2	76 ± 1	60 ± 2
9	135 ± 1	69 ± 2	70 ± 1	60 ± 2

Chapter 5
The Cerenkov proton Flux Monitor for the UA9 Experiment at SPS

Together with the quantitative understanding of channeling and volume reflection processes, the main objective of the UA9 experiment is to reveal the practicability of a crystal-assisted halo collimation, qualifying this technology as a better option than the standard multi-stage collimation in high energy Hadron machines. The major installation of this experiment in the Long Straight Section 5 (LSS5) of the CERN SPS basically consists of a prototype of a crystal-assisted collimation system. It is prepared from pre-existing optical elements of the SPS machine and new installation including goniometers to operate 5 different crystals [50] used as primary collimators, one movable absorber and several scrapers. A network of detectors near to the UA9 installations and around the machine measures the beam losses and provides an estimate of the collimation efficiency of the crystals.

To fully characterize this collimation system, it is fundamental to progressively monitor the flow of the halo particles diffusing to the crystal as well the channeled beam steered by the crystal onto the absorber. In the past years the crystal extracted flux estimation has been performed indirectly by the variation of the primary beam intensity measured by the Beam Current Transformer (BCT [51]). Unluckily this measurement is intrinsically affected by the losses in various locations of the machine whose contribution to the variation of the primary beam can't be discriminated from the one due to the crystal. Moreover in the SPS, BCTs are optimized for beam intensities larger than 10^9 particles with a resolution of 5% and since the expected crystal extracted flux is of the order of $10^5 - 10^7$ p/s, the BCT indirect measurement represents a reliable measurement just if it is integrated over some tens of seconds. The Medipix detector [52], located in a Roman Pot about 40m downstream the crystals, can directly measure the extracted beam. The limitation of this measurement depends on the window (0.2mm of Aluminum) of the Roman Pot enclosing the detector; the secondary particles that are created by the interaction of protons inside this window can affect the counting of the impinging protons affecting the resolution of the measurement.

To overcome such limitations and measure the proton flux in an absolute way, the UA9 collaboration started an R&D program in 2012 with the aspire of building a proton flux monitor for low intensities directly hosted in the beam pipe vacuum and able to deliver the flux measurement with a resolution of 15% several times per second.

In this chapter several topics are taken from [50] where the CpFM detector chain is described in more detail. Starting from the detector requirements all the design choices are discussed, together with the mechanical integration of the detector and the electronic readout which is important for the easy understanding of next chapters.

5.1. Requirements of CpFM detector

The CpFM detector has been designed as an ultra-fast and high resolution proton flux monitor. It is use to give the measurement of the crystal-extracted halo beam from inside the beam pipe vacuum of the CERN-SPS and discriminates the signal impending from various bunches of protons. The design choices were therefore led by the need to get very high performances matching at the same time with the SPS environmental specifications, especially concerning the vacuum and the high radiation. The requirements that have been taken in account for this detector are listed below:

i. **Vacuum compatibility.** The detector has to be installed inside the SPS beam pipe vacuum (10^{-9} mbar) for the reason to avoid the interaction of the protons with the vacuum-air interface or as in the case of the Roman Pot, with the primary vacuum-secondary vacuum interface. This imposes a careful selection of the material used at least for the protons-sensitive part of the detector. It has to be made with non-degassing materials and additionally treated to be well-matched with the surface cleanliness levels specified by CERN [53].

ii. **Impedance compatibility.** The device should represent low impedance to the beam in order to avoid the production of beam instabilities.

iii. **Occupancy and mobility.** The detector chain must be mounted in an allocated space in the accelerator tunnel passage. Moreover, it has to be movable in the direction transversal to the beam to allow measurements at different apertures of the collimator system and to avoid interfering with the beam during standard machine operations.

iv. **Radiation hardness.** When positioned in operational location, in interaction with the beam halo, the counter will have to face very high amount of radiation (tens of kGy/year). In parking point (namely around 40 cm from the beam pipe) the device will be constantly exposed to the SPS radiation. The latter is characterized by the shower particles (photons, pions, neutrons, protons) generated by beam losses at the aperture restrictions of the accelerator. Here the expected neutron flux is around $10^{14}/\text{cm}^2$ per year while the integrated dose is around 4 kGy per year. It is therefore fundamental paying attention to the radiation stiffness of the detector chain and to carefully think about the location of the readout electronics.

v. **Timing.** During UA9 operations the bunch length is close to 2 ns and the minimal bunch distance is 25 ns. The detector has to be able to measure the number of protons extracted by the crystal from a single bunch of the SPS. This means that the detector response has to be quick enough to discriminate the signals of two consecutive bunches (response time close to the bunch length) even if it is not needed to deliver the flux measurement for each bunch. The ideal frequency of the measurement should be the same of the SPS revolution frequency, 43 kHz. This should be taken in account in the selection of the optimal readout electronics.

vi. **Dynamic range.** The counter has to intercept the halo particles extracted by the upstream crystal. In the SPS the single bunch standard intensity used during UA9 experiments is around 10^{11} protons and the crystal extracts from 10^5 up to 10^7 p/s per bunch, depending on the distance of the crystal from the beam core. This automatically defines the dynamic range of the detector that has to resolve the signal generated by a single proton up to about few hundred of protons.

5.2. Designing the detector layout

Numerous investigations and experimental tests have been performed in the last few years to carefully select all the components of the detector chain. The conceptual sketch of the detector chain is reported in Figure: 5.1. The sensitive element consists in fused silica bar acting both as Cherenkov radiator and light guide. When a relativistic charge particle passes through the bar it creates Cherenkov light which is then transported to the other tip of the bar through internal reflection. To convey the light signal outside the beam pipe a standard quartz viewport is used. An optical fused silica fibers bundle is mechanically coupled to the viewport and guides the light to the PMT window, 1m away from the beam pipe. The PMT signal is transmitted up to a low radiation area through a low attenuation cable and it is readout by an ultra fast analog memory. The bar can slowly approach the extracted beam through a movable bellow on which the viewport is built up.

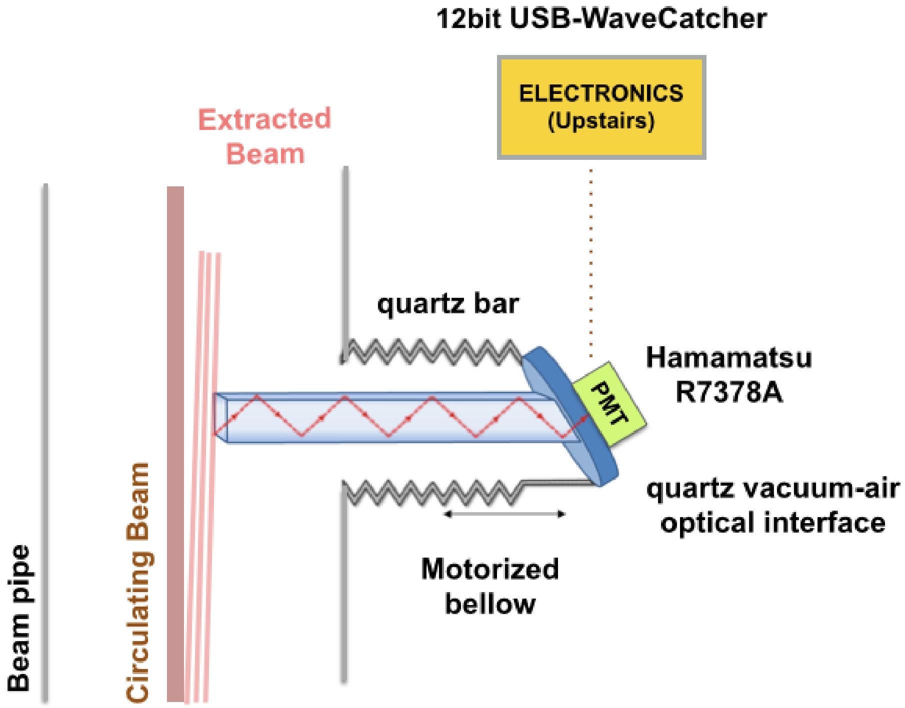

Figure: 5. 1 Sketch of CPFM

5.2.1. The Cherenkov radiator

When choosing the sensitive element of the detector, different options have been considered: silicon and gas sensors were discarded because they do not comply with the vacuum requirements while scintillation materials were not enough radiation resistant. Finally it was decided to use a Fused Silica radiator exploiting the Cherenkov light production mechanism. Fused Silica (or fused Quartz (SiO2)) is a very pure glass with a long absorption length in the ultraviolet (see Table: 5.1), were most Cherenkov photons[4] are produced. It is also characterized by a high resistance to radiation and for this reason it was an optimal solution for the CpFM operational environment. Moreover the Cherenkov light mechanism offers some useful advantages:

---

[4] Cherenkov light emission spectrum is proportional to $\frac{1}{\lambda^2}$

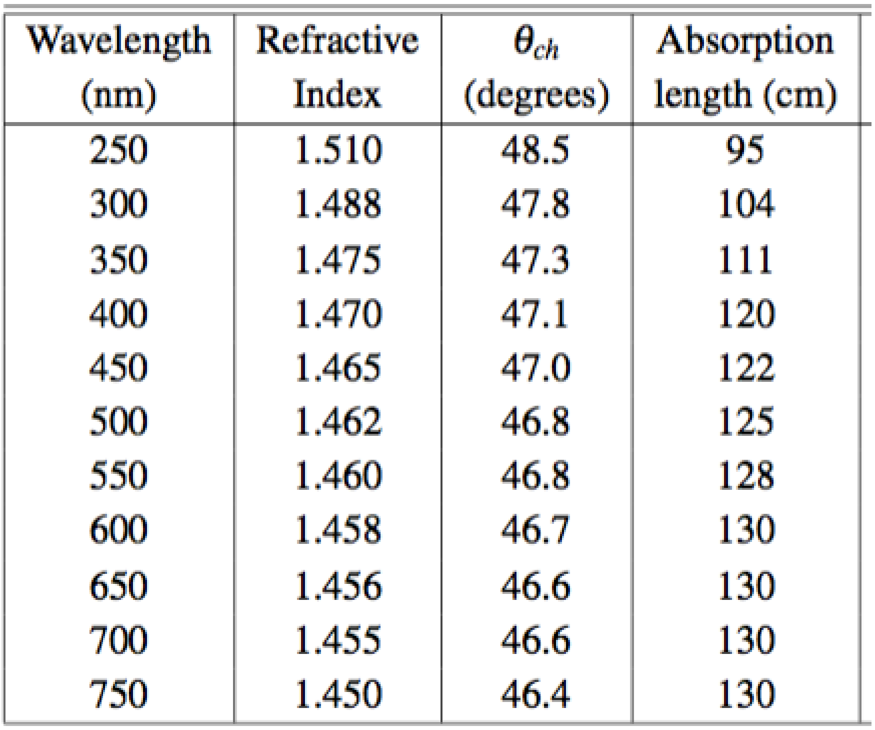

Wavelength (nm)	Refractive Index	θ_{ch} (degrees)	Absorption length (cm)
250	1.510	48.5	95
300	1.488	47.8	104
350	1.475	47.3	111
400	1.470	47.1	120
450	1.465	47.0	122
500	1.462	46.8	125
550	1.460	46.8	128
600	1.458	46.7	130
650	1.456	46.6	130
700	1.455	46.6	130
750	1.450	46.4	130

Table: 5. 1 Wavelength dependence of some important properties of Fused Silica

i. It is a threshold process. Just charged particles travelling faster than the speed of the light in the medium ($v > c/n$, with n the medium's index of refraction) lose energy in the form of Cherenkov radiation. This automatically cut the low particle background.
ii. It is intrinsically fast. Cherenkov light is a promptly emitted and therefore ideal to match with the SPS timing requirements (see sec 5.1).
iii. Directionality. The light is emitted along the particle's path on a cone with half opening characteristic angle θ_c (Cherenkov angle) which depends on the β of the particle and on the refraction index of the medium (which depends on the light wavelength λ) according to $\theta_c = \cos^{-1}(1/\beta n)$.

For the geometry of the radiator the starting idea was to shape it as a bar, to serve both as a Cherenkov radiator and as a light guide. Indeed, if the particles are going parallel to the walls of the radiator bar, all the Cherenkov light that hits the sides is totally internally reflected, as the Cherenkov angle θ_c is less than the total internal reflection angle[5] .Because the refractive index depends on the light wavelength, in fused silica θ_c from 48.5^0 at 250 nm to 46.4^0 at 750 nm.

---

[5] defined with respect to the surface, not the normal and given by the Snell's law: $\theta_{TIR} = \arcsin(1/n)$

This chromaticity issue affects the time resolution of the detector on the constraints scale (photons with different λ have different phase velocity and path length) therefore it will not be discussed here as this detector was not conceived to perform such a challenging timing measurement.

An extensive simulation campaign [54] has been performed to define the shape of the radiator bar as well as the required polishing and flatness of the surfaces. Several geometries were studied: from the simplest one, the I-shape bar to the L-bar and other more complex geometries designed in the attempt to include in the same object the radiator and the vacuum-air interface (very difficult to be realized). Simulations selected the L-shape bar as the optimal geometry. This bar is L-shaped with a 90^0 corner. The light is produced in the short leg (30mm long) of the L, parallel to the particles direction, and continue to be totally internally reflected until the tip of the long leg, called hereafter light guide. In fact since $n(\lambda) > \sqrt{2}$ so that $\theta_c > 45^0$ as it is for Quartz, the light that passes up the light guide bar has an angle with respect to the surface that is $< 45^0$, less than θ_{TIR}, and total internal reflection is sustained.

Simulations pointed out another fundamental issue related to the quality of the quartz surface. Depending of the length and on the section of the bar, the photons will rebound several tens of times prior to exiting the bar, therefore to avoid light losses, the surface reflectivity R_s has to be as close as possible to one (e.g. if R_s= 0.98 and photons needs about 40 reflections to reach the end of the bar, the light yield is decreased of a factor $1/(98)^{40}$ = 2:2). For the CpFM bar the R_s requirement was 0.99. This value of R_s sets therefore the requirements for the surface flatness to be >100nm and for the quality of the polishing to be < 100nm (RMS).

L-bar and I-bar have been selected to be produced the cherenkov light. The L-bar has optimal geometry according to simulations therefore it is selected as main source to produce the cherenkov from passage of protons and the I-bar, being easier to cut and polish is selected as back-up solution. Both bars were produced using the Fused Silica Spectrosil 2000 and with the same section and length (5mm x 10mm x 360mm). For the L-bar the manufacturer succeeded in cutting the bar with the right angle but not in polishing it with the requested accuracy. Figure: 5.2 (b) shows the results of the comparative test between the L-bar and the I-bar performed at the BTF facility with 450 MeV electrons. The bars were displaced by 5 mm and mounted on a translation stage to scan the bars response as a function of the impact position of the electrons beam on the bars (the x axis in Figure: 5.2 (a) is referred to the impact position on the L-bar). As we can see the L bar (red dots) displays a larger signal in the first fraction of the scan, corresponding to the beam

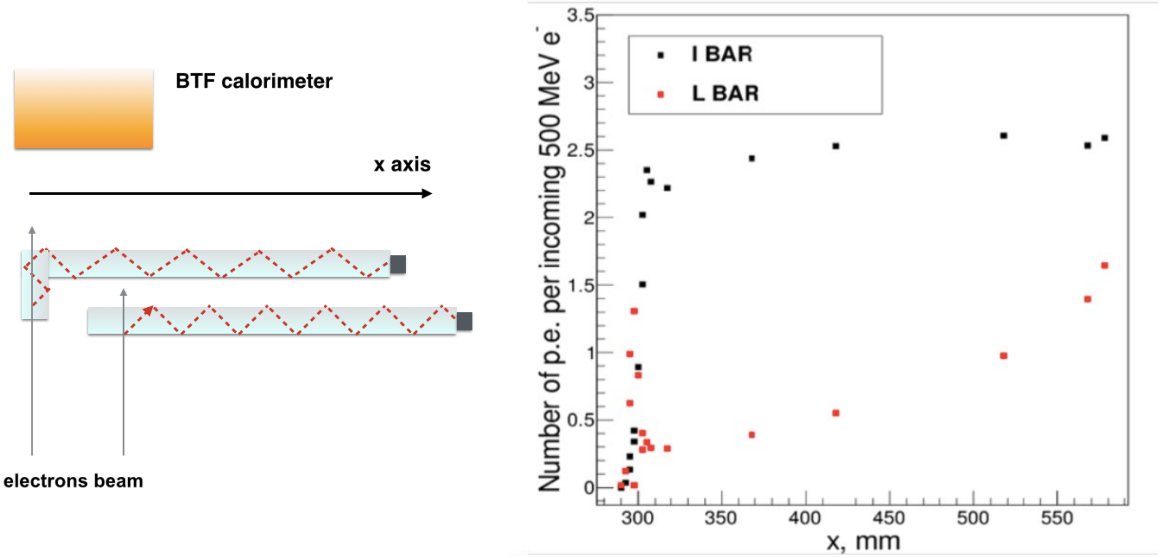

(a) L-bar and I-bar beam test configuration. Each bar is readout by aR762 Hamamatsu PMT and the signalsare normalize to the number of electrons provided by the downstream BTF calorimeter.

(b) CpFM signal (number of ph.e per incident electron) as a function of the impact position of the electrons in the quartz bars (red dots L-bar, black dots I-bar.

Figure: 5. 2 L-bar and I-bar comparative test with 450 MeV electrons at the Beam Test Facility in LNF [54].

When the beam hit the bar on the light guide and crossing the short leg of the L (30mm thick) the signal is reduced by a factor around 2. If all the photons produced within the short leg were transmitted to the end of the bar this value should be equal to 6, as the light produced is proportional to the crossed length which is equal to 30mm in the leg and to 5mm in the light of guide. We can thus assume that this was due to a bad polishing (especially in the junction part) of the bar which has, moreover, a non uniform response also along the light guide. The behavior of the I-bar (black dots) is instead uniform and the photoelectron yield per electron is 5 times higher than in the L-bar when just the light guide is considered. For these reasons the I-bar was selected to be installed on the CpFM. At the end, two I-bars were installed, one for the proton flux measurement and the other one to monitor the background.

5.2.2. The fiber bundle

Using a fiber bundle to readout the CpFM signal 1m away from the pipe was not essential but it was chosen to include it in the detector design for the purpose of decreasing the radiation dose on the PMT and above all to test a configuration suitable for the LHC radiation environment, with the

Figure: 5. 3 The 4 meters bundles composed of 100 fibers each. The ends of the bundles match the shapes of the Quartz bars (rectangular section) and of the PMT window (round section) [54]

purpose to export the CpFM concept into LHC. The fibers selected are made by pure Fused Silica as the standard plastic fibers are not radiation resistant. The coating is made of Tefzel while the cladding is made of Fluorine doped Fused Silica. The numerical aperture is 0.22, therefore photons have to enter the fibers with an angle smaller than the acceptance angle (8^0) to internally be transmitted to the end. This feature sets mechanical constraints on the rear edge of the bar and on the flange. In fact to optimize light collection the collection surface has to be perpendicular to the direction of the photons. This could be obtained inclining the bar at θ_c (47^0) with respect to the direction of the particles (configuration b, Figure: 5.4) but this solution was discarded since the integration of an inclined bar would have required a large aperture in the tank hosting the detector. Another solution was found through simulations [54]. They showed indeed that when particles intercept the bar at 90^0, the polar angle distribution of the photons emerging from the read-out surface of Quartz is peaked at 47^0, as also confirmed by an experimental test performed at the BTF facility in LNF. For this reason it was decided to cut the bar in such a way the end surface is inclined by 47^0 and to keep the radiator perpendicular to the beam direction (configuration c, Figure: 5.4). Obviously also the viewport was therefore produced inclined by the same angle. Although this solution improve the light yield at the PMT photocathode, the small acceptance angle jointly with the fill factor of the fibers (active area is not equal to the total one due to the dead spaces between the fibers inside the bundle packing) were anyway responsible for a strong light loss. It was first estimate by simulations and then observed during BTF test that a 4 meters bundle of 100 fibers (see Figure: 5.3) decreases the PMT signal of a factor of 10 with respect to the configuration with a direct coupling between the bar and the PMT. In Figure: 5.5 the results of Geant4 simulations of the number of photoelectron produced at the PMT photocathode output by 270 GeV proton crossing a quartz bar are shown for the direct coupling and with the fibers bundle. Cherenkov photons are produced inside the radiator, along with the proton trail with wavelength-dependent optical properties of Fused Silica (refractive index and free path length). The propagation of the generated photons takes into account the quality of the radiator surface as well as its bulk properties (inclusions concentration). The quantum efficiency and collection efficiency of the PMT with its Bialkali photocathode are considered. The coupling between the radiator and the photo detector or the fibers bundle is supposed to be perfect; for that reason the simulation provides an upper bound of the number of generated photoelectrons.

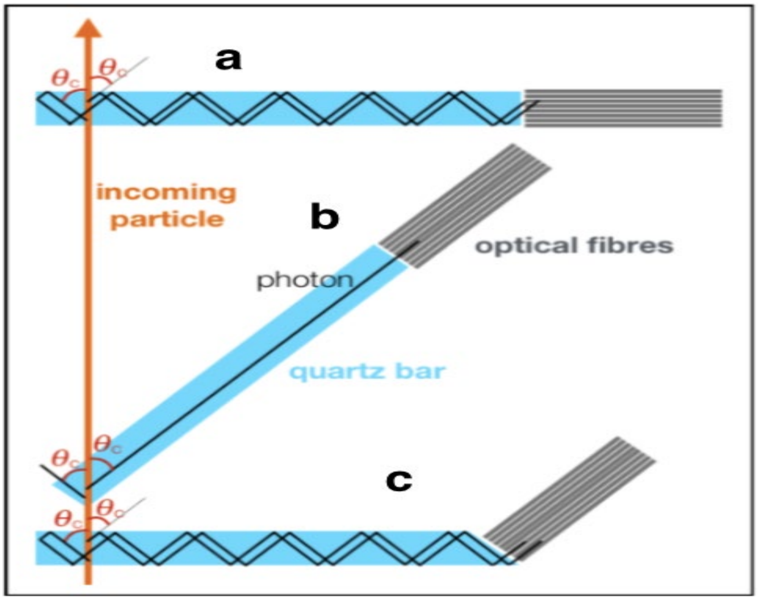

Figure: 5. 4 Effect of the Cherenkov angle on the collection of the signal at the end of the radiator Configuration a) was discarded it was not optimal for the light collection. Configuration b) was not feasible for mechanical constraints. Configuration c) was the one chosen. [28]

5.2.3. The optical and vacuum interface

The light generated in the radiator located in the beam pipe primary vacuum must be transmitted outside to be readout. In order to limit the number of interfaces traversed by light it was attempted to feed the bar through a vacuum flange and braze the ensemble to ensure the vacuum tightness.

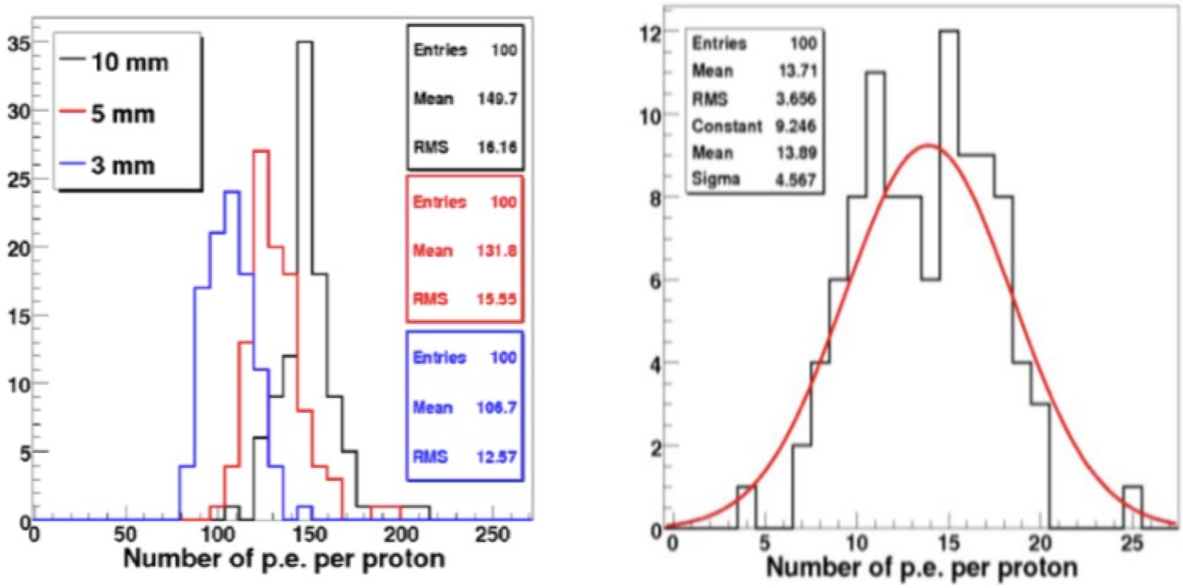

(a) Distribution of the number of p.e. per incoming proton produced at the PMT photocathode output for a direct coupling between the radiator and the PMT and for 3 different Quartz thickness (3, 5 and 10 mm).

(b) Distribution of the number of p.e. per incoming proton, crossing a 5m thick bar, produced at the PMT photocathode after 4m of fibers bundle.

Figure: 5. 5 Geant4 simulation of the number of photoelectron produced for 270 GeV incoming proton at the photocathode output with and without fibers bundle. [54]

Unfortunately the company in charge to realize the brazing failed in doing this, explaining that fused silica bar appears to cool and heat quicker than the stainless flange. This causes a stress point for the Fused Silica and breaking the bar. Another company recently succeeded to brazing a round bar into the flange and further developments of this technique are still ongoing. However for the installation of the CpFM it was decide to use a standard quartz viewport with a thickness of 3 mm and inclined at 47^0 with respect to the beam pipe (Figure: 5.6). It was chosen quartz glass with refraction index very close to the one of the bar and the bundle, to maximize the light transmission. Nevertheless, it has been estimated that the viewport is accountable for a reduction factor of 2 in the light reaching the PMT.

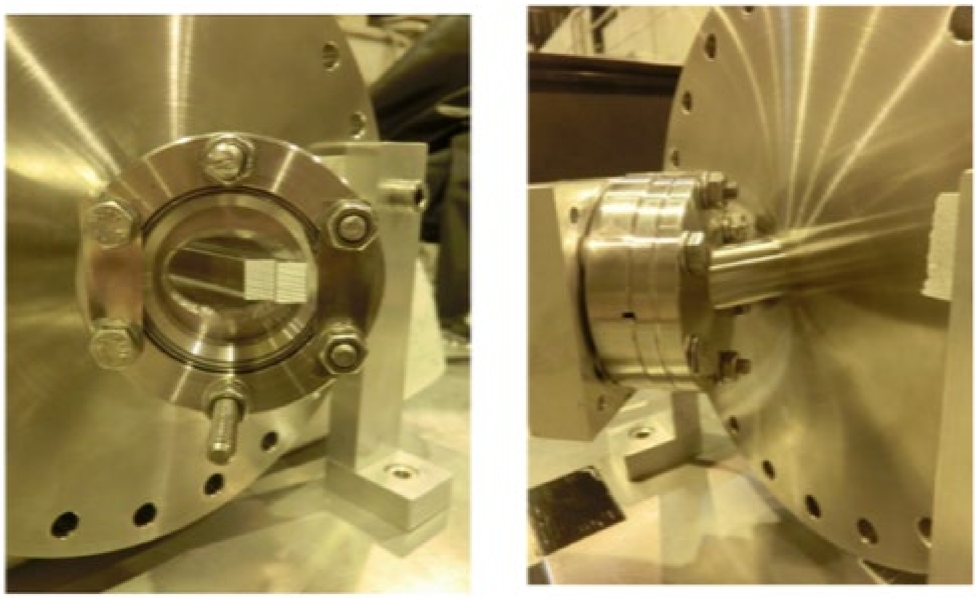

Figure: 5. 6 The quartz viewport connected to the stainless steel flange. The viewport is inclined at $47^0$with respect to the beam pipe and connected to the fiber bundle. [54]

5.2.4. The Photodetector

The optimal PMT for the CpFM has to operate in a quite hostile environment (10^{12} neutrons/year at 1m from the beam pipe[50]). This automatically discarded compact PMTs with metal channel dynodes because of their outside layer made with resins that are not radiation-resistant. It has to be characterized by a good sensitivity in the ultraviolet range and by a minimum gain of 10^5. The high gain is needed because the amount of light emitted through the Cherenkov mechanism in 5mm of Fused Silica by a particle (this is the thickness of the CpFM bar crossed by protons) is very small. To estimate it we can use the rigorous formula [55] for a particle of charge *ze* producing photons in the frequency range v_1-v_2 :

$$\frac{dE}{dx} = \frac{z^2}{2}\frac{e^2}{hc}\frac{mc^2}{e^2}\left(\frac{(hv_2)^2 - (hv_2)^2}{mc^2}\right)sin^2\theta \tag{5.1}$$

Figure: 5.7 shows the results of GEANT4 simulations of the number of photoelectrons generated at PMT photocathode output by 270 GeV protons crossing a *5mm* thick I quartz bar *(5 x 5 x 100m^3)* when the coupling between the bar and the PMT is straight and considered as perfect (no loss at interface). Considering the reductions due to the viewport (factor 2) and the bundle (factor 10), less than 2 ph.e per proton are expected. This is the reason for which a high gain PMT is really fundamental. The PMT selected for the CpFM is the HAMAMATSU R7378. Cherenkov photons were produced in the radiator, along the proton trail with wavelength-dependent optical properties of Fused Silica. The propagation of the produced photons takes into account the quality of the radiator surface as well as its bulk properties (inclusions concentration). The quantum efficiency and collection efficiency of the PMT with its Bialkali photocathode were taken into account. The coupling between the radiator and the PMT is considered as perfect [54].

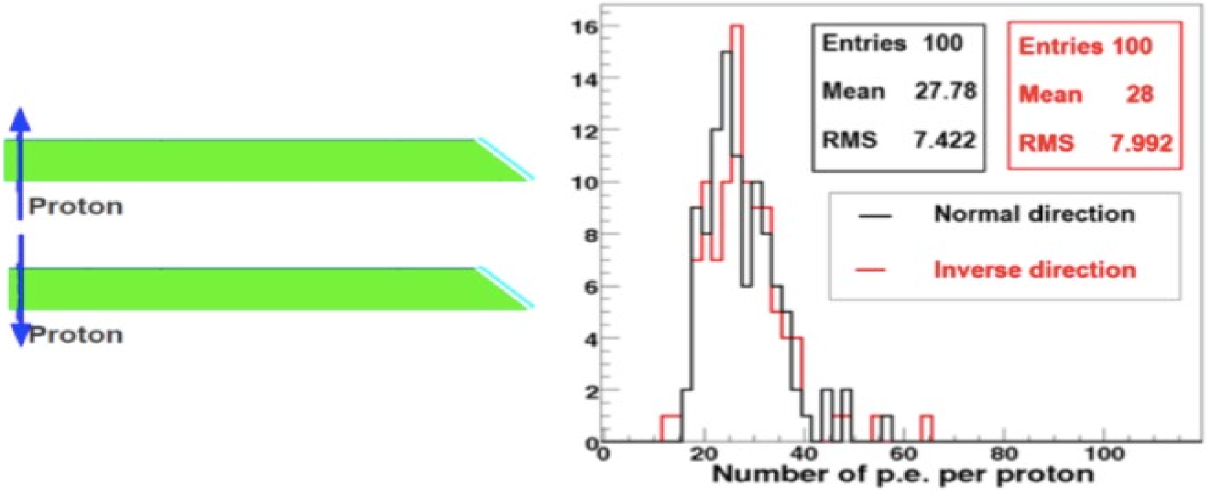

Figure: 5. 7 (Left) sketch of a Quartz I-bar. (Right) Distribution of the number of p.e. per incoming proton generated at the PMT photocathode in direct coupling for normal and inverse direction of the protons.

The main features of the PMT are shown in Figure: 5.8. Also the gain characterization table for the PMTs selected to be used for the detector is shown in Table: 5.2.

Bias (V)	**BA 1511**	**BA 1512**	**BA 1513**
700	2.90 E+05	2.33 E+05	3.332 E+05
750	4.82 E+05	4.00 E+05	5.53 E+05
800	7.75 E+05	6.65 E+05	8.94 E+05
850	1.21 E+06	1.07 E+06	1.40 E+06
900	1.84 E+06	1.68 E+06	2.14 E+06
950	2.74 E+06	2.57 E+06	3.20 E+06
1000	4.00 E+06	3.84 E+06	4.96 E+06
1050	5.73 E+06	5.63 E+06	6.74 E+06
1100	8.07 E+06	8.12 E+06	9.52 E+06

Table: 5. 2 Gain characterization table for the two PMTs selected to be mounted on the UA9-CpFM (BA1511 and BA1512) and on the SE-CpFM (BA1513). The table has been provided by the constructor.

The radiation hardness of the PMT is guaranteed by the synthetic silica window that unlike the Borosilicate does not demonstrate loss of transmittance due to the coloring of the glass when exposed to the radiation. Moreover, the synthetic silica window used in combination with the Bialkali photocathode produces a spectral response ranging from 160 to 650nm which makes this PMT suitable for the Cherenkov light spectrum (Figure: 5.9). The gain ranges from 10^5 to 10^7 and the time response is fast (anode pulse rise time ≈ 1.5 ns and recovering time < 10 ns). As the CpFM operation time is limited to the UA9 beam time in SPS (24h x 3 per year), the lifetime of the PMT should not be affected by accumulated charge effects. Moreover, as it was decided to readout the CpFM signal 1m away from the pipe, where the radiation flux and dose are less intense (10^{12} neutrons/cm^2 and several tens of Gray per year), the PMT should not suffer damages due to radiation. Nevertheless periodical checks of the PMT stability (dark current and response under illumination), are scheduled during each technical stop of the SPS, therefore every 3 months. Measurements of the PMT linearity as a function of the incident flux were performed with a blue LED (405nm_2 nm) biased by a pulse generator producing 10 ns light

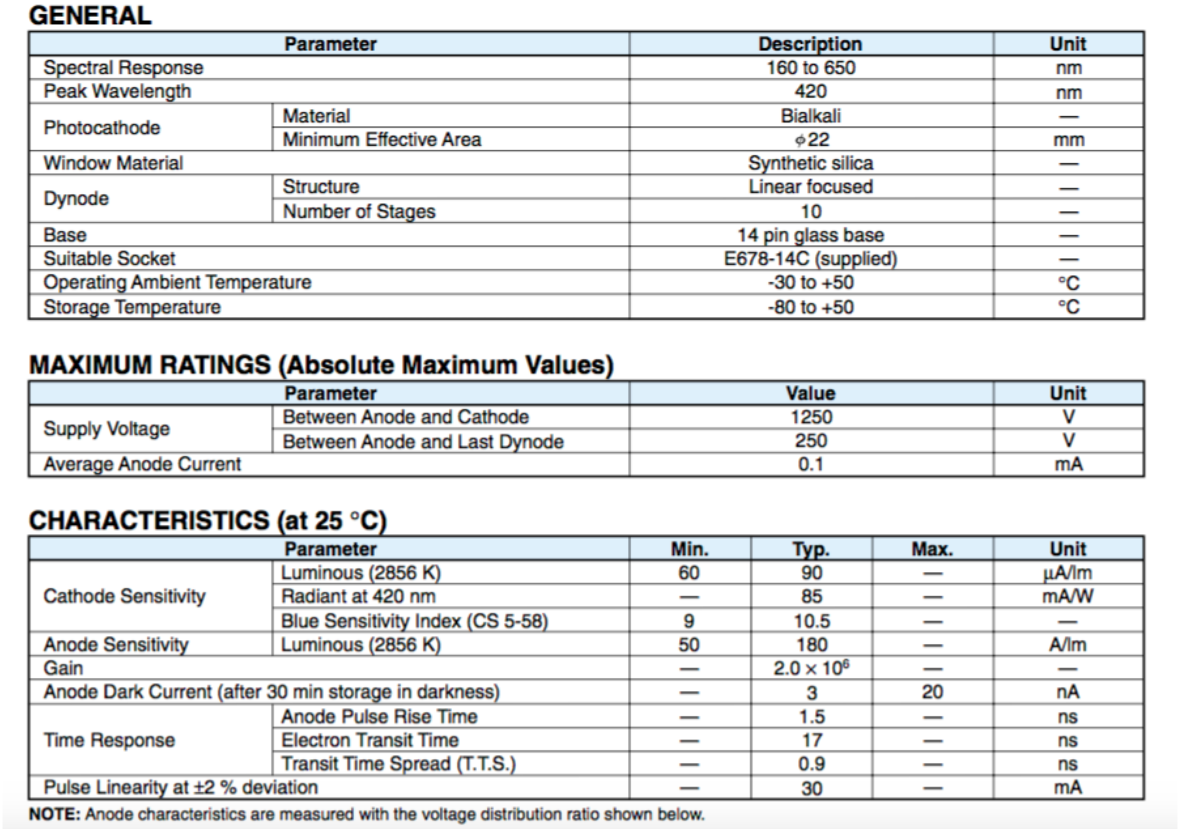

GENERAL

Parameter		Description	Unit
Spectral Response		160 to 650	nm
Peak Wavelength		420	nm
Photocathode	Material	Bialkali	—
	Minimum Effective Area	ϕ22	mm
Window Material		Synthetic silica	—
Dynode	Structure	Linear focused	—
	Number of Stages	10	—
Base		14 pin glass base	—
Suitable Socket		E678-14C (supplied)	—
Operating Ambient Temperature		-30 to +50	°C
Storage Temperature		-80 to +50	°C

MAXIMUM RATINGS (Absolute Maximum Values)

Parameter		Value	Unit
Supply Voltage	Between Anode and Cathode	1250	V
	Between Anode and Last Dynode	250	V
Average Anode Current		0.1	mA

CHARACTERISTICS (at 25 °C)

Parameter		Min.	Typ.	Max.	Unit
Cathode Sensitivity	Luminous (2856 K)	60	90	—	µA/lm
	Radiant at 420 nm	—	85	—	mA/W
	Blue Sensitivity Index (CS 5-58)	9	10.5	—	—
Anode Sensitivity	Luminous (2856 K)	50	180	—	A/lm
Gain		—	2.0×10^6	—	—
Anode Dark Current (after 30 min storage in darkness)		—	3	20	nA
Time Response	Anode Pulse Rise Time	—	1.5	—	ns
	Electron Transit Time	—	17	—	ns
	Transit Time Spread (T.T.S.)	—	0.9	—	ns
Pulse Linearity at ±2 % deviation		—	30	—	mA

NOTE: Anode characteristics are measured with the voltage distribution ratio shown below.

Figure: 5. 8 Summary of the main characteristics of the CpFM PMT. (PMTr-7378a datasheet)

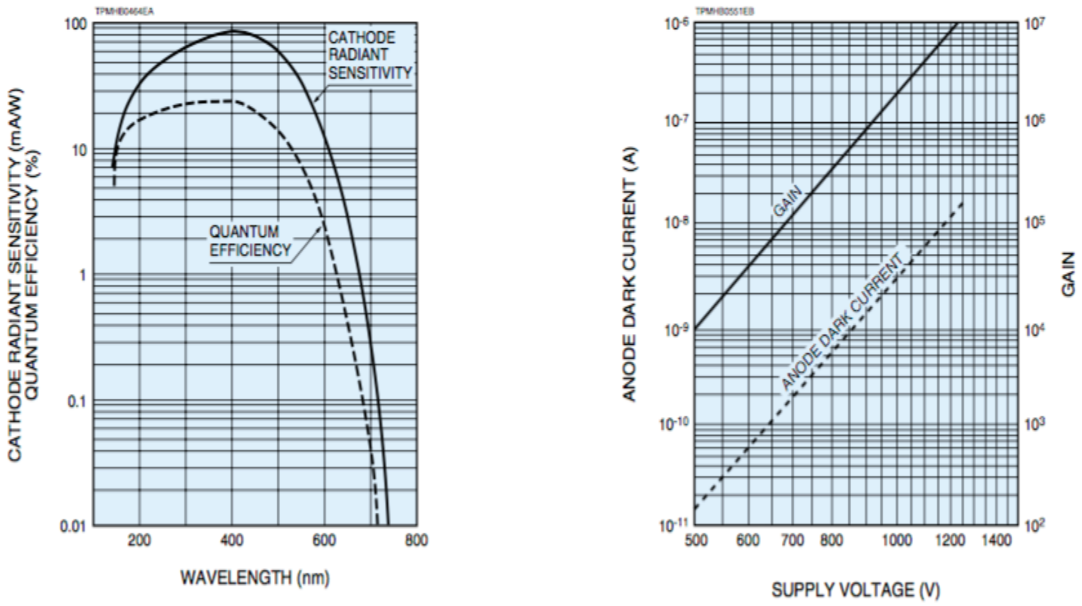

Figure: 5. 9 Typical spectral response (left) and typical gain and dark current characteristics for the CpFM PMT. [Pmt r-7378a datasheet," 2004. Available on line]

pulses with a frequency of 43 KHz to simulate the revolution frequency of SPS (and therefore the particles signal frequency on the detector). The outcomes of this test are fundamental to optimize the detector depending on the expected particle flux. In Figure: 5.10 are shown the linearity curves when the PMT is operated at 1000 V and 700 V (the UA9-CpFM PMT is usually operated at 1050V with protons and 700V during the Ions beam tests). Considering that the flux hitting the CpFM will not exceed few hundred protons per turn and that less than 5% of produced photons reach the PMT (because of the bundle and the viewport effect), it was assessed that no divider is required to improve the linearity of the PMT; therefore as a divider it has been chosen the standard one advised by HAMAMATSU.

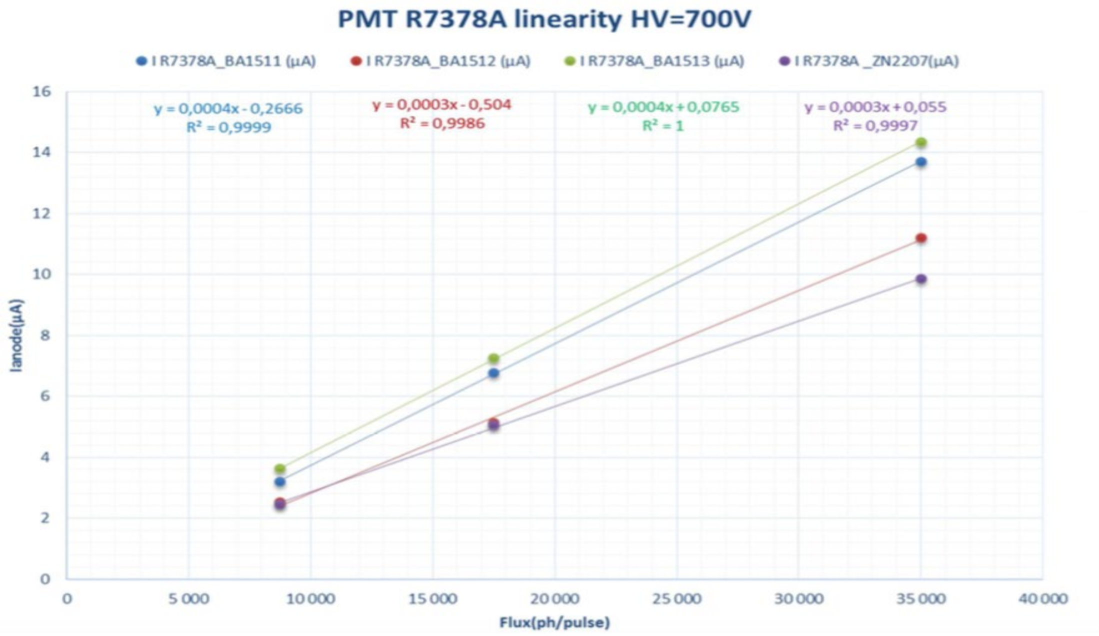

(a) Anode current as a function of the incident flux when the PMT is operated at 700V .

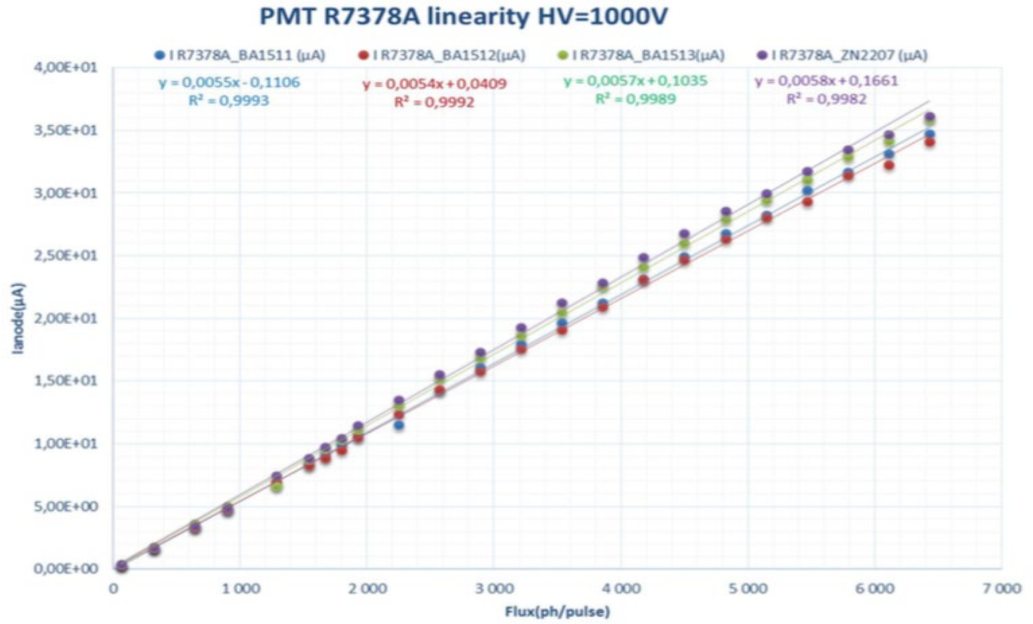

(b) Anode current as a function of the incident flux when the PMT is operated at 1000 V.

Figure: 5. 10 CpFM PMT linearity test as a function of the incident flux provided by a blue LED driven by a pulse generator set at 43 KHz. Each light pulse is 20 ns long[50].

5.3. Readout electronics (Wave Catcher board)

The Wave Catcher boards (Figure: 5.11) are 12-bit 3.2 GS/s digitizers based on the SAMLONG chip[56] fitted with a USB 2.0 interface for data transfer. The input dynamic range is 2.5 V_{pp} (DC coupled). The DC offset is changeable in the ±1.25V range via a 16-bit DAC on each channel (for the CpFM the 8-channels module is currently used). The signal analog bandwidth is 500 MHz at 3 dB. In case of the sampling frequency and the number of bits, it is fit for very fast signals. The analog input signals are constantly sampled within the SAMLONG chips (one chip each couple of channels) in a circular analog memory buffer (1024 cells) at the default sampling frequency of 3.2 GS/s (312.5 ps of sampling period); 6 other frequencies down to 0.4 GS/s can also chosen via software[6].

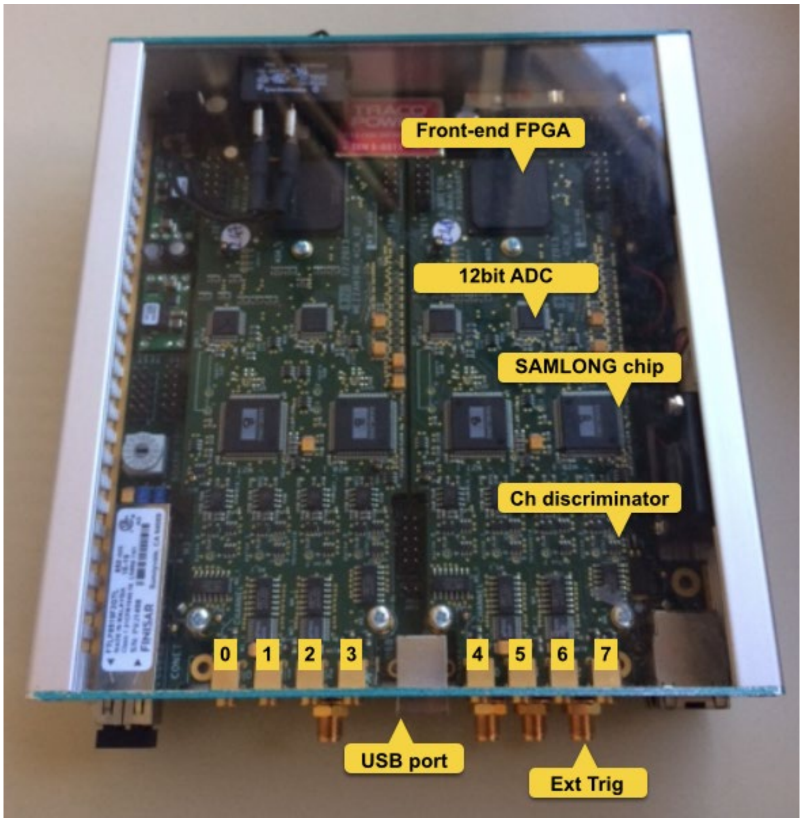

Figure: 5. 11 USB-Wave Catcher board. In the picture is shown the architecture of the board with the main components. The board is composed by two sub-units, each one with one FPGA handling 4 analog channels. Each couple of channels has their own SAMLONG chip and the12bit ADC. Every channel is equipped by a 16-but programmable discriminator for the trigger signal and for the hit monitor

---

[6] each sampling frequency is generated by a corresponding input clock which ranges from 25MHz for 400 MS/s up to 200MHz for 3.2 GS/s

As a trigger signal asserted, all analog memory buffers are frozen and consequently digitized with a resolution of 12 bits into a digital memory buffer. Moreover it is possible to move the 1024 sample window up to 63 time divisions further the trigger signal (the time division depends on the sampling frequency and corresponds to (1024*1/v)/20).

Each input channel is equipped with a discriminator using a 16-bit programmable threshold, which can generate the common board trigger, causing all the channels to obtain an event simultaneously. The common board trigger can also be provided outwardly through a software command or via the external trigger input connector (TTL or NIM signal), or by any combination of the channel discriminators and/or the external trigger signal. During the process of analog to digital conversion, the Wave Catcher cannot grip other triggers, and thus generates a dead time (maximum 125 μs, lessening proportionally with the recording depth thanks to the configurable record length). This sets the ultimate limit on the acquisition rate.

Each input channel is prepared with a hit rate monitor based on its own discriminator and on two counters providing the number of hits which pass through the programmed discriminator threshold (also during the dead time period) and the time elapsed with a 1 MHz clock. This permits measuring the hit rate with respect to the signal amplitude.

Every input channel is also equipped with a digital measurement block situated in the front-end FPGA (Field Programmable Gate Array) which permits taking out in real time all the key features from the signal baseline, peak, charge, time of the edges[7] in CFD (constant fraction discrimination) or fixed threshold modes. This block works with parameters fixed by user (see Figure: 5.12).

The board is interfaced to the computer via USB 2.0 port and dedicated software and libraries allow an easy handling of the board. The data recording rate limit is set by the maximum data flow that USB 2.0 port can handle (up to 30 MB/s, considering that just a couple of acquired channels produces 10 MB/s registering 1024 samples waveform) that could be even bigger than the maximum data flow that the software can digest. Therefore the data recording rate limit strongly depends on how many channels we want to acquire and on what we are interested in recording (rates, measurement from the block measurement, 1024 samples digitized waveform) and obviously on the PC speed. It was decided to acquire and registering CpFM data at 43 Hz

---

[7] rise time edge and falling time edge are measured starting from the beginning of the digitizer window thus they can be considered as the arrival time of the signal with respect to the signal which opens the acquisition window

frequency. In this way it is possible to acquire and register events from 3 channels (2 channels or the CpFM and 1 for the trigger) with the full data information package.

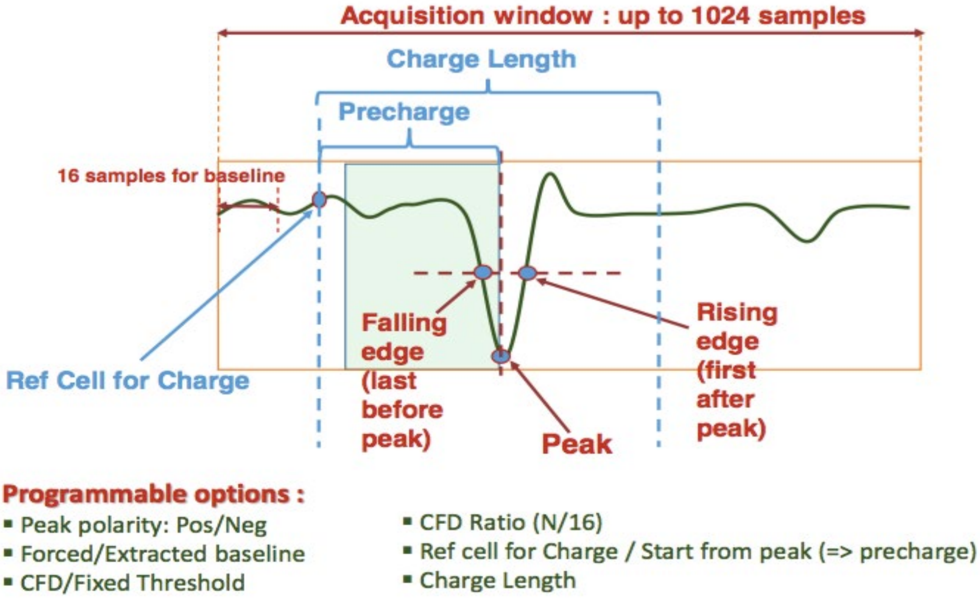

Figure: 5. 12 Conceptual scheme of the digital measurement block. Before being stored into the Digital Memory Buffer and made ready for readout in the shape of events data, the ADC outputs pass through the measurement block of the FPGA. The measurement block works with parameters fixed by user and listed in the picture to extract the main signal features. [57]

5.4. CpFM Detector

The CpFM detector was assembled and installed at the beginning of 2015 in the UA9 experimental area (Long Straight Section 5 of the SPS). In this section we will discuss the Final layout, Mechanical integration and Readout system of CPFM.

5.4.1. Ultimate Layout

The CpFM final layout is shown in Figure: 5.13. In its final version the CpFM consists in two identical Fused Silica I-bars displaced of 5 mm. One bar (also called CpFM 1) is 5mm closer than the other one to the circulating beam and it is devoted to the flux measurements. The other bar (also called CpFM 2), being retracted from the beam to be measured, is conceived to provide background measurements.

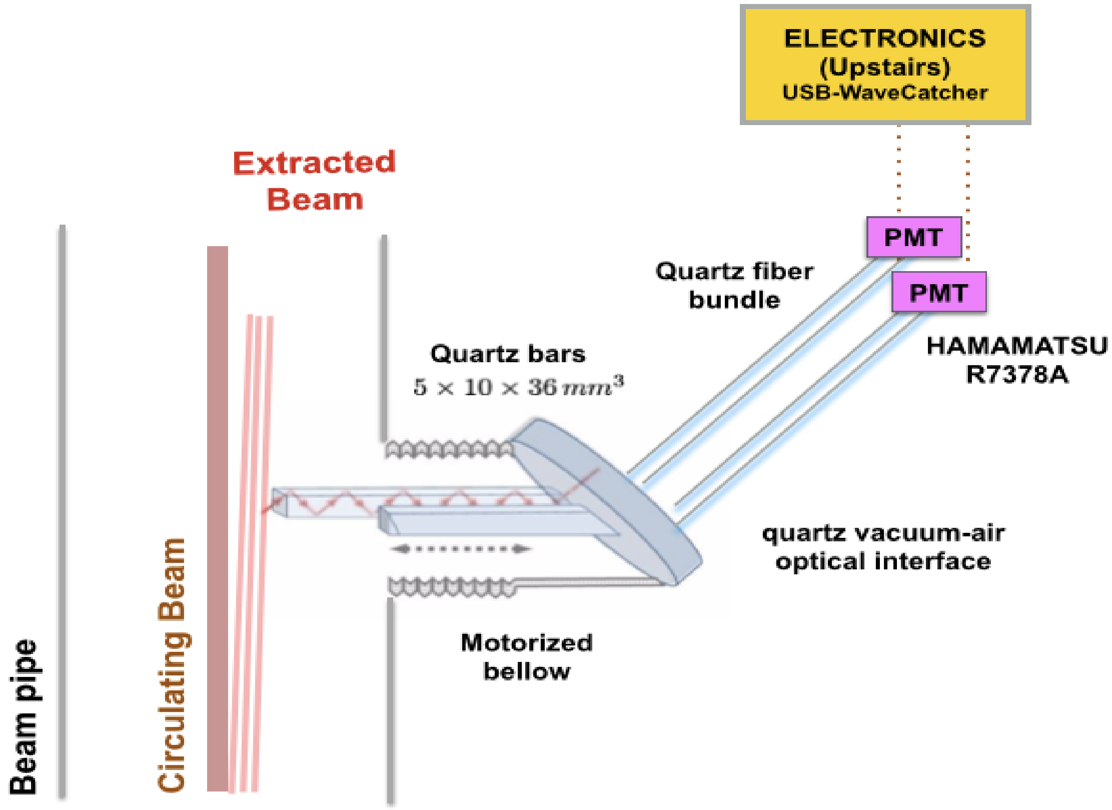

Figure: 5. 13 Conceptual draft of the CpFM in its final layout.

The bar are supposed to be identical and sized 5 x10 x 360mm^3, being 5mm the Quartz thickness crossed by the particles of the channeled beam (supposed parallel to the pipe and therefore perpendicular to the bars). The rear edges of the bars are mechanically coupled to a standard 3mm Quartz viewport which realizes the vacuum-air interface and it is connected to a stainless steel flange. It is not possible to improve the coupling between bars and viewport using optical grease because it would darken in the SPS radiation. The viewport, in turn, is mechanically coupled to the fiber bundles, one for each CpFM bar. The bundles are made by 100 Fused Silica fibers 4m long which transmit the light on the floor, 1m from the pipe, where the PMTs are located. In fact, as the fibers are very brittle and cannot bend at a radius lesser than 400 mm, 4m long fibers are required to connect the viewport to the PMTs. Moreover as the SPS tunnel is always lit, the bundles are sheltered from background light by stainless steel coating. Finally the PMTs, one for each CpFM channels, are enclosed in a light-tight metallic box that shields them both from the electromagnetic noise and from the background light.

5.4.2. Mechanical integration

Figure: 5.14 show the mechanical integration of the CpFM into the beam pipe of the SPS. The CpFM is hosted by a general purpose tank with large flanges, already used in the SPS for several devices. The Quartz bars are integrated into the tank through a special holder that is connected to the flange and touches the bars just with two 0.5mm thick shoulders, to minimize the light loss at the interface between metal and Quartz. The bars are put into the beam pipe by a motorization system designed to be adapted to this standard tank. It consists in a radiation-hard stepper motor moving a slide attached to the flange. In turn, the flange and therefore the bars, are connected to a compressible bellow. By closing and opening the bellow the bars are inserted or retracted from the beam pipe. When the bellow is completely extended, the CpFM 1 is 5mm further than the center of the beam pipe, while when it is completely closed the tip of the CpFM 1 is at 65mm from the beam pipe center.

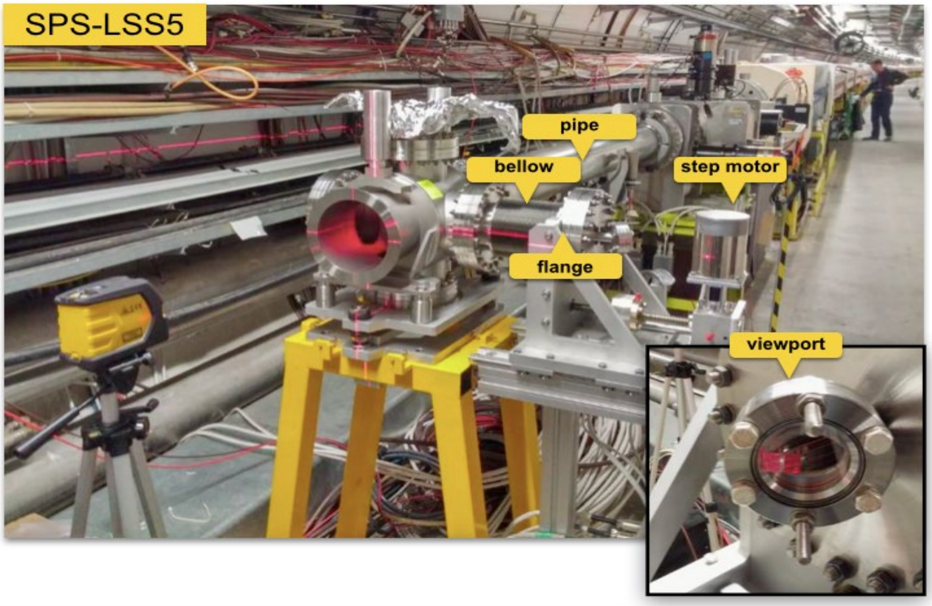

Figure: 5. 14 CpFM tank during the alignment procedures.

5.4.3. Readout system

As it has been explained in Section 5.3, the readout of the two CpFM channels is realized by the Wave Catcher board, located in a shielded area of the tunnel, 40m away from the detector position. The PMTs signals are transported up to the electronics through low attenuation coaxial cables (CKB50). The signal attenuation produced by 40m of this type of cable has been measured to be 10%. The Wave Catcher board is read out by the usual UA9 experiment trigger. This signal is the SPS revolution signal (43 kHz) downscaled by a factor 1000 and synchronized with the passage of a filled bunch in LSS5. CpFM 1, CpFM 2 and the UA9 trigger are acquired simultaneously in 3 different channels of the Wave Catcher with a frequency of 43 kHz.

The Data Acquisition (DAQ) system is integrated in the UA9 DAQ. In this way all the CpFM events have the same timestamp of the other devices and detectors of the UA9 experiment. In a standard UA9 run, for each trigger event two different files are saved: the rates file and the measurements file. The rate file includes the hit rate monitor output (counts/s) per each acquired channel. The Measurements file includes the output of the measurement block per each acquired channel. Moreover, a waveform file can be acquired usually with a lower frequency (1/1000, 1/100 triggers). It includes the digitized 1024 samples waveforms from each channel. The time length of the waveforms depends on the sampling frequency and it ranges from 320 ns (3.2 GHz sampling frequency) up to 2.4 ns (400 MHz sampling frequency). Using the measurements and the rate files and the common timestamp very useful plots are produced on-line, as the CpFM rates as a function of its position inside the beam pipe (Figure: 5.15, left) or the CpFM rates as a function of the angular position of the crystal (Figure: 5.15, right).

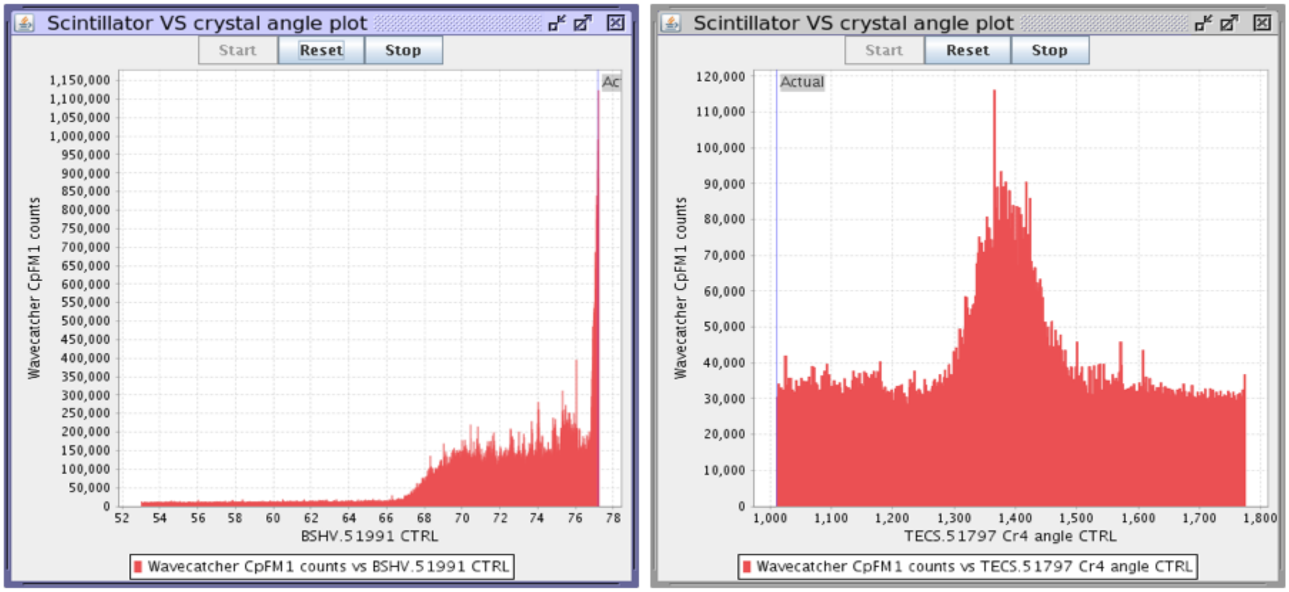

Figure: 5. 15 CpFM on-line plots examples. CpFM Linear scan: CpFM rates as a function of the CpFM position inside the pipe (left). Angular scan: CpFM rates as a function of the angular position of the Crystal. The peak in the rates corresponds to the channeling orientation of the Crystal.[50]

5.5. CpFM calibration test

Unfortunately the whole CpFM detector chain, with all the original components, has never been tested in beam before the installation. Nevertheless two calibration tests with a CpFM prototype have been performed at BTF with 450 eV electrons and in the H8 extraction line of the SPS with a 400 GeV proton beam. In Figure: 5.16 some pictures of the H8 beam test are shown. The CpFM prototype tested were not enclosed in the tank described in the previous section.

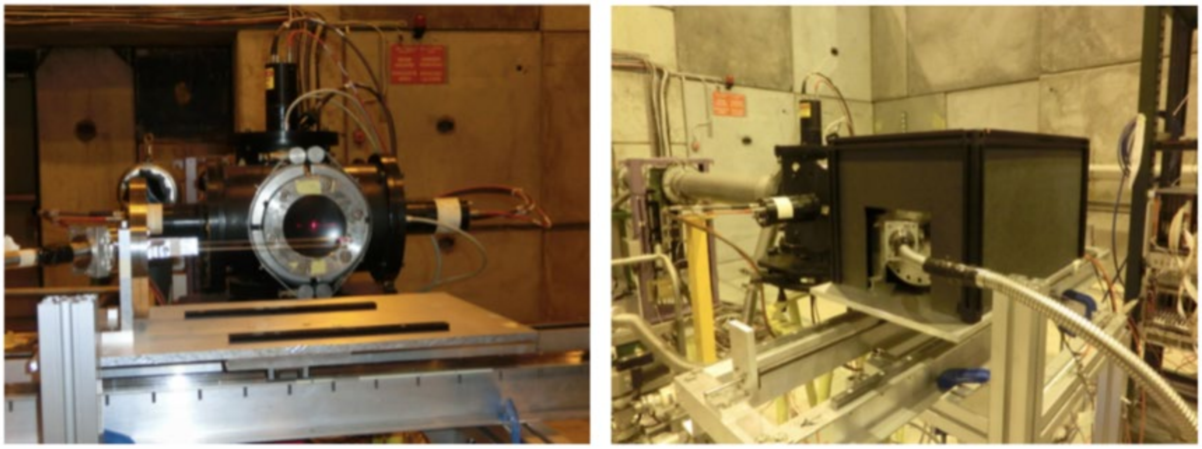

Figure: 5. 16 H8 calibration test. I-bar aligned with respect to the beam (left). Test layout: enclosed in the light-tight box there are the CpFM prototype and trigger counters to perform the efficiency and calibration measurements (right). [54]

The holder was made to support a single bar and the viewport was simulated by a 3.85mm glass plate. The bars, tested one by one, were two I-bars by the same company that realized the final one, but not exactly the same that in the end were mounted in SPS. The bundles were the two bundles of 100 fibers each used later for the CpFM as well as the two PMTs.

The outcomes of the two tests showed the linearity of the detector chain and the calibration factor in perfect agreement. In Figure: 5.17 the photoelectron yield per incoming electron related to the BTF test is shown. The plot is obtained from the signal amplitude divided by the amplitude of a single photoelectron (at the same bias of the working bias) and normalized to the number of incoming electrons counted by the downstream BTF calorimeter. The photoelectron yield per electron (or for other particle with charge 1 and $\beta \approx 1$) is 0.62. From the same plot we can evaluate the resolution of the detector for 100 incoming electrons (protons) as:

$$R = \sqrt{2}\,\frac{\sigma}{Mean} = 15\% \tag{5.2}$$

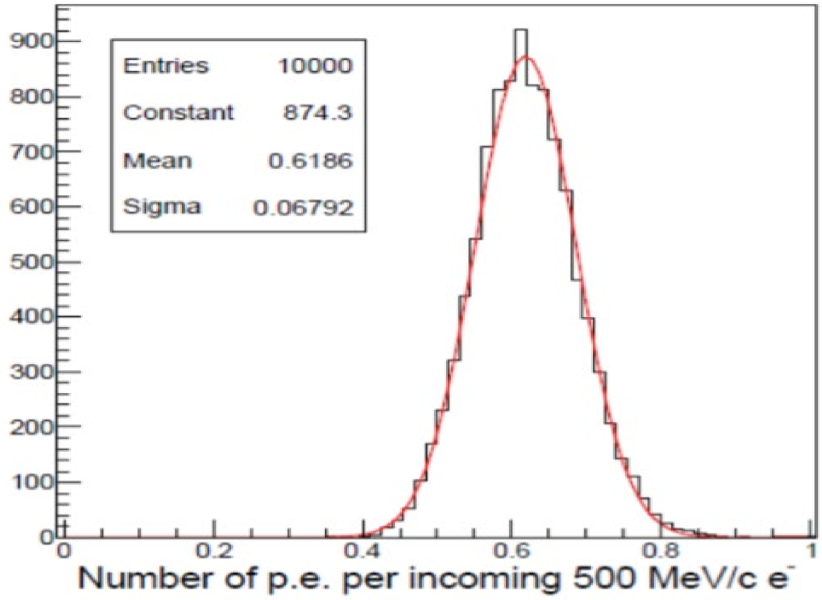

Figure: 5. 17 Distribution of the number of photoelectrons normalized for the number of the incoming electrons: photoelectron yield per electron. [54]

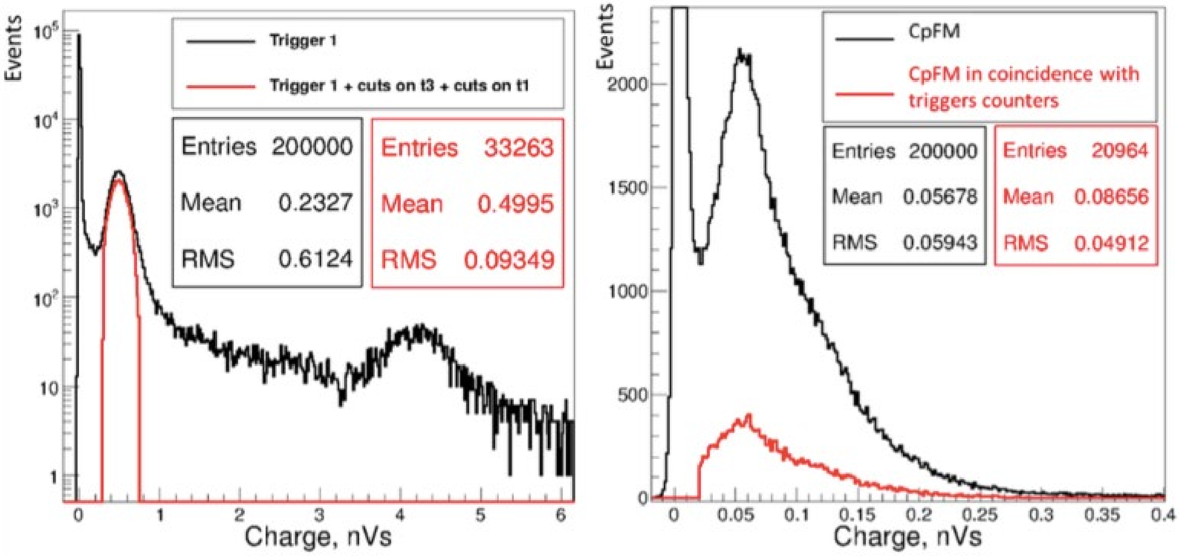

Figure: 5. 18 (a) charge distribution of the counter (trigger 1) placed in front of the Quartz bar end (where the protons cross the radiator). (b) Charge distribution of the CpFM. The black histograms correspond to all the events recorded, the red histograms are the result of the different cuts (coincidence with the counters placed upstream and downstream of the Quartz bar).[54]

Chapter 6

Alpha & Gamma Irradiation Effects on ZnO Photo Sensitivity

6.1. Introduction

Due to the mellowness of its manufacture technology, silicon dominates the commercial market presently in data storage and communication, integrated circuits for computing, discrete and power switching devices. For optoelectronic and high-speed instruments such as laser diodes and high-speed integrated circuits, Gallium arsenide (GaAs) is the material of preference. It shows superior electron transport properties and extraordinary optical properties. GaAs is a direct bandgap semiconductor, while Si is indirect, for this reason GaAs is better suited for optoelectronic devices. On the other hand, physical properties essential for high power, high temperature electronics and UV/blue light emitter applications are away from the limits of Si and GaAs. It is necessary to find substitute materials to achieve these devices with required properties. Wide bandgap semiconductors show signs of intrinsic properties such as wider bandgap, high electron mobility and higher breakdown field strength. For that reason, they are appropriate for high power, high temperature electronic devices and short wavelength optoelectronics. Zinc oxide (ZnO) is a direct, wide bandgap semiconductor material with various promising properties for blue/UV optoelectronics, transparent electronics, spintronic devices, and sensor applications.

In last decade, ZnO thin films have been inspected broadly due to their possible applications in optoelectronic and piezoelectric devices. It is one of the II-VI compound n-type direct bandgap semiconductor that own several great characteristics including a wide energy bandgap (3.3 eV) [58] , Photo absorption in UV range and high exciton binding energy of 60 eV[59]. ZnO has three kinds of crystal structures, i.e 1) wurtzite shown in Figure: 6.1, (2) zinc blende, and (3) rock salt, where at ambient pressure and temperature the most stable phase is wurtzite thermodynamically. Wurtzite ZnO has a hexagonal structure with the lattice parameters of a = 0.3296 and c = 0.520 65 nm[60]. In the ZnO wurtzite structure, the Zn and O atoms are set in an hcp pattern and are heap alternately along the c-axis, where each Zn atom is surrounded by four O atoms and vice versa, making a tetrahedral non-central symmetric arrangement. Hereby, wurtzite ZnO shows piezoelectric and pyroelectric properties, which are additional features that improve the photoconductivity of ZnO-based UV PDs [61].

The ZnO thin film can be prepared using a variety of methods such as sputtering, spray pyrolysis, sol-gel spin coating, chemical vapor deposition (CVD) and pulsed laser deposition (PLD), [62-64]. In spite of studies regarding to the solgel method, the sol–gel technique not only enables simple fabrication of a large area thin film at a low cost, but also simply controls over the film composition and consistency of thickness to scrutinize structure and optical properties of ZnO thin films and above all is environment friendly.

The main objective of this chapter is to test the ability/sensitivity of Zinc Oxide under alpha and Gamma radiations of low energy and to check whether ZnO is able to work under high radiations environment or not. Presently, there are different types of material including Silicon, Gallium Arsenide (GaAs) and Gallium Indium Phosphide (GaInP) etc are used as photon sensors that are radiation hard upto a certain threshold. The manufacturing/synthesizing process, cost and increasing dark count rate with radiations left space to be filled by suitable candidate for the same purpose.

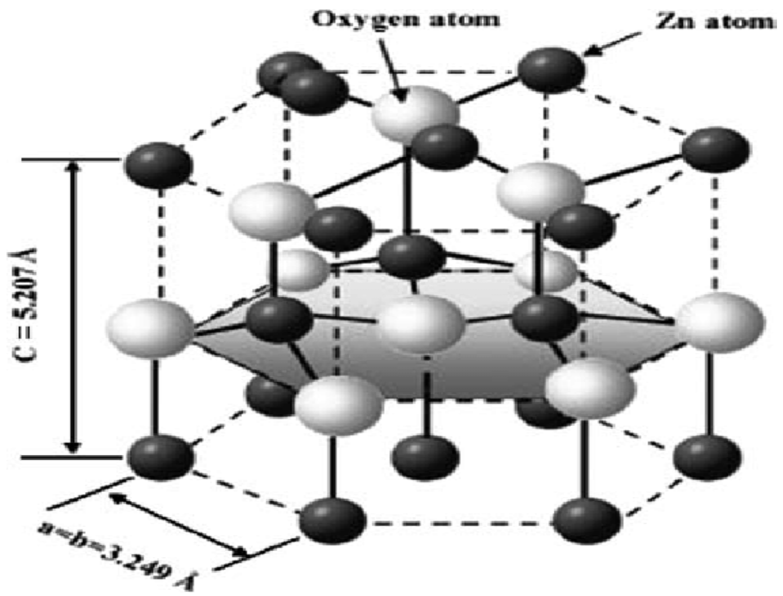

Figure: 6. 1 The hexagonal wurtzite structure model of ZnO and the tetrahedral coordination of Zn-O.

6.1.1. Photoconduction mechanism of ZnO UV Photo Detector

There are optoelectronic devices that change an optical signal into current. This conversion procedure can proceed into three main steps:

1. The incident light on the semiconductor produces the carriers.
2. The carriers are transported through the semiconductor to the electrodes. Typically, some kind of amplification is also there, esp. for Photodetectors.
3. Withdrawal of the generated carriers as current in the exterior circuit.

For photoconduction in a ZnO UV Photodiode, the photo generated electrons and holes under exposure to UV illumination get separated by an outside (conventional PD) or inner (self-powered PD) driving force. The power of the driving force plays a significant role in the e^- –h+ pair splitting and recombination practice, which determines the general photo response performance of a PD.

The photoresponse method of ZnO-based UV PDs is characteristically different from those of conventional semiconducting materials, where oxygen molecule adsorption and desorption play a critical role in photoconduction. In the dark, oxygen molecules adsorb on the ZnO face from ambient according to the equation: O_2 (gas) + e^-(surface) → O_2^-(adsorption), and then form a low conductivity depletion region. During UV illumination, e^- –h+ pairs are photo generated, where few of the photogenerated holes desorbs the adsorbed oxygen molecules from the ZnO surface to reduce the low conductivity depletion width as follows, $h^+ + O_2^-$ (adsorption)→O_2 (gas). In conclusion, the unpaired photogenerated free electrons collectively with available holes contribute to photoconduction in the existence of an external driving force[65, 66].

Figure: 6. 2 shows the photoconduction method of a ZnO NW-based UV Photodiode (Figure: 6.2a) under the ultraviolet light [67]. As given in Figure: 6.2b (bottom diagram), when oxygen molecules get adsorb on the ZnO surface, bending occurs in upward energy band because of the formation of a little conductivity depletion layer in the dark (top schematic). On exposure to UV light, the photo created holes travel to the surface of the nanowire along the potential slope initiating from energy band bending for the desorption of adsorbed oxygen molecules, resulting in a decrease in the low conductivity depletion size. Figure: 6.2c illustrates the migration of the photo generated holes (bottom schematic) for oxygen desorption and decrease in upward energy band bending (top schematic) upon exposure to UV illumination. Again, the oxygen molecules are re-adsorbed when the UV light is turned off and vice versa.

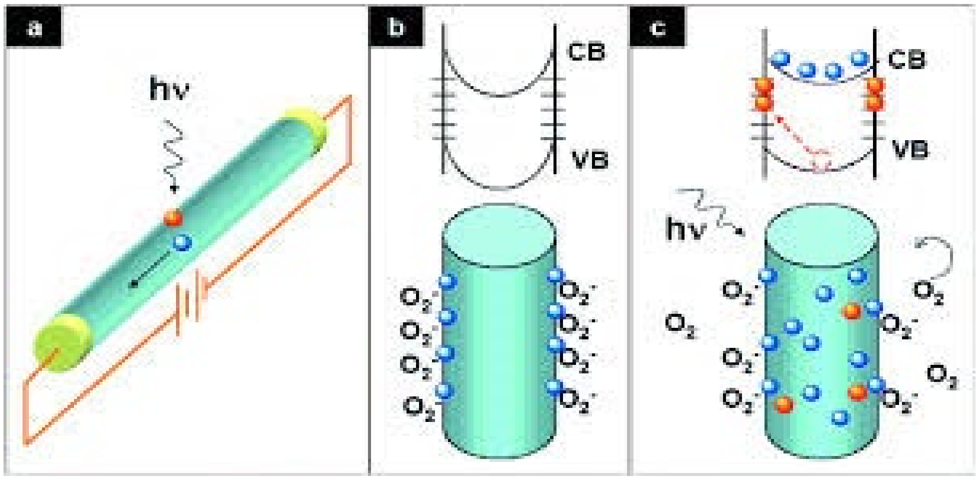

Figure: 6. 2 Photo conduction schematic in ZnO[61]

6.2. Experimental Work

6.2.1. Substrate preparation and electrode deposition

Initially, the silicon (Si) wafer, crystal orientation (111) and thickness of 3 µm, washed in dilute solutions of Dilute hydrofluoric acid/DI water, Sulfuric acid/hydrogen peroxide/DI water, ammonium hydroxide/hydrogen peroxide/DI water to remove silicon native oxide, adhering particles and organic/inorganic impurities from its surface. Next, a polyethylene terephthalate (PET) sheet with a specific patterning configuration that defines the features to be patterned (mask) was applied to the cleaned Si substrate to create the interdigitated gold (Au) electrodes using sputtering. The sputtered chamber was kept at room temperature under an argon pressure of 0.3 mtorr, giving rise to a Cu deposition rate of 2 nm s^{-1} for 1 min to produce 120 nm thin Au electrodes.

6.2.2. ZnO synthesis

A sol-gel solution was prepared by dissolving zinc acetate dehydrate (219.51 mg) in 1-propanol solvent (100 ml) to form a 10 mM concentrate solution. The mixture was then solicited for 30 min and kept at room temperature for eight hours in an isolated environment for sol-gel stabilization.

6.2.3. Sensor fabrication

SiO_2/Si substrates with interdigitated Au electrodes were used to make the sensor devices. The obtained stabilize ZnO solution was drop cast on the Au/SiO_2/Si substrate and dried at 120 °C 30 min in an oven. The baked film's post-annealing was carried out at 350 °C in a convection furnace under a Nitrogen (N_2) environment to remove the organic residuals remaining in the crystals and improve adhesion of the film with Au electrodes. Schematic and real picture of the sensor are shown in Figure: 6.3 and Figure: 6.4 respectively:

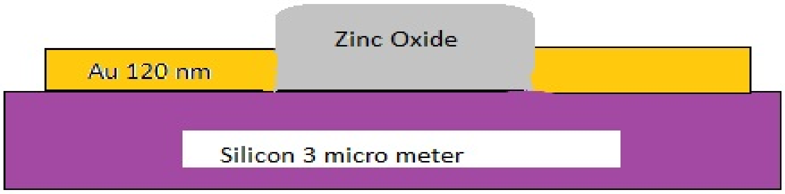

Figure: 6. 3 Schematic of the Sensor

Figure: 6. 4 Real Pictures of the sensor

6.2.4. SEM Analysis

The morphological study was done using a field emission scanning electron microscopy system (FESEM, JEOL-6700s). The surface morphology of fabricated ZnO thin films onto Si substrate using SEM was investigated. The SEM picture of ZnO films is shown in Figure: 6.5 which indicate that the deposited ZnO thin film on Si substrate has rough surface morphology and comparatively big particles which are fit connected to each other.

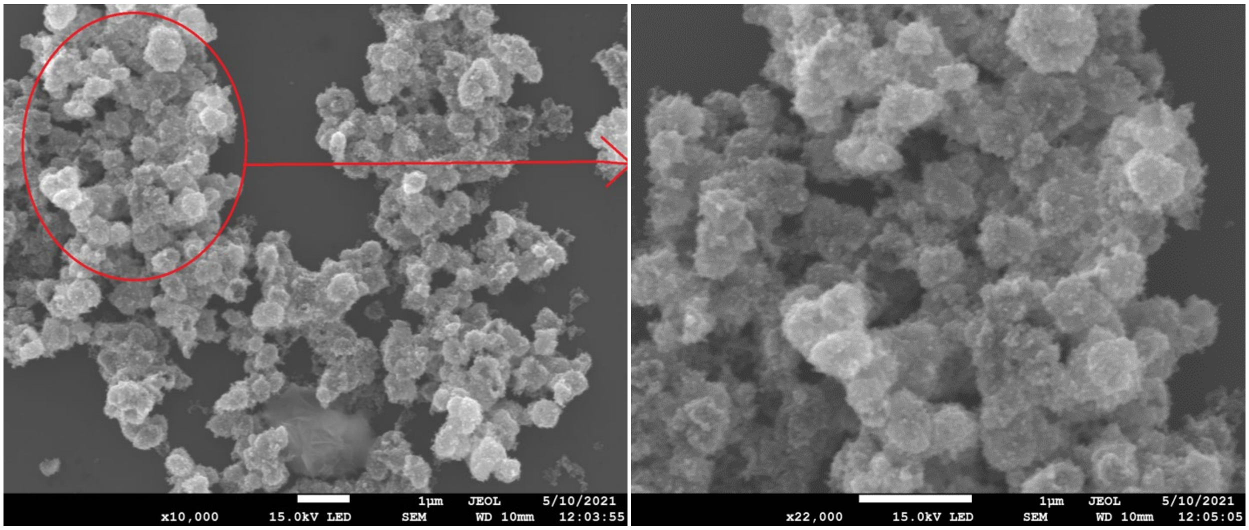

Figure: 6. 5 SEM picture of ZnO thin film

6.2.5. UV–visible absorption spectroscopy

The UV–visible characterization of the grown films gives information about the properties such as band gap energy, optical active defects and band structure etc. Optical properties of ZnO have been studied by UV–visible spectroscopy in absorption mode which is shown in Figure: 6.6. I have taken the absorbance spectrum of ZnO using V-750 UV-visible Spectrophotometer equipped with diffuse reflectance spectra.

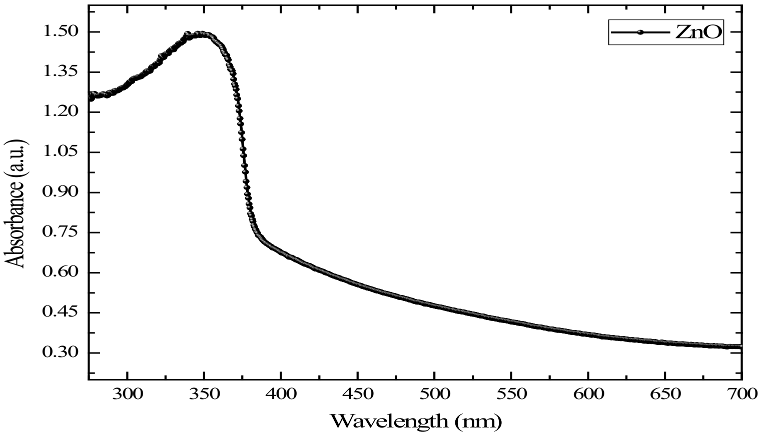

Figure: 6. 6 UV–visible absorption spectra of the ZnO thin films on quartz substrates

A photon of hν energy incidence on semiconducting material stimulates a direct transition between the highest occupied state of valance band and the lowest unoccupied state of the conduction band. This fact can be utilized to estimate the optical band gap energy E_g of the material using the Tauc's equation:

$$Ah\nu = A(h\nu - E_g)^n \qquad (6.1)$$

In equation 6.1 "α" is the absorption coefficient, 'n' has different value for different kinds of transitions. It is given as 1/2 for the permitted direct transition and 2 for the allowed indirect transition. But, n acquires the values of 3/2 and 3 for the direct and indirect forbidden transitions correspondingly. "A" is the temperature independent constant and corresponds to the band tailing. In order to determine E_g value, a plot with $(\alpha h\nu)^2$ along y-axis and hν along x-axis is drawn. Extrapolation of the linear portion of Tauc's plot from $(\alpha h\nu)^2 = \infty$ to zero provides an intersection with the x-axis which is associated to the E_g value of the material. Tauc's plot is shown in Figure: 6.7. These outputs are in good relation with the ones in literature [58].

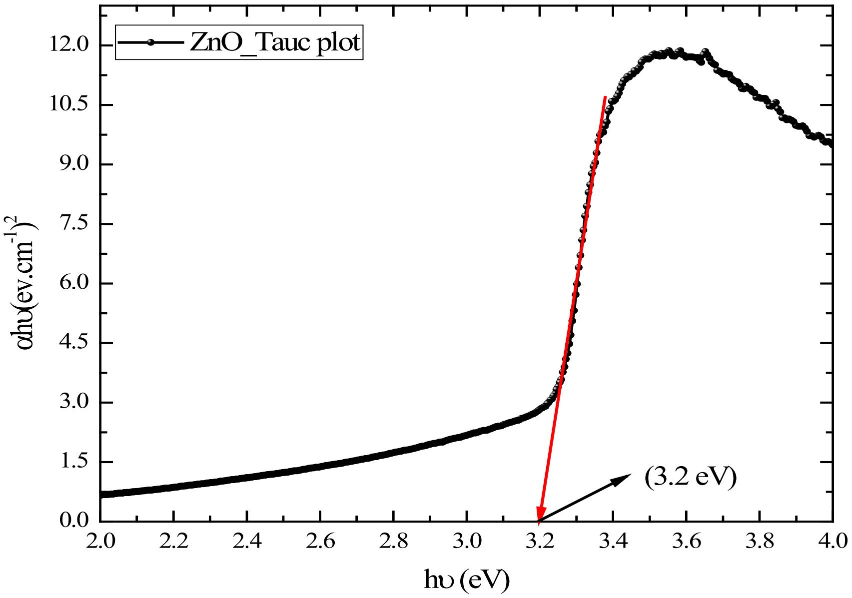

Figure: 6. 7 Tauc's plot of ZnO

To support the performance of photo carriers at various excitation wavelengths we have examined the PL spectrum of the film at room temperature (Figure: 6.8). The figure shows mainly two emission bands: The band in the UV region corresponds to near band-edge emission and the other in the visible region is due to the structural defects and impurities in ZnO film.

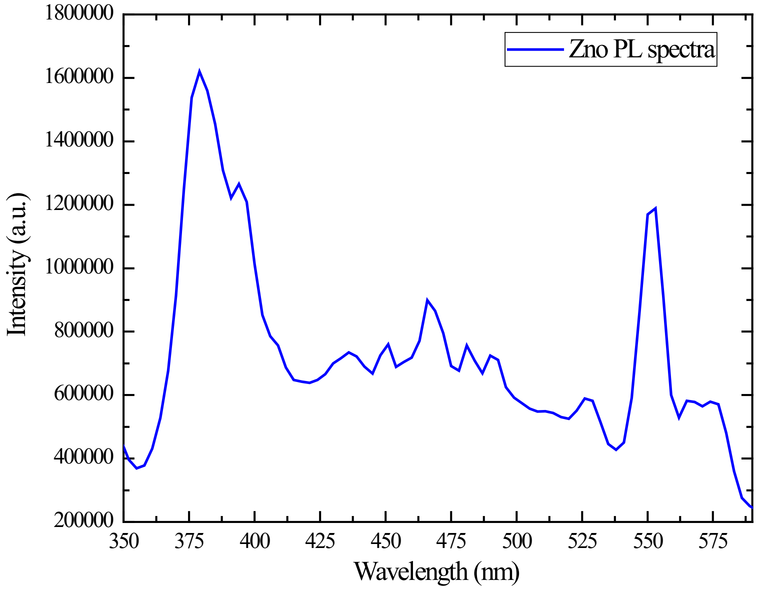

Figure: 6. 8 Photoluminescence spectrum of ZnO film (Room temperature)

6.3. Photodetector performance measurement

A home-made sensing test system shown in Figure: 6.9 containing a resistance measurement facility was used to examine ZnO-based sensors' sensing performance. The fabricated sensor device was placed in a dark box with a volume of 7000 cm^3 and alternately linked with the signal acquisition system by a slender Ag wire. Sensing test was operated at room temperature with dry condition. The electrical conductance signals of the sensor were collected and recorded by Keithley Digital Multimeter (2000) with help of GPIB-USB-HS (National Instrument) and Labview. UV Lamp of 254 nm and 365 nm spectrum lamp is used for light conditioning. The following formula calculated the response sensitivity, S, of the sensor.

$$S(\%) = \Delta R/R_0 \times 100 = [(R_g - R_0)/R_0] \times 100 \tag{6.2}$$

e R_0 and R_g represent the sensors' resistance upon exposure to dark (no light) and light, respectively. The response and recovery time were described as the time required for the signal to reach 90% of the equilibrium value of sensitivity during the ON and OFF, respectively. The photo detection switching speed is an important quality of PD, which determines how quickly it returns to its original state after switching off UV or how fast it response to the exposure to UV.

A quick response to the UV PD (smaller values of response time and recovery time) is very important.

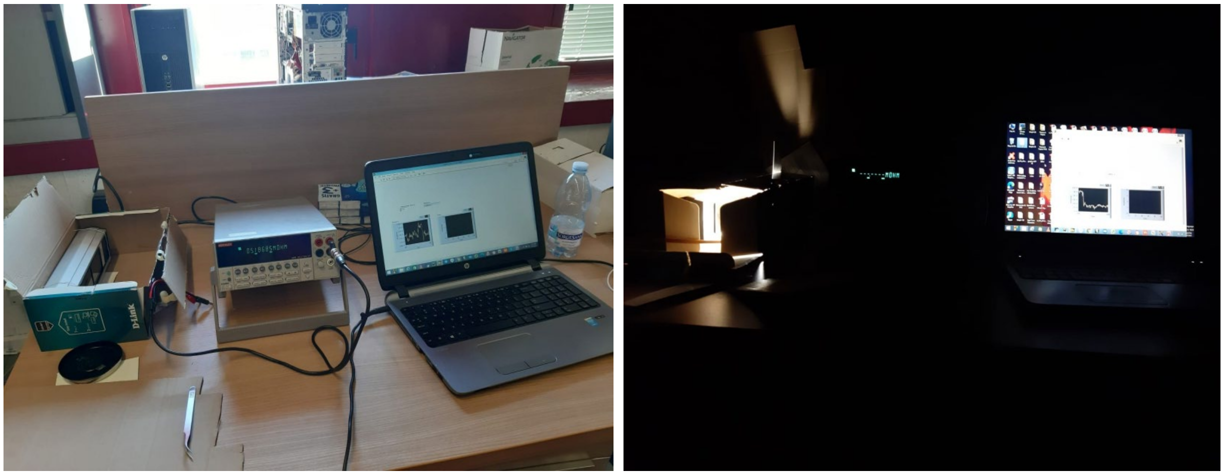

Figure: 6. 9 Photo Response Testing System

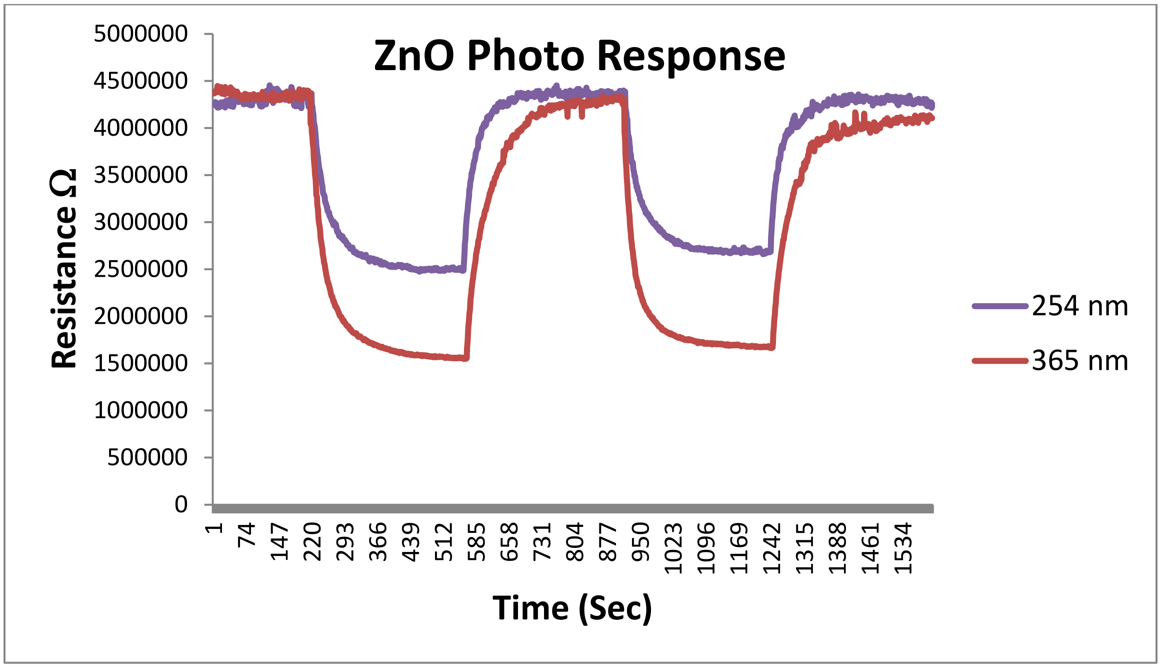

Figure: 6. 10 Photo response of ZnO based sensor under different wavelength.

In Figure: 6.10 response of ZnO based sensor to different wavelengths is shown. It confirms that this sensor has good potential for optoelectronics applications. For the confirmation of its radiation hardness, in this work we performed some gamma and alpha particle radiation tests which are presented in the following.

6.3.1. Gamma Radiation effects on Performance

The effect of gamma irradiation on the structural and optical properties is discussed in detail in [68] where it is shown that the structure of the film had not witnessed any important change in term of grain size or preferred orientation. We therefore performed tests to check the effect of gamma rays on sensitivity of the sensor before, during and after radiations. For the test we used Cobalt 57 (Co-57) (shown in Figure: 6.11) as Gamma source for 3 hours continuously. The activity A_t was measured by the following equation.

$$A_t = A_0 e^{-\lambda t} \tag{6.3}$$

where A_t is the activity on sensor computed from equation 6.3, A_0 is the initial activity, λ is decay constant, A_t was about 5.19 x 10^{-13} Bq. which is approximately 7.32 x 10^{-22} Gy for 6 hours.

Figure: 6. 11 (a) Co-57 Gamma Source (b) fixed on sample/sensor

The results show that the response time and sensitivity of the sensor before and after the gamma irradiation remained unaltered, which confirms that gamma radiation has no major effect to damage the sensor. The results are given in Figure: 6.12.

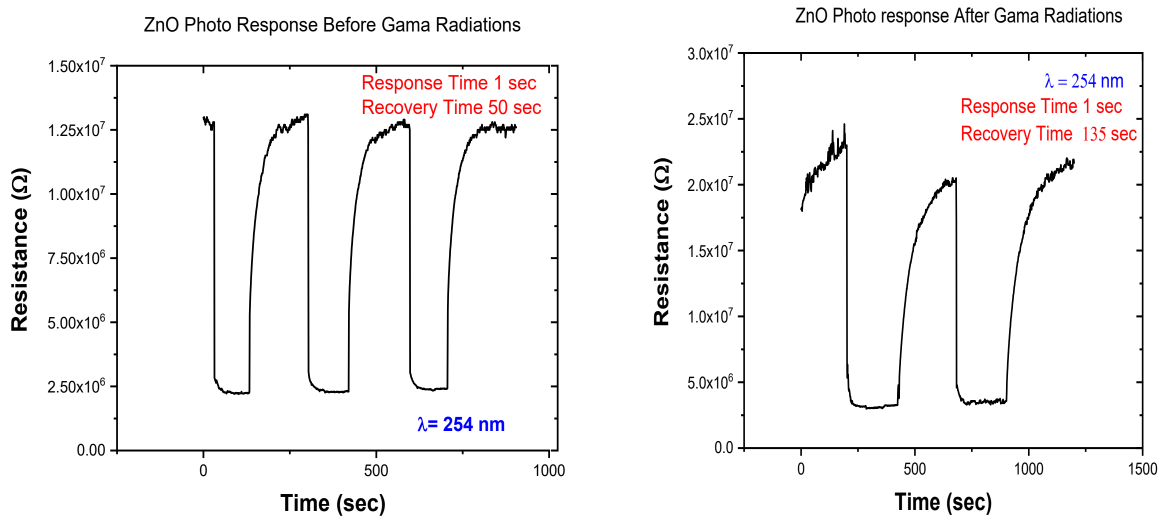

Figure: 6. 12 Response and recovery times of sensor before and after gamma irradiation

From Figure: 6.12 it is concluded that the response time of the sensor remains 1 s before and after irradiation, whereas its recovery time increased from 50 s to 135 s (explained in conclusion). The sensitivity given in Figure: 6.13, remained 81.90 % before and after irradiations see Table: 6.2.

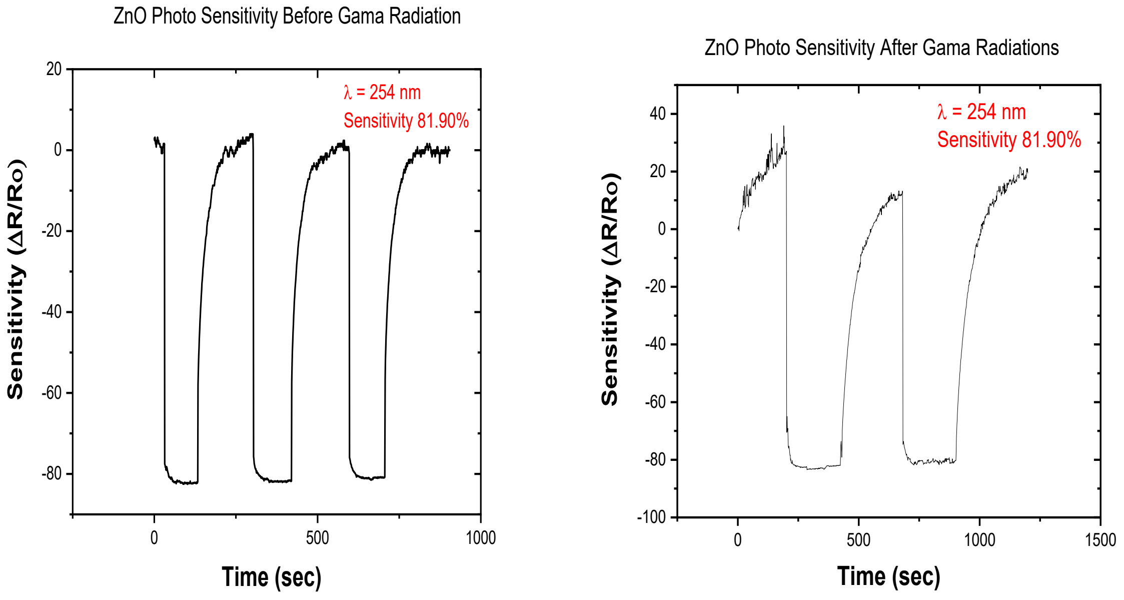

Figure: 6. 13 Sensitivity of the sensor before (left) and after (right) gamma irradiation.

Table: 6. 1 Detail of Gamma Radiations

Source	**Source Energy**	**Activity (Bq)**	**Time (hrs)**	**Dose Rate (Gy/hr)**	**Distance from sample (cm)**
Cobalt 57	1 M eV	5.19×10^{-13}	6	1.22×10^{-22}	0.8

Table: 6. 2 Gamma Rays (Co-57) Effect on ZnO based sensor

Characteristic	**Before Radiations**	**After Radiations**
Response Time	1 s	1 s
Recovery Time	50 s	135 s
Sensitivity (%)	81.90	81.90

The results in Table: 6.2 confirms no change in sensitivity and response time and the only change noticed in recovery time is most probably due to experimental setup and varying condition of measurement. Conclusively, we can say that gamma rays have no effect on the sensor performance.

6.3.2. Alpha Radiation effects on Performance

In order to check the alpha radiation hardness of the sensor (ZnO), Americium- 241 was used as source. The ZnO sample was irradiated by this source in various times and conditions. The photo response and photosensitivity were measured before, under and after irradiation. The detail of radiation and results of the measurements are given in Table: 6.3 and Table: 6.4 respectively. The activity A_t was computed using equation 6.3. The alpha source is shown in Figure: 6.14.

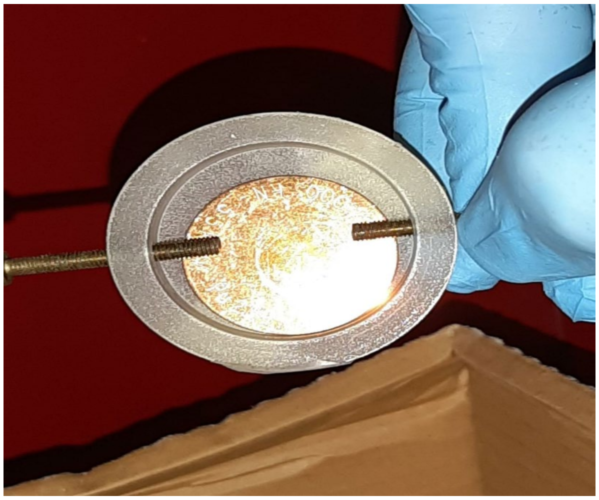

Figure: 6. 14 Americium-241 (alpha source)

In Figure: 6.15 and Figure: 6.16 the photo response and sensitivity before and after irradiation are shown, respectively.

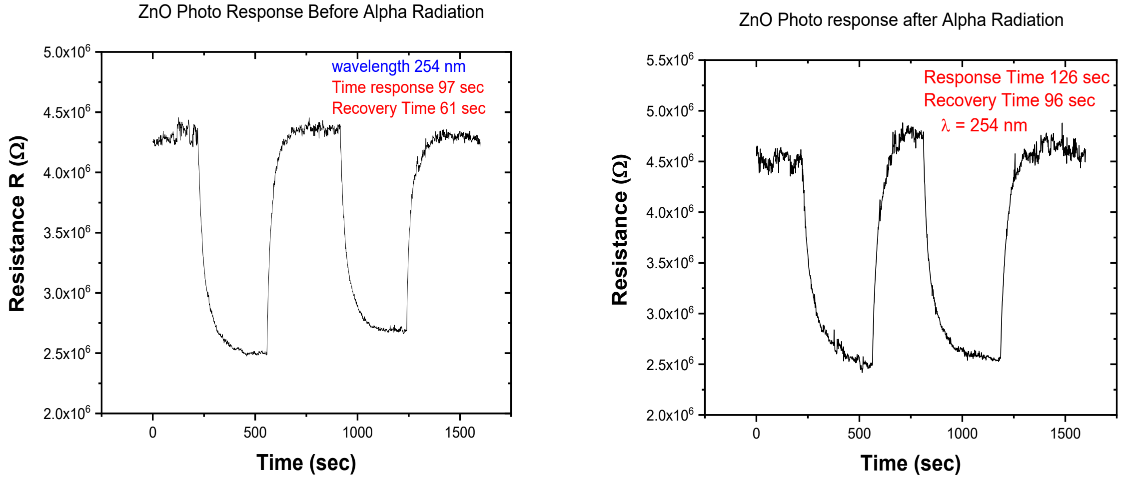

Figure: 6. 15 Response and recovery times of sensor before (left) and after (right) alpha irradiation.

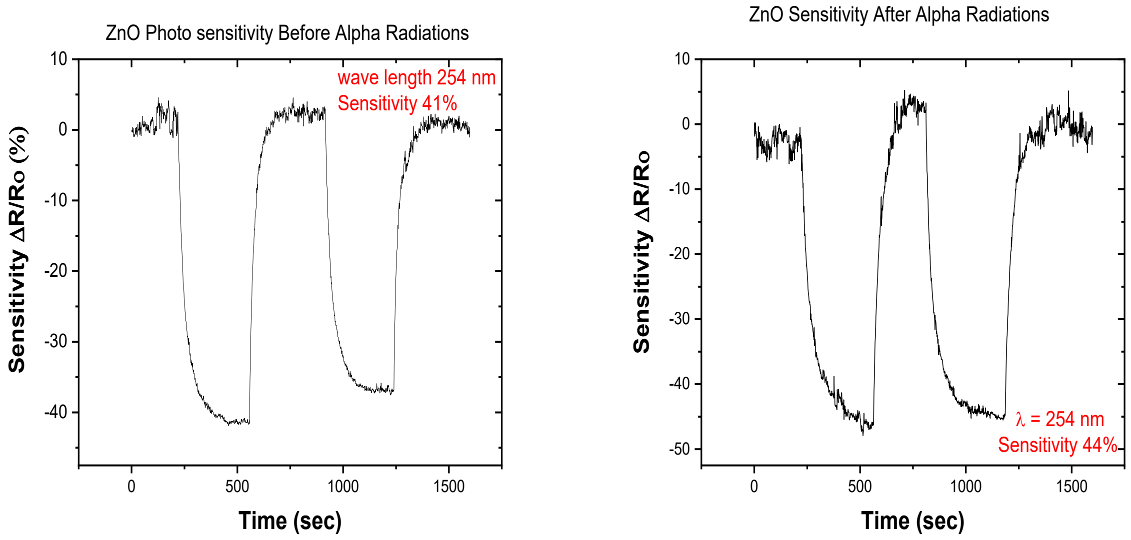

Figure: 6. 16 Sensitivity of the ZnO based Sensor before (left) and after (right) alpha irradiation.

Table: 6. 3 Details of Alpha Radiation

Source	Source Energy	Activity (Bq)	Time (hrs)	Dose Rate (Gy/hr)	Distance from sample (cm)	Energy[8] Loss (%)

---

[8] The Energy Loss is calculated using SRIM 2011

Americium 241	5M eV	2.85 x10^3	15	2.02 x 10^{-5}	0.7	99.95

Table: 6. 4 Alpha Particles (Am-241) irradiation effect on ZnO based sensor

Characteristic	Before Radiation	After Radiation
Response Time	97 s	126 s
Recovery Time	61 s	96 s
Sensitivity (%)	41	44

6.3.3. I-V Characteristics of ZnO

The current-voltage quality of a photodiode without incident light is same as a rectifying diode. There is an exponential rise in current when the photodiode is forward biased whereas with reverse bias a little reverse saturation current emerges. It is connected to dark current as given in equation:

$$I_D = I_{sat}\left(e^{\frac{qV_A}{k_BT}} - 1\right) \tag{6.4}$$

where I_D is the photodiode dark current, I_{SAT} is the reverse saturation current, q is the electron charge, V_A is the applied bias voltage, k_B=1.38 x 10^{-23} J / K; is the Boltzmann constant and T is the absolute temperature (273 K= 0 ºC).

This relationship is illustrated in Figure: 6.17 and 6.18, from equation 6.2, three different states can be defined: (a) V = 0, the dark current I_P=0; (b) V = +V, the current increases exponentially (this state is also known as forward bias mode); (c) V = -V, a reverse bias is applied to the photodiode, the dark current becomes the reverse saturation current, I_{Sat}. By illuminating a photodiode with optical radiation, the I-V curve shifts by the amount of photocurrent (I_P). Hence:

$$I_{Total} = I_{sat}\left(e^{\frac{qV_A}{k_BT}} - 1\right) - I_P \tag{6.5}$$

In principle a radiation hard optoelectronic sensor should have less change in Dark Current or dark counts before and after operating in high radiation environment, because many devices can be operated at high radiation exposure, but penalty is paid in high dark currents, which manifest themselves as fake signals. The dark current is comparatively small electrical current that runs in photosensitive devices, even when there is no photon entering the device. It consists of the charges created in the detector when no external radiation goes into the detector. In non-optical devices, it is referred to as a latch leakage current and is present in all diodes. In fact, dark current is due to the accidental generation of electrons and holes in the depletion region of the device.

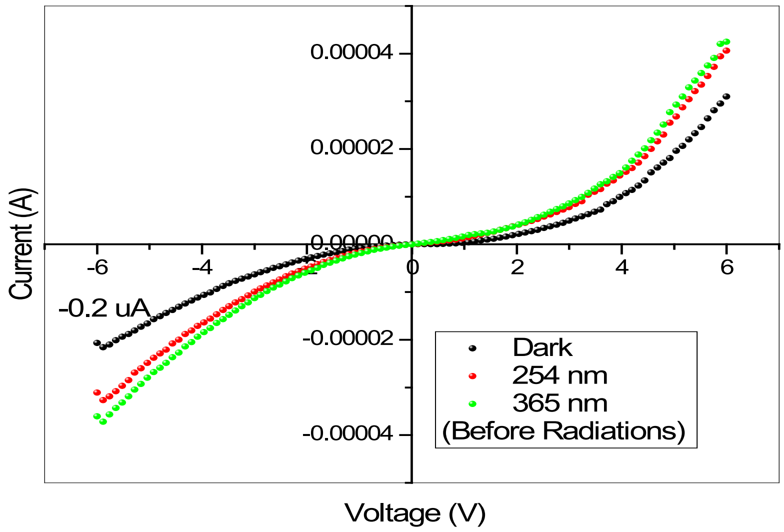

Figure: 6. 17 I-V Characteristics of ZnO before Radiations

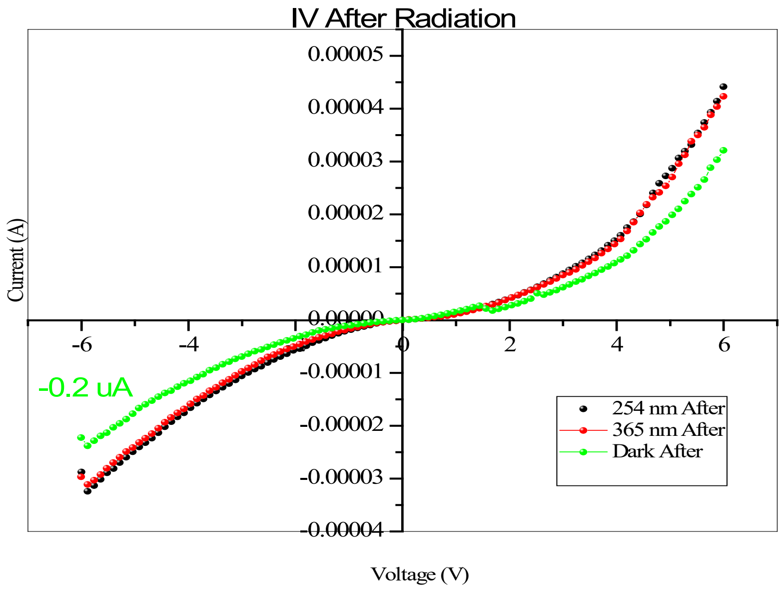

Figure: 6. 18 I-V Characteristics of ZnO after Radiations

From the aforementioned results shown in Figure: 6.17 and Figure: 6.18 it is clear that for low alpha radiations the ZnO sensor shows no significant change in dark current. To understand the concept of dark current better and its deal with external radiations, we should explain its root causes or origin.

6.3.3.1. Origins of Dark Current

Dark current of a Photodetector can have various origins. Here two main are discussed:

(i). Internal Photoelectric Effect

In photo-diodes and other photodetectors with some p-i–n or p-n junction dark current is regularly caused by thermal excitation (generation of carriers), not essentially directly from valence to conduction band, but most likely through defect states associated to crystal defects or impurities. Such thermal effect depends on the active area, temperature, operation voltage (mainly close to the breakdown voltage, where impact ionization can take place) and also on the band gap energy of the material. Tunneling throughout the depletion region can also contribute at high voltages. For detectors of visible light range such as silicon-based photodiodes, the dark current can be very little (e.g. in the picoampere region) (even for considerable bias voltages) and is then of no consequence for most applications. Germanium photodiodes demonstrate higher dark currents which are, though mostly not due to their somewhat lesser band energy. Indium gallium arsenide diodes, which also have a reduced bandgap energy compared with silicon, also show a comparatively low dark current.

In materials with significantly smaller band gap, dark current could be a serious problem and may thus require operation at considerably reduced temperatures. For operation close to the break-down voltage, the dark current can turn out to be far stronger than the value noted at lower voltages.

Dark currents may also be produced by some leakage currents which are not linked to thermal excitation.

Generally, dark current cannot occur for operation with zero bias voltage, because there is no energy provision available for it, at the uniform temperature of the device, without any Peltier effects. Thus, one can functionalize a photodiode, for example, with zero bias voltage in situations where effects of a dark current must be avoided.

Of course, output signals drifts may also take place in electronics, for example due to bias drifts of operational amplifiers. Therefore, a non-zero output signal does not necessarily indicate a dark current of the detector.

(ii). External Photoelectric Effect

The major cause for a dark current is typically *“thermionic emission”* on the photocathode. This means the thermal excitation of electrons. Thermionic emission can be considerable for cathode materials with very small work function, as necessary for infrared detection. It is also powerfully temperature-dependent; low-temperature operation is thus very effective in reducing the dark current. The dependence on the operation voltage is feeble. For pretty high operation voltages, there can be a steeper rise of dark current due to field emission at different locations in the bulb. That can lead to accelerated aging. Some current is added by the ionization of residual gas, i.e., due to the non-perfect vacuum. This is mainly the case for detectors that operate with higher voltages, for example photomultiplier.

In general, fairly weak contribution comes from the leakage current due to non-perfect electrical isolation.

It is also possible that some unwanted light is generated by scintillation, e.g. when electrons hit the glass tube. At a usually very low level, there are weak flashes of light caused by cosmic rays and radioactive substances e.g. in the glass tube or the near surroundings.

6.4. Conclusion and Future Work

It is concluded from the above measurements that ZnO Photo sensor has the ability to work under high radiation environment, as it hasn’t shown any major changes or damages to the Gamma (1 MeV) and alpha radiations of 5 MeV which loses almost 99.9 % energy inside the compound. The only change that can be noticed is the response and recovery times but it is not a big deal because it can be treated by making various shapes and thickness of this material. The response time is reduced by the reverse bias by increasing the size of the depletion layer. This increased width reduces the junction capacity and increases the drift velocity of the carriers in the photodiode. The transit time of the carriers is reduced, improving the response time. The response time and recovery time (photo detection speed) of conventional ZnO-based UV PDs varies from a few hundred seconds to milliseconds [61]. The rise and fall times for the photocurrent are measured as 22 ps and 8 ns also, show how the deposited ZnO thin film photodetectors (MSM etc) can be used for the applications needed for low light level (tens of ns pulses) detection and fast operation[69].

To use the ZnO material based sensors in radiation hard environment like inside SPS (Tens of KGy/Year and $10^{12}/cm^2$ neutron flux[54]) for Photon detection, it is mandatory to check its response under high energy particles (proton and neutron etc with Energy in GeV). This is our future task to check its performance under high energetic radiation particles for further use, in case it succeed to face those particles without any damages, it would be a great candidate for photo detection in radiations environment because of its low cost, easy fabrications method, fast photo detection, low light level detection and potential applications in the regime of pulse radiation detection (ZnO:Ga)[70] etc.

.

Chapter 7

Real Time Analysis of SiPM Signal

Main aim of this chapter is the characterization of SiPM and analysis of its recorded signal in Real time for the purpose to make a real time framework in the future for the purpose to monitor the proton beam in Cherenkov Detector (given in chapter 06) for UA9 experiment at CERN. Due to its radiation hardness, good photon detection efficiency (≈20%) in the wide spectral range and comparable gain (10^6) with other Photomultiplier like GaAs and GaInP based and others, SiPM has the potential to use it in radiation hard environment for low photon rate light detection in high energy physics detectors. In this chapter we reviewed the commercially available SiPM at the marketplace in terms of their fundamental properties and discussed how each characteristic influence or limit the design of classic HEP detectors.

7.1. Introduction

The Silicon Photomultiplier (SiPM) is a multi-pixel semiconductor photodiode, on which the pixels are jointed together on common silicon substrate[71]. In High Energy Physics, Multi-pixel silicon based diodes (SiPM) operating in Geiger mode, have gained a considerable attention in the last decade. Low cost, compactness and robustness, magnetic fields insensitivity [72] and higher photon detection efficiency make them an attractive competitor to conventional photomultiplier tubes (PMTs). As compared to avalanche photo-diodes (APD), SiPM offers a high intrinsic gain (10^5 -10^7) which considerably simplify the readout electronics and expands the response permanence to temperature or voltage changes. SiPMs are also insensitive to ionizing radiation, i.e. the nuclear counter effect as well. Furthermore, SiPMs give fast timing (~100 ps FWHM for a single photon) and single photon counting abilities. They work over the breakdown voltage (or in the Geiger mode) and offer a broad linear dynamic range with respect to the number of photons in a light pulse. At present, this kind of devices is also identified as Micropixel Avalanche Photo Diodes (MAPD) and Micro-Pixel Photon Counters (MPPC), depending on the maker.

7.1.1. SiPM Structure

SiPM is a pixilated detector where every pixel or a microcell is a series combination of an avalanche photodiode (APD) and a quenching resistor (R_Q). All of the microcells are joined in parallel; hence, a SiPM has two spikes, anode and cathode. The three sections in the Figure: 7.1

here demonstrate, from left to right, a cross section of three microcells in a feasible structural design, top view — the side of encroaching light —of the device, and an corresponding electrical circuit.

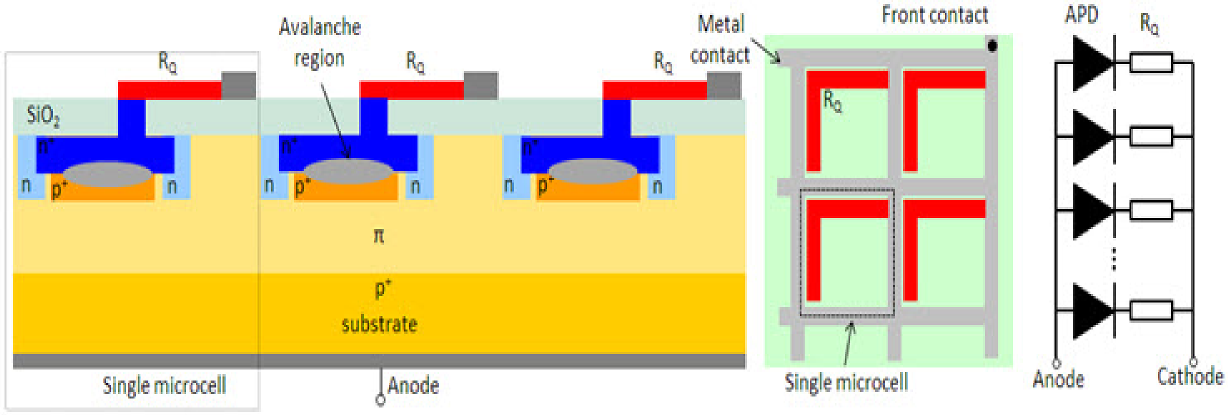

Figure: 7. 1 The figure depicts schematically archetypal structure of a SiPM. [From Hamamatsu]

In applicable SiPMs, the microcells of the same dimension are prearranged in a rectangular prototype. The dimension of a microcell lies in between 10 µm to 100 µm and the number of microcells per detector ranges from few hundreds to tens of thousands, depending on the device. Active areas of SiPMs range from 1 mm^2 to 6 mm^2 and spectral sensitivities from UV to IR, peaking in the visible (400 nm - 500 nm). As an example, Figure: 7.2 shows the microphotograph of SiPM with pixel size 42x42 µm^2, and a total pixel number m=576 on the area of 1 mm^2

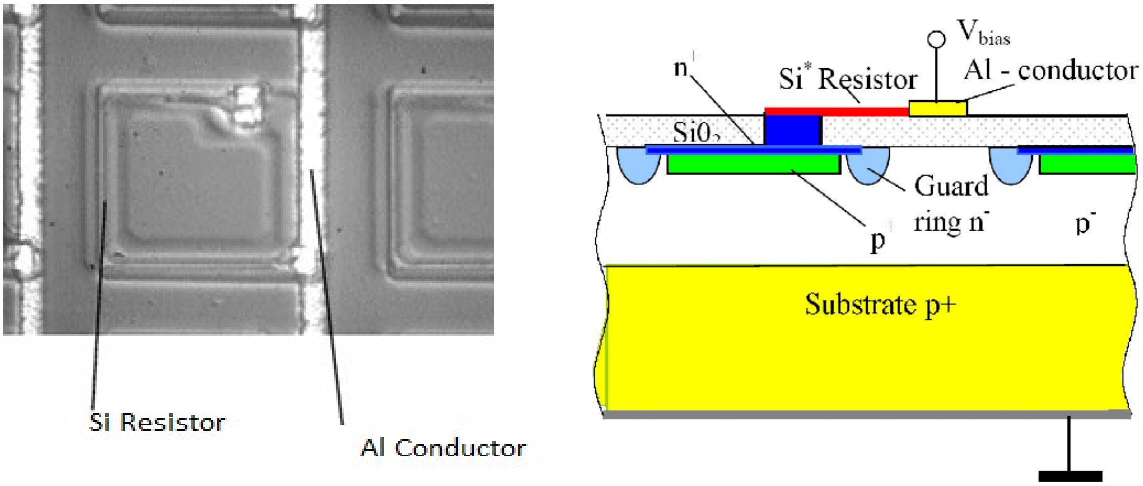

Figure: 7. 2 Silicon photomultiplier microphotograph (left) and Cross section through the topology of one SiPM cell (right). On the right side a part of a neighboring cell is shown. Photons are incident from the top [picture taken from [71]].

7.1.2. SiPM Working Mechanism

For the purpose to keep the voltage on each APD above than its breakdown voltage, SiPMs are externally biased each APD operating in Geiger mode. The key changeable parameter controlling device operation is overvoltage which is actually "the difference between the biasing voltage and the breakdown voltage ($V_{over} = V_{bias} - V_{op}$)". When a SiPM takes in a photon, the ensuing charge carrier (an electron or hole depending on the structure) can trigger an avalanche in the gain region (shown as the gray oval in the Figure: 7.1) within the p^{+} - n^{+} structure. The avalanche can generate 10^5 - 10^6 carriers which correspond to the gain of sensor. The function of the quenching resistor is to reinstate the APD back to the Geiger mode. The SiPM gain is linearly dependent on the values of overvoltage and junction capacitance. Although a SiPM is a pixilated sensor but it does not work as an image sensor. It is an analog device generating an output signal which is time-varying but could be measured in real time. The output signal is a time series of waveforms or current pulses, which have a discrete distribution of amplitudes: A, 2A, 3A, and so on. The amplitude histograms depend on the intensity and time-characteristics of the impinging light. Here is a closer glance into how a single microcell of a SiPM produces a waveform in reaction to light.

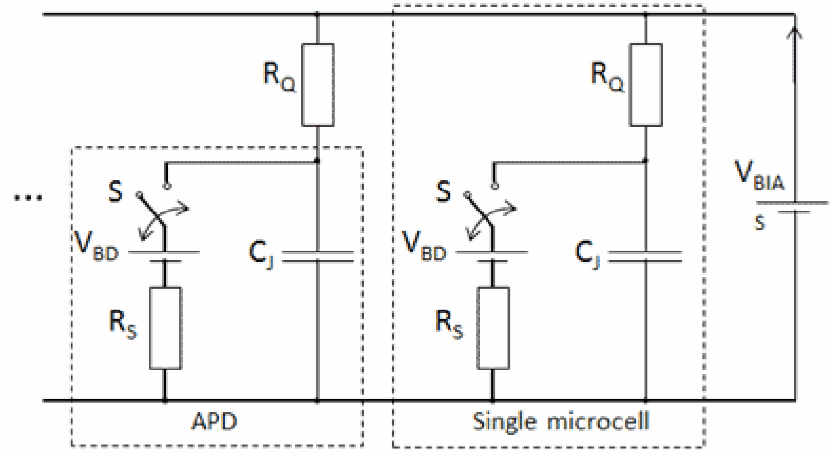

Figure: 7. 3 A simplify corresponding circuit of a SiPM (two representative microcells) biased by an external voltage source V_{BIAS}.

As mentioned above that microcell is a series combination of quenching resistor R_Q and an avalanche photodiode (APD). The microcells shown in Figure: 7.3 are all in parallel. The circuit modeling of the APD is a parallel combination of a capacitor C_J (denotes the junction capacitance) with a series combination of switch S, voltage source V_{BD} (equal to the breakdown voltage), and a resistor R_S (representing the resistance of the complete APD during a discharge). In the absence of light and ignoring dark counts, S is open and the voltage on C_J is V_{BIAS} ($V_{BIAS} > V_{BD}$), the microcell is in a light-sensitive condition and the APD is in Geiger mode. When the microcell takes in a photon, electron-hole pairs are generated, one of these charge carriers floats to the avalanche area, where it can start an avalanche effect. At the moment the avalanche starts, S get closed which causes C_J to be discharging during R_S ($R_S \ll R_Q$) with the time constant R_SC_J. The voltage on C_J reduces, lowering the chance of impact ionization. For most favorable R_Q, the probability ultimately becomes so little that the avalanche quenches. At this instant, S opens and V_{BIAS} recharges C_J with the time constant R_QC_J.

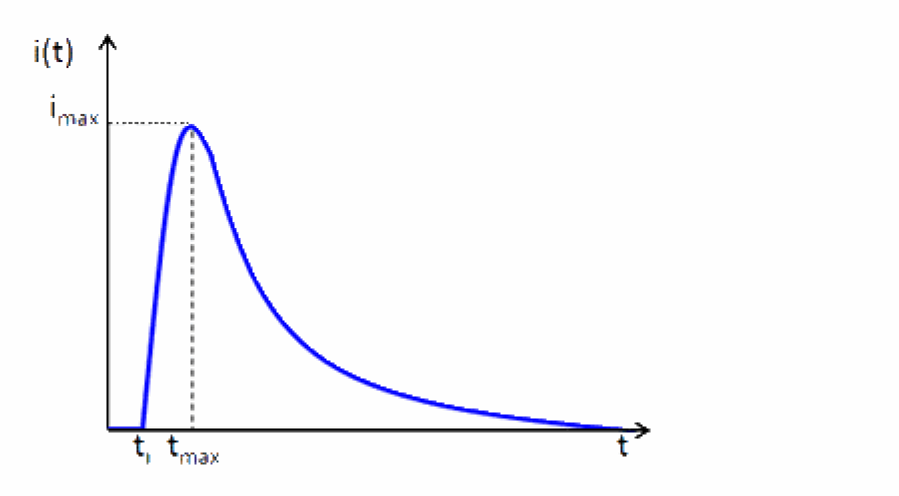

Figure: 7. 4 A diagram of the current flowing through the terminals of the SiPM through the above discussed process.

In Figure: 7.4, the avalanche starts at t_i and quenches at t_{max}. The pulse leading edge starts at t_i and raises proportional to $[\,1 - exp\left(-\frac{t}{R_sC_J}\right)]$. The pulse attains the maximum value $i_{max} \approx \frac{V_{BIAS}-V_{BD}}{R_Q+R_S} = \frac{\Delta V}{R_S+R_Q}$ at t_{max} and then declines as $exp\left(-\frac{t}{R_sC_J}\right)$. Integration of the current pulse with respect to time is equal to the total charge Q that has moved between the terminals of the SiPM. As a single charge carrier sources the transfer, being the gain $M = \frac{Q}{e}$ and $Q=C_J\triangle V$ therefore, $M = \frac{C_J\Delta V}{e}$. If two or extra microcells "fire" almost simultaneously in response to incident light, the output signal is a linear superposition of the pulses, each like the one illustrated in the figure, giving an amplitude 2A, 3A, so on. On the other hand, if the same pixel absorbs at the same time two or more photons, the output pulse is the same to that shown in the figure and the amplitude is A.

The time required for a pixel to turn into active again after a having discharged is called the pixel recovery time, "τ". This is taken as product of the pixel quenching resistor "R_q" and the pixel capacitance "C_j". The value of R_q has to be bigger than 100 kΩ such that to quench the avalanche and can be as large as 20 MΩ in several cases [73]. The value of Cj scales with the pixel area and can be 20-150 fF. Therefore, τ value ranges between a few 10 ns to a few µs. It is essential to note that polysilicon resistors are temperature dependent, and so is the pixel recovery time. Alternative quenching techniques are being experienced as well like integrated FET (field-effect transistor) circuits in the silicon wafer [74] or CMOS (Complementary Metal Oxide Semiconductor) quenching circuits in the case of digital SiPMs [75].

7.1.3. Gain of SiPM

The gain M is defined as the ratio of Q and the basic charge $e = 1.6 \times 10^{-19}$ C. Archetypal values of M are in the range of 10^5 - 10^7[76]. In particular:

$$M = \frac{Q}{e} = \frac{i_{max}}{e} = \frac{1}{e} \cdot \frac{(V_{BIAS} - V_{BR})}{(R_S + R_Q)} \cdot R_Q C_J \tag{7.1}$$

As R_Q>>R_S, we obtain:

$$M = \frac{C_J \Delta V}{e} \tag{7.2}$$

The equation 7.2 for the gain illustrates that it changes linearly with ΔV and C_J and somewhat surprisingly, it does not depend on R_Q. The value of C_J is set by the particular architecture of the SiPM; therefore, ΔV is the adaptable parameter that controls M. There is no apparent dependence of M on temperature; though, because V_{BR} does depend on temperature, so does M for a fixed V_{BIAS}. To ignore or remove the temperature reliance of the gain, the SiPM should be function so that ΔV remain constant.

An avalanche photodiode in a SiPM works in Geiger mode. If a charge transporter triggers a discharge in a microcell, the result is a current pulse with the total amount of charges Q moving through the SiPM terminals.

As shown in Figure: 7.5, current pulse starts at t_i and quickly increases until achieves the maximum value $i_{max} = (V_{BIAS} - V_{BR})/(R_Q + R_S)$ at t_{max}, which is about of ~1 ns. At t_{max}, the voltage on the APD falls to roughly V_{BR}, which is not sufficient to maintain the discharge, quenching happens. The junction capacitance C_J starts recharging, reasoning the voltage across R_Q to be decreasing and, thus, the current throughout the terminals of the SiPM to be also declining exponentially with the characteristic time $\tau = R_QC_J$. For typical values of R_Q and C_J, $\tau \approx 10$ ns[76].

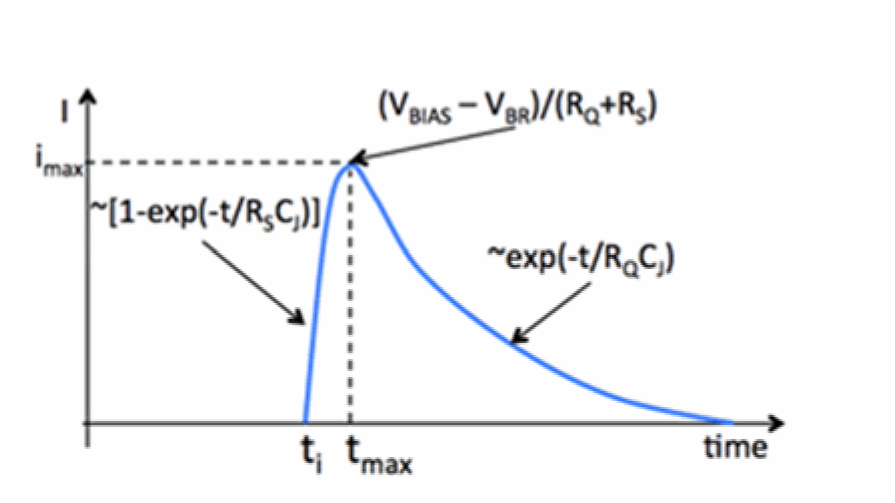

Figure: 7. 5 Current Pulse

7.1.4. Photon Detection Efficiency of a SiPM

The probability of a silicon photomultiplier (SiPM) that it will produce an output signal in response to the incident light/photon is called Photon detection efficiency (ξ) (PDE). As given in the following equation it is a function of overvoltage ΔV and wavelength λ of the incident light.

$$\xi(\Delta V,\lambda) = f \cdot \eta \cdot P_G \qquad (7.3)$$

In the equation 7.3, f is a geometrical fill factor, η is quantum efficiency and P_G is the probability of Geiger discharge. Photon detection efficiency is the main and important characteristic of a SiPM.

7.1.4.1. Geometrical Fill Factor

The fill factor is actually related to the proportion of the light sensitive surface area of the SiPM. According to the SiPM structure, each microcell should be separated from its neighbor microcell for optical and electrical isolation reasons. In addition, a portion of surface area is needed for the quench resistor and signal paths. All these possibilities result in a 'dead space' around the microcell. The partition between microcells and the space needed for the quench resistor and tracking path is almost constant, despite of the microcell size. Consequently, larger microcells give higher percentage of active surface area (ratio of active area and total area).

High fill factor (larger microcells) outcomes in higher gain and PDE, but also in higher capacitances, lengthy recovery times and lesser dynamic range. A lesser fill factor (smaller microcells) not only results in lower gain and small value of PDE, but also in lower capacitances, shorter recovery times and higher dynamic range.[77]. The values of f ranges between ~30% to ~80%,[76] with the better value for the larger size of microcell.

7.1.4.2. Quantum efficiency

The probability that an incident light/photon generates a charge carrier (hole or electron) that is able to trigger Geiger discharge in the avalanche sector of the depletion region is known as quantum efficiency. The SiPM layered structure can be optimized by the Beers-Lambert law for the purpose that light absorption occurs in depletion layer for the preferred range of wavelengths. In depletion region the electric field separates the photo-generated electron-hole pair and inserts one of the charge carriers into the avalanche region. In exterior of the depletion region, the electric field is weak and the photo-generated electron-hole pair is expected to be recombined. The above detail concludes that quantum efficiency (η) is the function of wavelength.

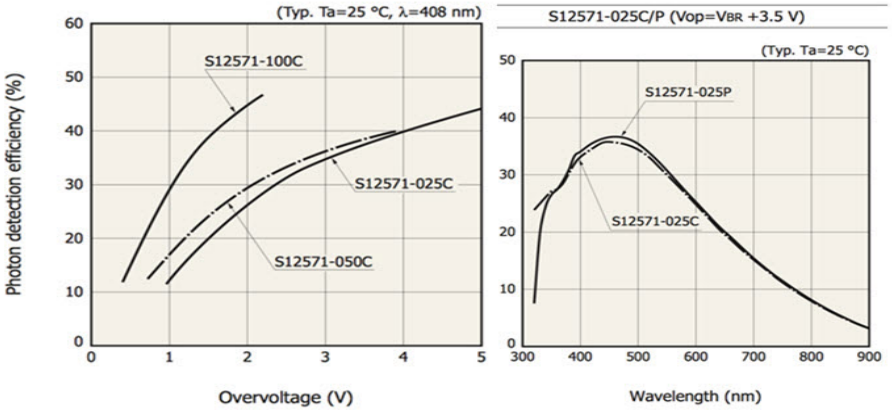

Figure: 7. 6 Samples of plot that show how ξ depends on ΔV and λ [76]

7.1.4.3. Probability of Geiger discharge

In the avalanche area, when injected charge carrier obtains enough kinetic energy from the electric field which goes beyond the ionization threshold, and might be capable to impact ionize silicon atoms, accordingly triggering an avalanche. The probability of this situation depends on following factors:

(1) Electric field strength, (which depends on ΔV)

(2) Avalanche region width, (which also controlled by ΔV)

(3) Collisional cross section of charge carriers with phonons and the particular history of these contacts.

when $\Delta V < 0$, the probability of Geiger discharge is extremely low. As ΔV rises above 0, the K.E of a charge carrier can get cross the ionization threshold energy and, besides, the width of the avalanche region increases, making the probability gradually higher. Inelastic scattering of charge carriers with phonons increases with ΔV, which confines steeply the probability of Geiger discharge rising with ΔV. In Figure: 7.6 samples of plot illustrating how ξ depends on ΔV and λ.

7.1.4.4. Responsivity

The responsivity is "the average photocurrent created per unit optical power" and is given by:

$$R = \frac{I_P}{P_{op}} \tag{7.4}$$

where, I_p is photocurrent and P_{op} is the incident optical power at a specific wavelength over the sensor area. The PDE is normally calculated from the responsivity of the sensor using equation 7.5. Responsivity unit is Amps per Watt (A/W).

$$PDE = \frac{R.h.c}{\lambda.M.e.(1+P_{AP}).(1+P_{XT})}.100\% \tag{7.5}$$

In eq 7.5 "h" is the Planck's constant, c is speed of light, λ is the wavelength of the incident light, M is the gain, and e is the elementary charge. P_{AP} and P_{XT} are the afterpulsing and crosstalk probabilities that are measured individually and are discussed in following sections. More detail about PDE can be found in [78].

7.1.5. Dark Count Rate

Dark count rate (DCR) is the key reason of noise in SiPM which is mostly due to the thermal electrons that are created in active region. DCR is a function of overvoltage, temperature and active area. Every dark add up is the effect of an avalanche in the volume of high field produced by thermal electron. The resulting signals from the microcell breakdown, due to either photon-generated or thermal electron generated, are identical. As a result, the thermal electrons make a source of noise at the single photon level. If a ΔV threshold is fixed above the single photon level then fake triggers from the noise can be considerably reduced. Though, the dark counts will still contribute to the measured signal.

As the dark count is composed of pulses series, its value or magnitude is estimated as a pulse rate (kHz), or pulse rate per unit area (KHz/mm^2). For continuous or current integration measurements, therefore it becomes more suitable to consider its contribution as a 'dark current'. The DCR can be calculated with a simple counting system, fixing a signal threshold at the half-photon level. The DCR increases with rising bias, creating an intrinsic trade-off between increasing PDE and DCR. The DCR also increases with increasing temperature and linearly with the active area, so a 3mm sensor will typically have 9 times the DCR of a 1mm sensor.

7.1.6. Optical Crosstalk

Optical cross talk is another factor of SiPM noise between microcells. It is a function of voltage and also influenced by the sensor fill factor. In avalanche process, inside the high field area the accelerated carriers will produce photons that may cause another avalanche in the nearby microcell. These secondary photons have tendency to be close to infrared (NIR) region and can cover considerable distance throughout the silicon. Normally 2x10^{-5} NIR photons are released per electron crossing the junction [77]. These photons (secondary) can move to adjacent microcells through: (a) directly to a adjacent microcell, (b) reflected from the window material (epoxy or glass) on the top of the sensor, or (c) bounced back from the base of the silicon substrate, as shown in Figure: 7.7a.

The crosstalk can be defined as "the possibility that an avalanching microcell will produce an avalanche in a second nearby microcell". The procedure happens immediately and as a result, single incident photons can sometimes creates signals corresponding to 2 or 3 photons, or even more. This phenomenon can be seen in Figure: 7.7b, which demonstrates the sensor's output in the dark, and here all of the signal pulses are because of dark counts. The middle dark count pulse given in Figure: 7.7b has a pulse height that is twice that of the other dark counts that is at the single photon level, and so will be most probably due to a crosstalk event. The optical crosstalk can be calculated by measuring the ratio of the count rate at the second photon level to the count rate at the single photon level. Figure: 7.18 illustrate the result of plotting the DCR as a function of threshold position, which makes a step-like plot. The flat regions of the curve correspond to the frequency of dark counts at the single, double, triple photon level etc. Significantly, this plot shows that with a threshold level set at the level of a ~3 photons, the dark count trigger rate will be small enough or negligible.

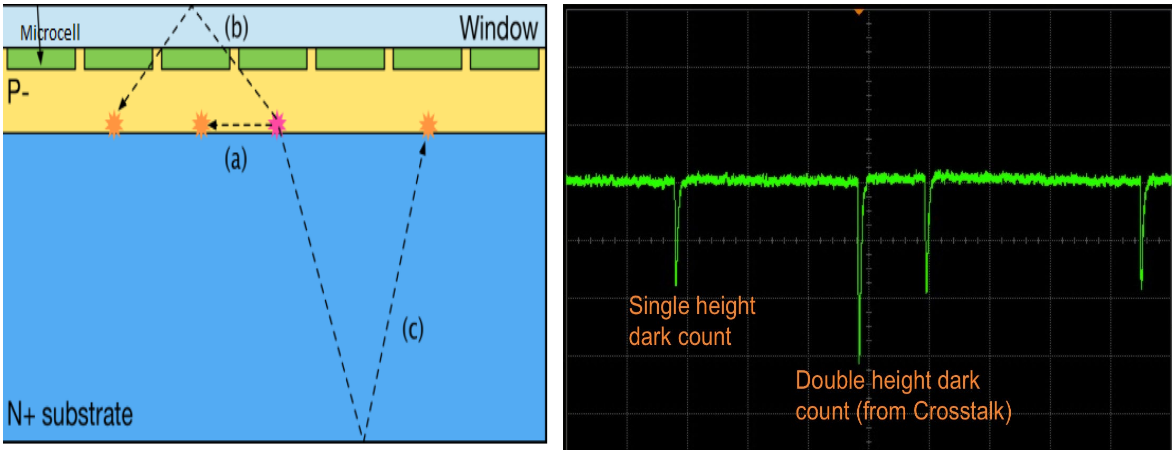

Figure: 7. 7 (a): An illustration of the different ways in which secondary photons can move (b) Oscilloscope shot showing dark counts photons can move to adjacent microcells to cause optical crosstalk.

7.1.7. Afterpulsing

During breakdown the carriers become trapped inside defects in the silicon. Following a several nanosecond delay, these trapped carriers can be free, potentially starting an avalanche and producing an afterpulse in that same microcell. Afterpulses of short delay which happen during the microcell recovery time likely have insignificant impact as the microcell is not completely charged. However, afterpulses having longer delay can affect the calculation with the SiPM if the rate is high. The probability of afterpulse is determined by measuring the statistical distribution of successive pairs of dark counts, when triggered at one half of the single photoelectron amplitude. Afterpulse probability gets increase with overvoltage (due to increased avalanche beginning probability). Afterpulsing in more detail including its measurement in SiPM sensors can be found in[78].

7.2. Experimental Setup

In this section the experimental detail including Apparatus used for experiment is given.

7.2.1. Apparatus

A schematic diagram of the experimental arrangement is shown in Figure: 7.8, whereas a photo of real setup is given in Figure: 7.13.

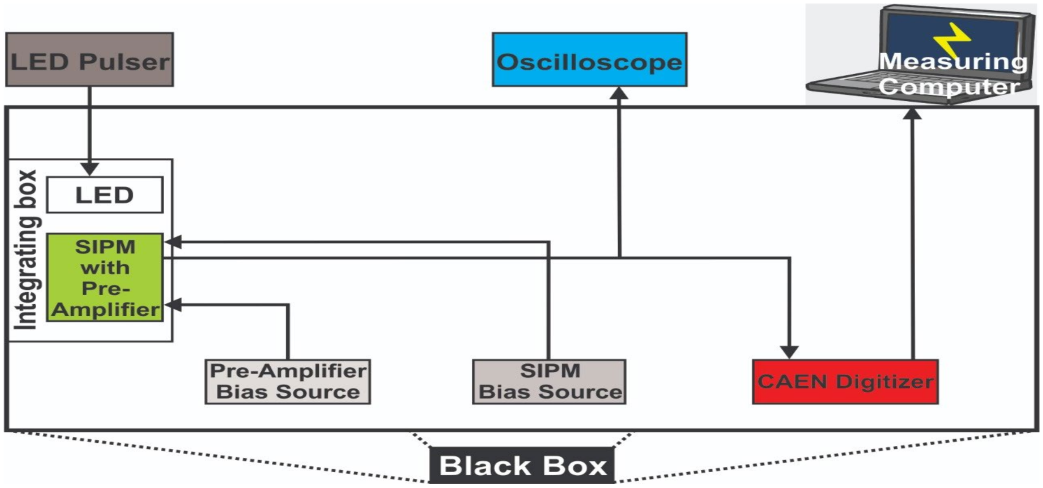

Figure: 7. 8 Schematic view of the experimental arrangement

7.2.1.1. Characterized Silicon Photomultiplier (SiPM)

In this work we have used a commercially available SiPM-Hamamatsu MPPC, type number S13360-3050CS and serial number 13787. The detail about parameters of this SiPM is given in Table: 7.1.

Type	Measurement Condition	Spectral response range λ (nm)	Peak sensitivity wavelength λp (nm)	PDE [9] at λp (%)	DRC [10] (max) (kcps)	Terminal capacitance (pF)	Gain M	Breakdown Voltage V_{BR} (V)	Crosstalk Probability %	Operating voltage V_{op} (V)	Temp coefficient at recommended V_{op} (mV/C)
S13360-3050CS	$V_{over} = 3V$	270-900	450	40	1500	320	1.7 x 10^6	53±5	3	$\mathbf{V_{BR}}$ +3	54

Table: 7. 1 Electrical & Optical Characteristics of SiPM at Typ. Ta 25 ^{0}C[79].

---

[9] Without crosstalk and afterpulse

[10] Threshold = 0.5 p.e

The aforementioned SiPM duly fixed on a PCB with preamplifier is shown in figure 7.9.

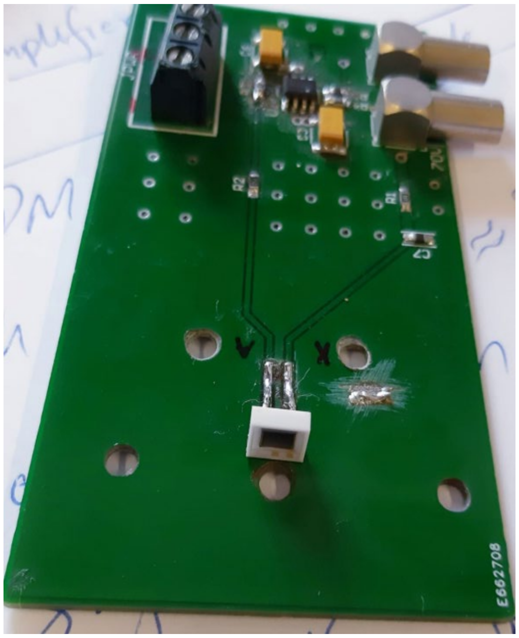

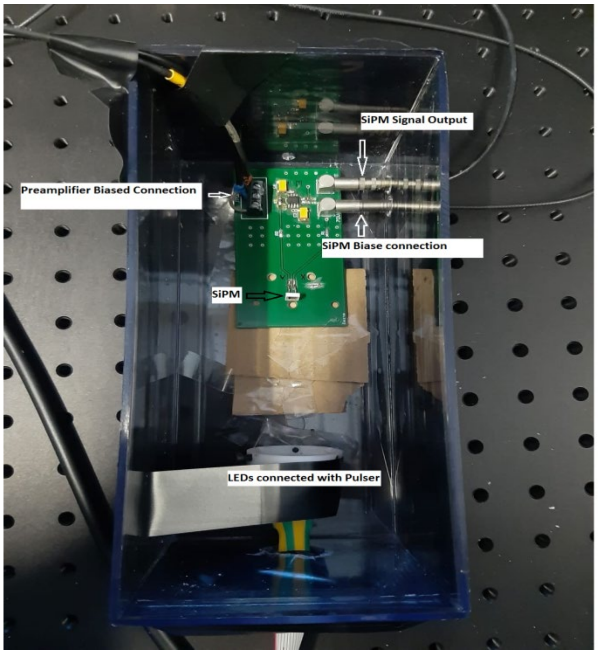

Figure: 7. 9 SiPM (S13360-3050CS) with Preamplifier. Figure: 7. 10 Measurement Setup of SiPM with LED in a closed box

In Figure: 7.9, a SiPM is shown which is fixed on PCB and connected with Preamplifier, at the opposite end the connections for Preamplifier voltage (in black), bias voltage input and signal output are given (two metals connections). The distance between the SiPM and LED is equal to 7.5 cm. This setup was then fixed inside a small closed box given in figure 7.10 with the LED to check the response of SiPM both in Dark and Light.

7.2.1.2. Power Supply Sources for Bias voltage

For the purpose to supply the bias voltage to SiPM, a high voltage power supply model NHQ 224M (2x4KV and 3 mA) was used which is made in EEC by ISEG. To bias the preamplifier with ±5 volt, an Agilent E3631A model supply is used.

7.2.1.3. Oscilloscope

To check the signal before doing online analysis an oscilloscope of Tektronix (TDS 3014B) is used. Both the oscilloscope and high power supply with CFD and a scalar are shown in Figure: 7.11.

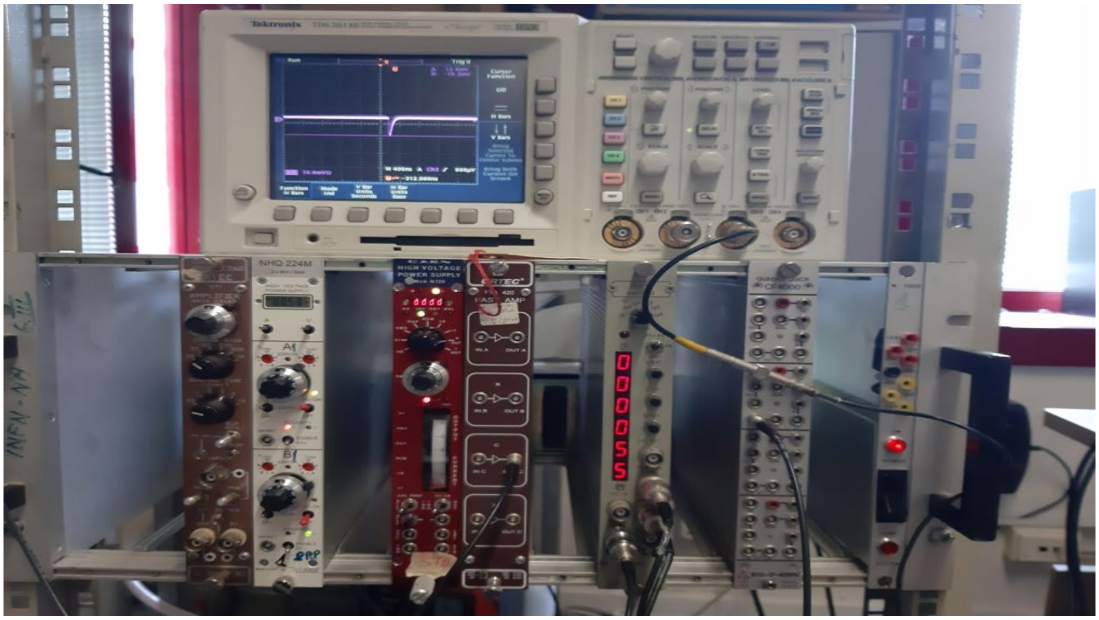

Figure: 7. 11 Instrumentation setup for measurement (Oscilloscope, High Power source, CFD and Scalar)

7.2.1.4. LED Pulser

An LED Pulser (AGB Scientific) is used to produce light of low energy and illuminate on the sensor. This Pulser has 10 output channels (LEDs), pulse width ranges in between 4 ns to 100 ns, the pulse rate has three values i.e 1 ms, 10 ms and 100 ms whereas the pulse intensity can be fixed from 0 to 2.5 mA. All these values are adjustable and user can select any of them according to their needs and requirements.

7.2.1.5. CAEN Digitizer

CAEN Desktop Digitizer (DT5730SB) has been used as a main ADC device which has 8 different channels, 14 bit resolution, 500 MS/s rate and 0.5 & 2 volt peak to peak dynamic range. Detail about this digitizer can be found in [80]. CAEN digitizer, LED Pulser and Preamplifier bias supply are shown in Figure: 7.12. The signal taken from digitizer is then analyzed by CoMPASS software which is an application able to manage the data acquisition from digitizers where a DPP (Digital Pulse Processing) firmware is installed. The software automatically detects the connected boards despite the communication interface, allows the user to set the DPP settings, displays the waveforms and histograms, and saves the data [81].

Figure: 7. 12 CAEN Digitizer (top), LED pulser (middle) and Power supply to bias preamplifier (bottom)

CAEN Compass software is used for measuring and taking data for both offline and online analysis of the signal which can be found in manual [81] in detail.

7.3. Measurement Procedure

SiPM characterization was done using the experimental setup shown in Figure: 7.13 as a whole including a big black box and other instruments (mentioned above) where ±5 volt bias is provided to preamplifier from power supply shown in Figure: 7.12. The electrical and optical properties of the sensor are given in Table: 7.1 whereas; structural and other properties are given in Table: 7.2.

Type No	Pixel Pitch μm	Effective Photosensitive area (mm^2)	Number of Pixels	Package	Fill factor %	Window material	Refractive Index of Window material	Operating Temp T_{op} ^0C	Storage Temp T_{stg} ^0C
S13360-3050CS	50	3.0 x 3.0	3600	Ceramic	74	Silicon resin	1.41	-20 to +60	-20 to +80

Table: 7. 2 Manufacturer specifications of SiPM[79]

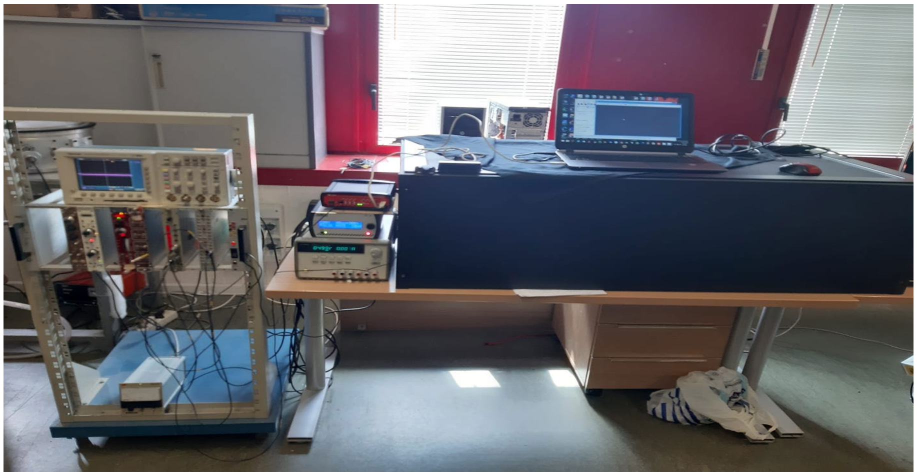

Figure: 7. 13 Experimental setup used for all test, at room Temperature

7.3.1. Signal output waveform

As mentioned above, test were done using CAEN digitizer and CAEN Compass software for signal analysis and other measurements. Tests were done both under dark and under light using LED Pulser (shown in Figure: 7.12). The signal was first examined using oscilloscope, where the magnitude and width of the signal was observed, and the crosstalk and afterpulses were clearly noticeable as shown in Figure: 7.14. SiPM produces a typical signal when any of the cells walks off to breakdown. The amplitude Ai is proportional to the capacitance of the cell times the overvoltage. $A_i \sim C \bullet (V - V_{br})$ When many cells fire at the same time the output is the total of the standard pulses $A = \sum A_i$.

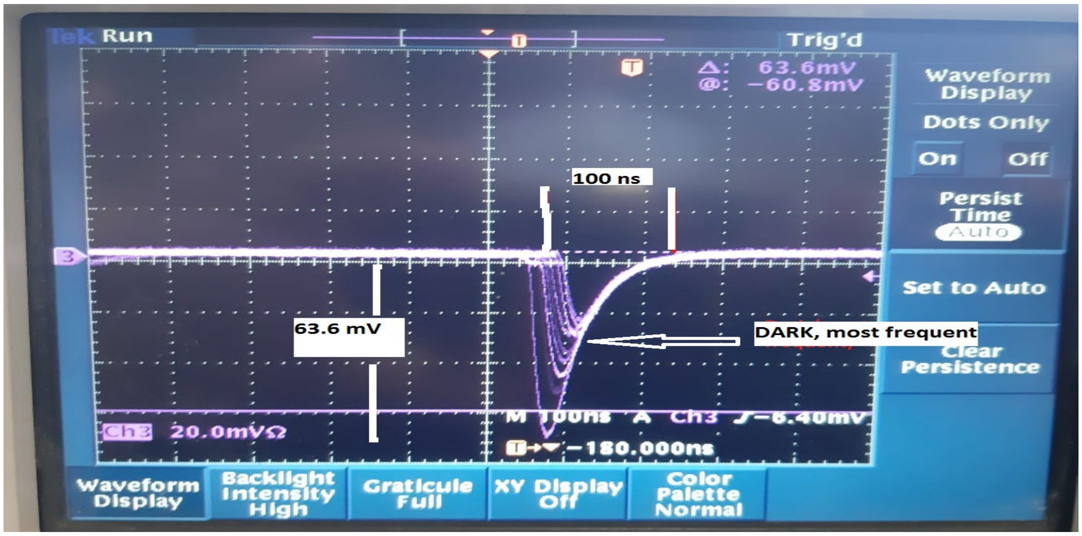

Figure: 7. 14 Discrete Nature of the SiPM shows the output when illuminated by brief pulses of Low-level light (Oscilloscope Shot)

When there is no crosstalk happens, the produced waveform looks like the one 1 p.e. in the figure 7.14. If the primary avalanche is come with one secondary crosstalk discharge, the resultant waveform looks like 2 p.e, is a superposition of two 1 p.e. waveforms. If it is accompanied by two, a 3 p.e. waveform results, and so on. The Figure: 7.14 is an oscilloscope trace with the display set to persistence mode where the pulse width is 100 ns and the given magnitude is 63.6 mV. The SiPM is illuminated by LED pulser having the properties given in table 7.3; the 1 p.e. waveforms are due to dark counts. The most frequent events are 1 p.e., followed by 2 p.e., 3 p.e., etc. All of the waveforms that are different from 1 p.e. are due to different simultaneously fired diodes because of the light or crosstalk. The same shot of the signal took from CAEN digitizer is shown here in Figure: 7.15, this is the resulting signal for light of 405 nm wavelength, 2.05 mA pulse intensity, 52 ns width with 10 ms pulse rate, the bias voltage is 52.5 V.

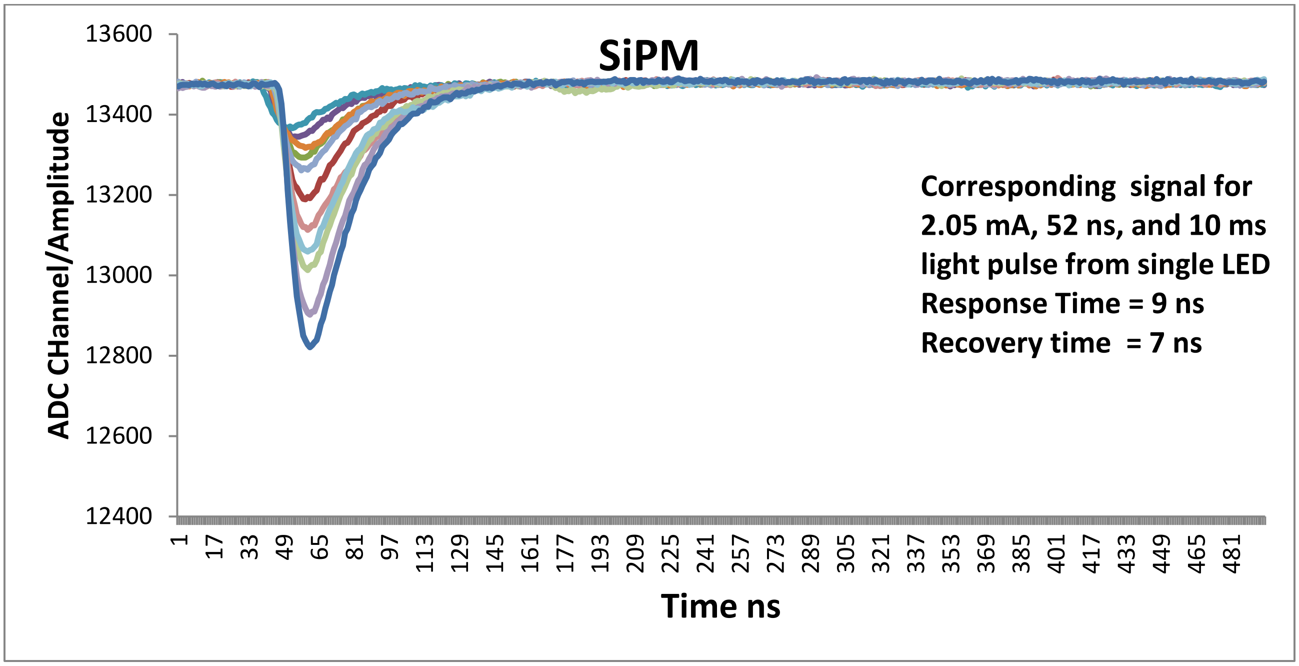

Figure: 7. 15 The Discrete Nature of the SiPM Output when Illuminated by the LED Pulser, taken from Digitizer.

The pulse height spectrum for the same light pulse having same intensity, width and rate is shown in Figure: 7.16.

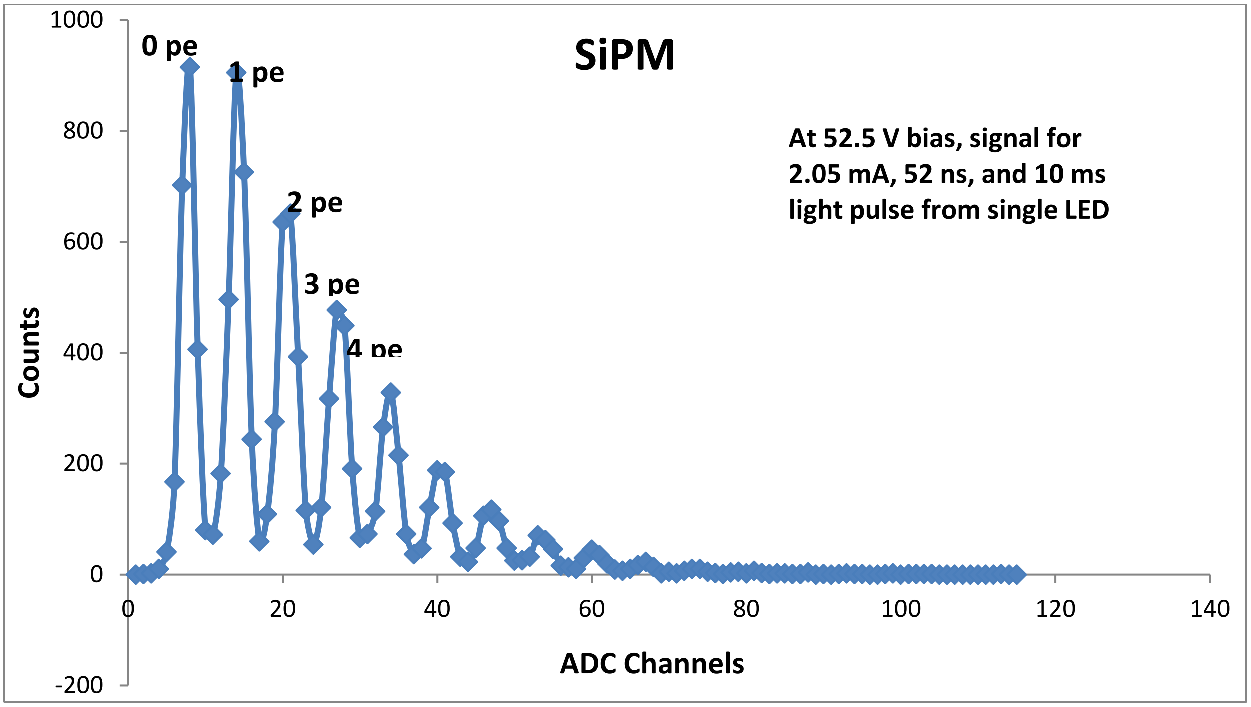

Figure: 7. 16 Pulse height spectrum of light pulses with very low intensity recorded with a SiPM

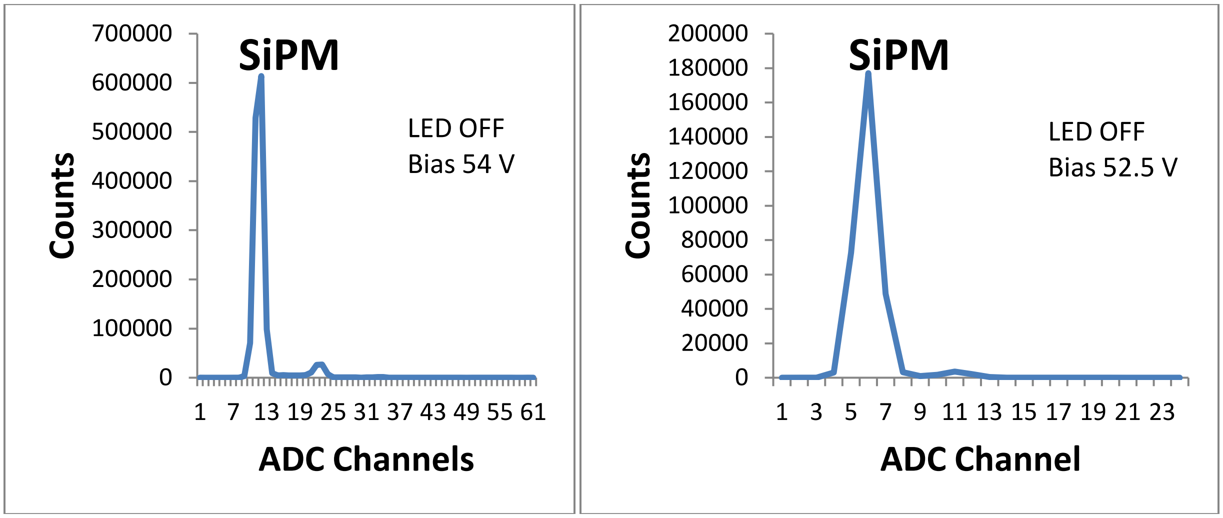

Figure: 7. 17 Pulse height spectra for two different bias voltages under dark

One LED (no 1 of Pulser), blazed with the characteristics given in Table: 7.3 wide voltage pulses, illuminated the SiPM. The signals from the SiPM are amplified in preamplifier, and analyzed in CAEN digitizer ADCs. An example of the pulse height distribution is shown in Figure: 7.16 where single photons clearly can be detected with SiPM‘s. The pulse height spectrum shows a resolution which is even better than what can be achieved with a hybrid photomultiplier. The fit of a sum of four gaussian functions to the pulse height distribution provides the gain and the number of detected photons. The gain is proportional to the distance between the photo-peaks, whereas the number of photoelectrons, N_{pe}, is equal to the ratio of the average of the pulse height distribution (corrected for the dark count contribution) to the gain. In Figure: 7.17 spectra without light for two different bias voltages are given, as compare to 52.5V for 54 V bias shows a huge increase in dark count rate.

7.3.2. Dark Count Rate Vs Threshold

Dark count rate is defined in section 7.1.5 in detail here we present DCR as a function of threshold for different biases voltage. As the dark count is consists of a series of pulses, its magnitude is given as a pulse rate (kHz), or pulse rate per unit area (KHz/mm^2). For continuous or current integration measurements, it is occasionally more suitable to consider the contribution as a ‘dark current’.

The DCR is measured with a simple counting system, setting a leading edge threshold. As expected (see Figure: 7.17) the DCR increases with increasing bias as shown in Figure: 7.18, creating an intrinsic trade-off between increasing PDE and DCR. The DCR also increases with increasing temperature and linearly with the active area[77].

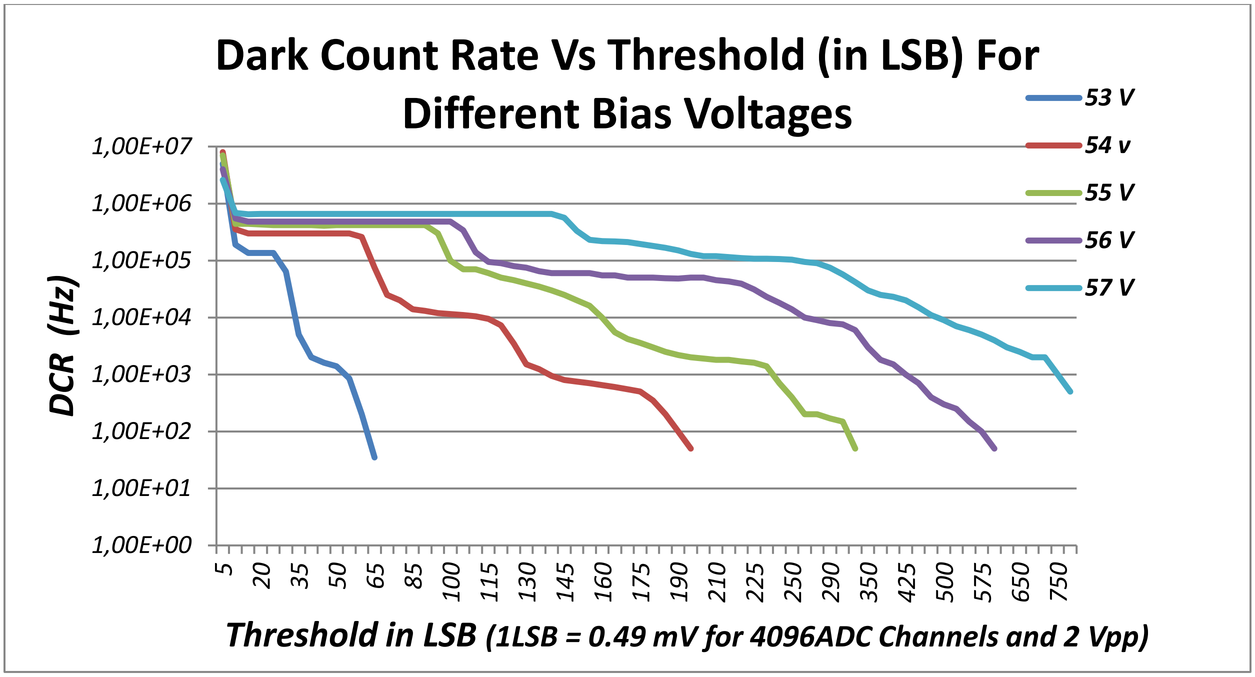

Figure: 7. 18 DCR as a Function of Threshold for Different Biases

7.3.3. Real time Measurements with Compass (CAEN Software)

As mentioned above **CoMPASS** is the novel software from CAEN able to put into practice a Multi-parametric DAQ for Physics Applications, where the detectors can be linked directly to the digitizers' inputs and the software obtains energy, timing, and PSD (Pulse shape discrimination) spectra. CoMPASS software has been designed as a user-welcoming interface to handle the acquisition with the entire CAEN DPP algorithm. CoMPASS can handle multiple boards, even in synchronized mode, and the event correlation between many channels (in hardware and/or software), apply energy and PSD cuts, compute and show the statistics (trigger rates, data throughput, etc...), save the output data files (raw data, lists, waveforms, spectra) and use the saved files to run off-line with different processing parameters. Using this software in the following are some spectra (screenshots) discussed in detail:

7.3.3.1. Pulse Height/Photoelectron Spectrum

Silicon photomultipliers are recognized to have exceptional photon counting abilities. Its few or single photoelectron spectrum is described by well separated peaks relating to consecutive number of detected photons. Example of such spectrum is presented in Figure: 7.19 which is recorded using compass software. The spectrum in Figure: 7.20 recorded by the SiPM without any light is compared to the spectrum when the sensor is illuminated (Figure: 7.19). A cut of low channels and high channels (20 and 100) was applied to the spectrum in Figure: 7.19. Using this cut to consider only region of the pulse height spectrum where the contribution of dark current is negligible.

Wavelength of Light	Number of LED	Pulse Intensity	Pulse Width	Pulse Rate
405 nm	01	2.2 mA	48 ns	10 ms

Table: 7. 3 Light Pulse Properties

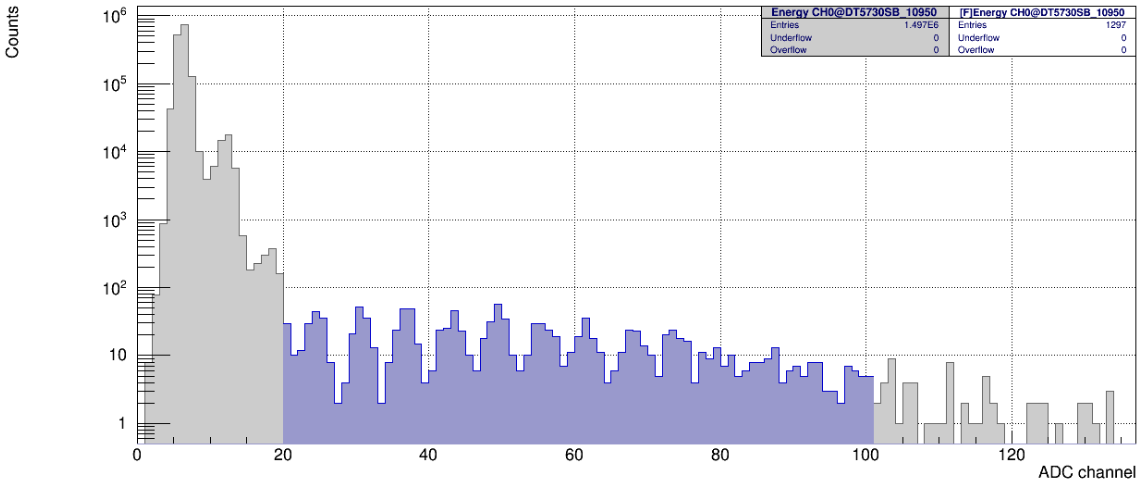

Figure: 7. 19 Energy Spectrum Screenshot recorded by compass using SiPM under the illumination of low level light

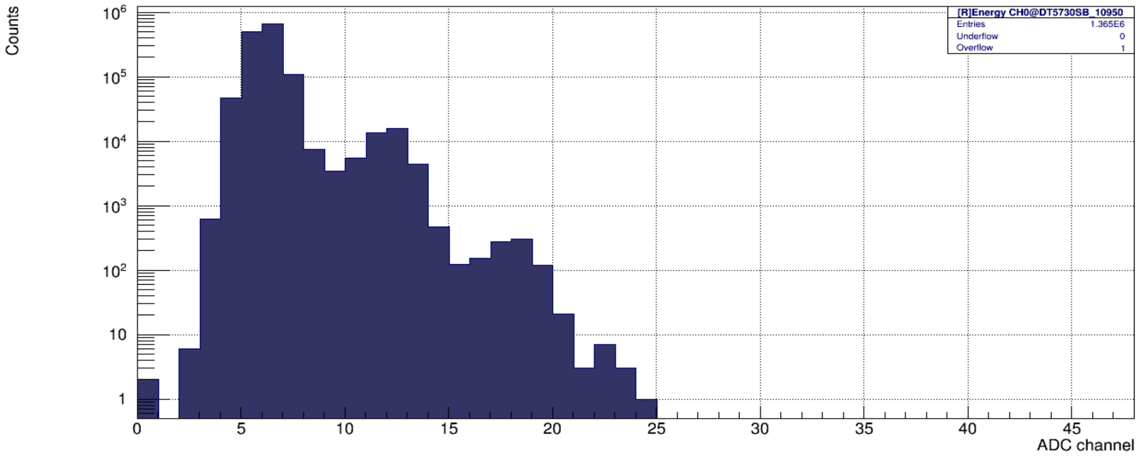

Figure: 7. 20 Energy Spectrum Screenshot recorded by compass using SiPM under dark

7.3.3.2. Signal Waveform in CoMPASS

Waveform digitizers are well suited for physics, medical, homeland security and industrial applications. CAEN built up also numerous digital pulse processing algorithms that allow the user to collect a set of important information like energy, precise timing, PSD and so on.

Algorithms based on the waveform analysis (Pulse Shape Discrimination-PSD) are very important in order to discriminate between the different particles producing the signals, for instance Gamma and Neutron. The slow and fast components are used by the algorithm to compute the PSD, according to the formula:

$$PSD = \frac{Q_{Long} - Q_{short}}{Q_{Long}} \tag{7.6}$$

which corresponds to the ratio between the integral of the tail ($Q_{long} - Q_{short}$) and the total charge (Q_{long}).

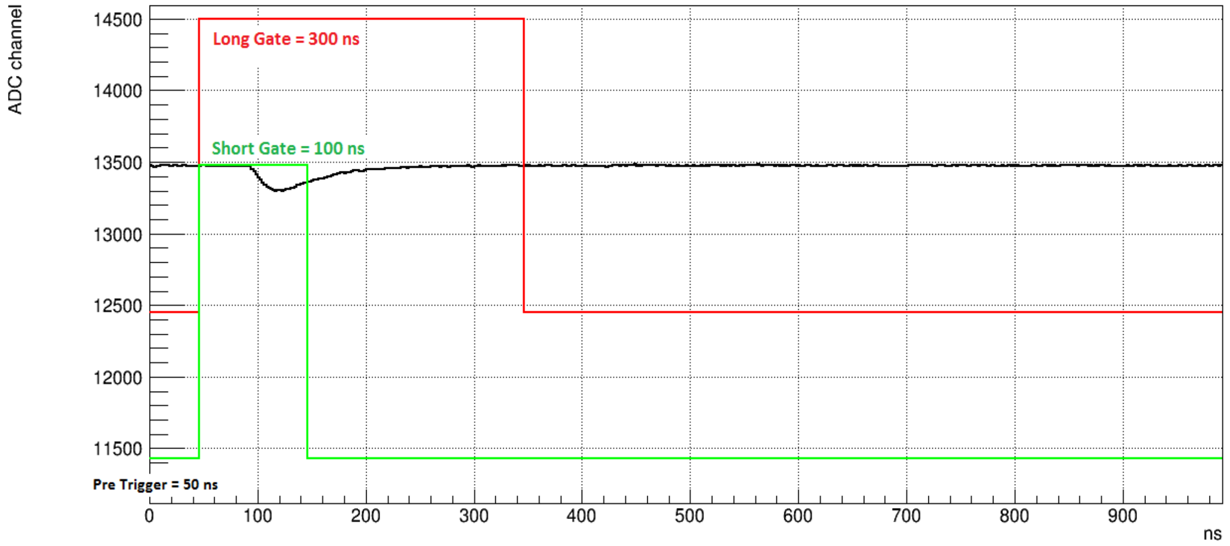

Figure: 7. 21 Screenshot from CoMPASS, summarizing the DPP-PSD parameters. The trigger fires as soon as the signal crosses the threshold value. Long Gate, Short Gate, Pre-Trigger, and Record Length are also shown for one acquisition window

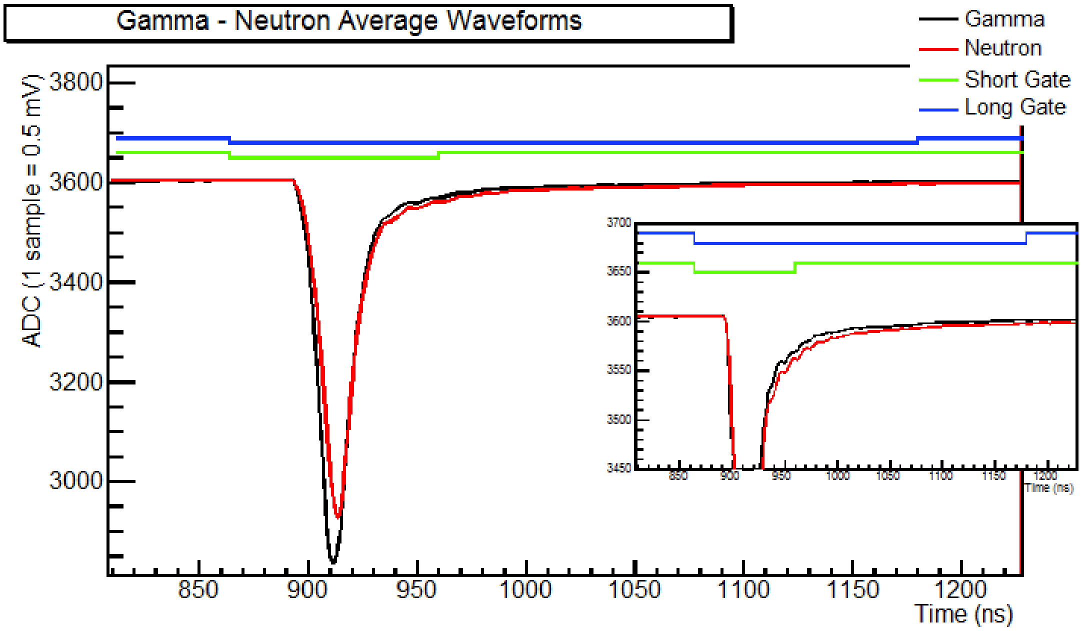

Figure: 7. 22 Plot of typical γ-Neutron waveforms [81].

In Figure: 7.22 we show an example of signals from neutrons and gamma, where it is possible to see a difference in the waveform shapes; the slow and fast components are used by the algorithm to compute the PSD, according to the formula 7.6, are also shown:

7.3.3.3. PSD vs Energy Spectrum

This spectrum is normally use to identify and distinguish two different signals coming from different sources just like doing discrimination of Gammas and Neutrons. Here we are just showing the detail of PSD-ADC channel two dimensional spectrum for both dark and light with specified cuts. In Figure: 7.23 corresponding to the dark we recognize the three peaks shown in Figure: 7.20. Figure: 7.23, Figure: 7.24 and Figure: 7.25 show the same two dimensional spectra with light without any cut on the channels and with cuts in order to eliminate the noise associate to the dark, respectively.

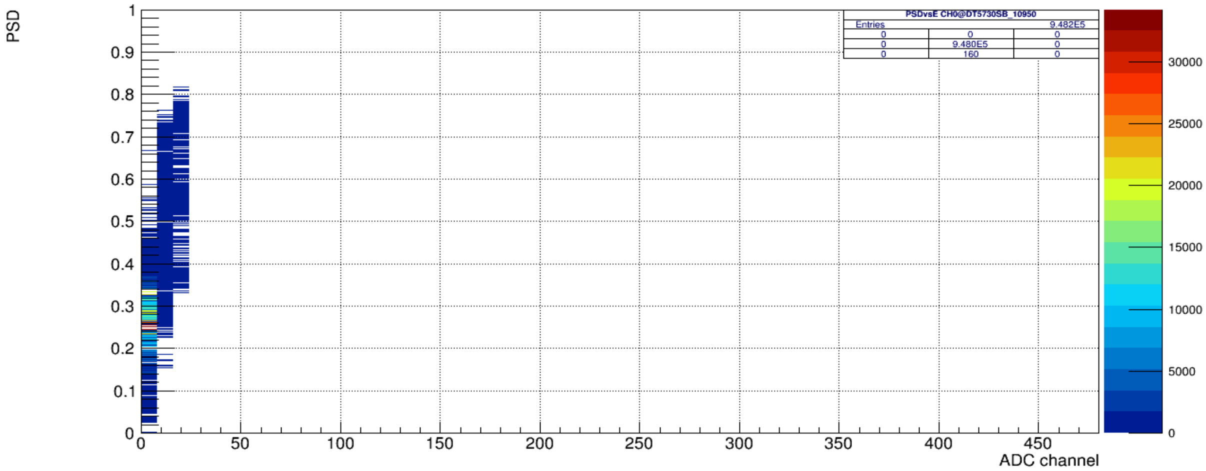

Figure: 7. 23 PSD verses Energy spectrum recorded using SiPM under dark condition

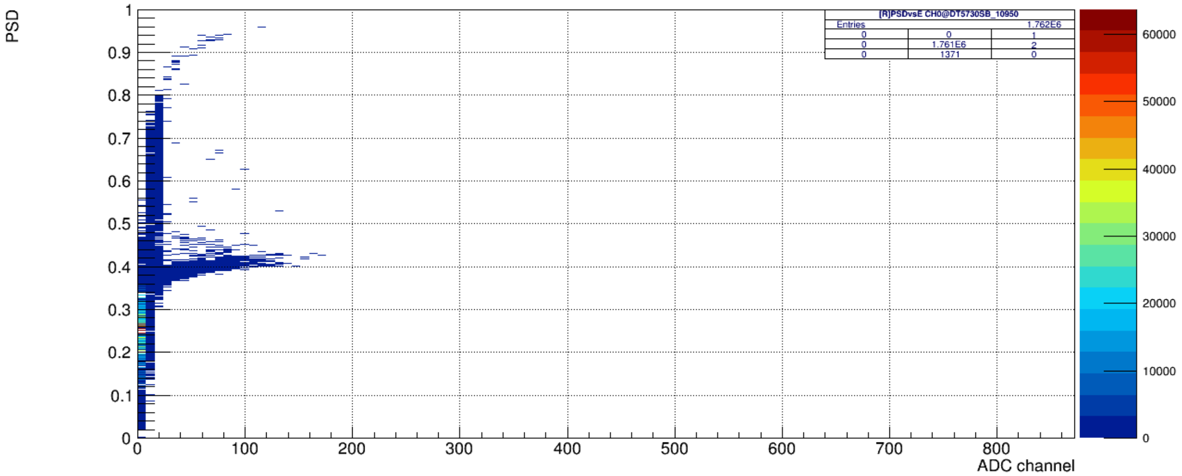

Figure: 7. 24 PSD verses Energy spectrum recorded using SiPM under light (table 7.3) condition (both dark and light are shown)

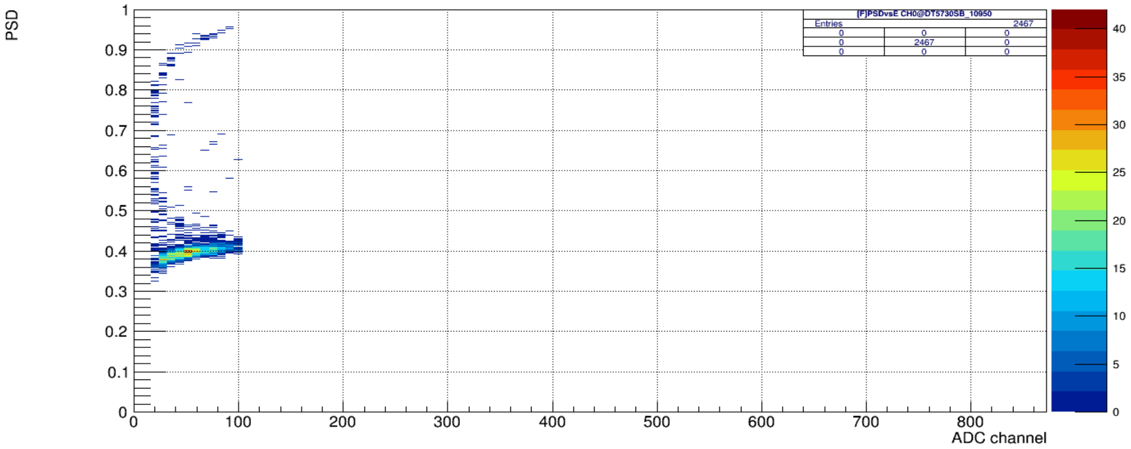

Figure: 7. 25 PSD verses Energy spectrum recorded using SiPM under light only (cut applied) condition

The PSD algorithm could be important to discriminate between light produced by proton in Cherenkov and photon producing by other sources passing by near.

7.3.3.4. Counts vs PSD Spectrum

As comparing the Figure: 7.24 and Figure: 7.26 it is confirmed the accuracy of pulse shape in both the light pulse is at 0.4 on PSD (x axis in Figure: 7.26 and y axis in Figure: 7.25). Furthermore, from Figure: 7.26 we can see that first histogram in Figure: 7.20 approximately corresponds to the pulse shape from 0 to 0.5, for second it is approximately 0.25 to 0.75 and the third one is 0.35 to 0.80 (one can also confirm from Figure: 7.23). This kind of spectrum also helps to discriminate different types of pulses.

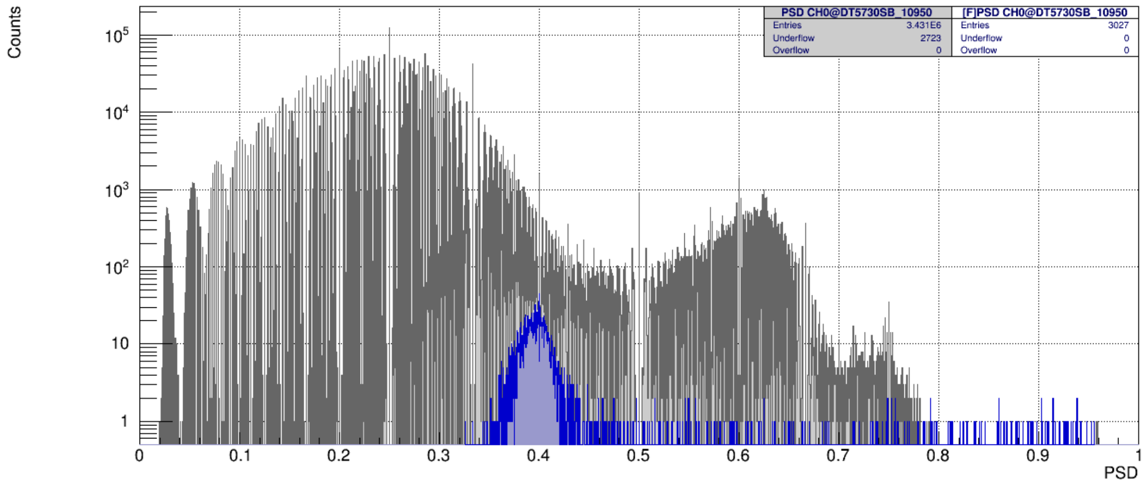

Figure: 7. 26 The PSD spectrum of the same SiPM with applied cut for light (blue only)

7.3.3.5. Time Spectrum

The silicon active layers are very slim (2–4 mm), the avalanche breakdown practice is quick and the signal amplitude is large. Hence, good quality timing properties even for single photons can be expected. Fluctuations in the avalanche process are mostly because of the lateral scattering by diffusion and by the photons produced in the avalanche[82]. The vertical build-up contributes only small to the timing. Figure: 7.27 shows a measurement of the time response of a G-APD for single photons [83].

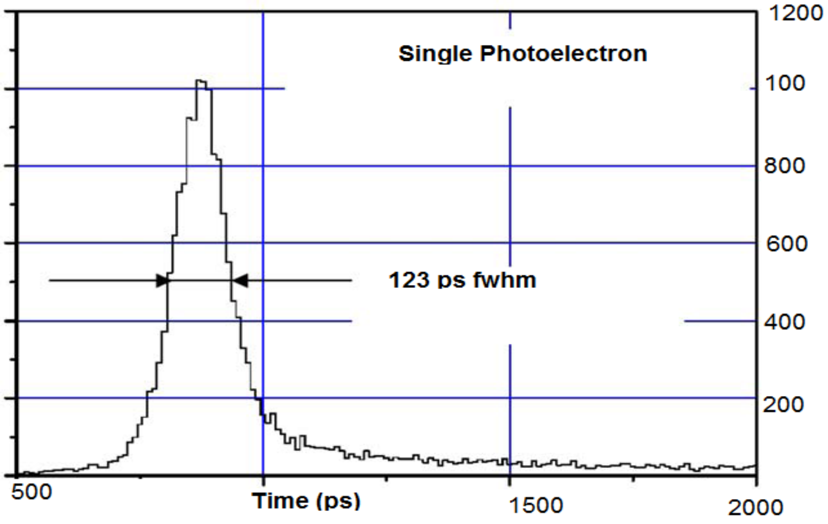

Figure: 7. 27 Time resolution for single photons.

The authors stated a 40 ps contribution from both the used laser and the electronics (each). The result then is a time resolution with a standard deviation of 42 ps Operation at high overvoltage (high gain) improves the time resolution.

The tail to the right of the peak in Figure: 7.27 can be explained by carriers created in field free regions which have to travel by diffusion. It can take several tens of nanoseconds until they reach a region with field and trigger a breakdown. We have verified such a behavior in our measurement as shown in Figure: 7.28 where we reported a time spectrum measured for the SiPM illuminated by the pulse.

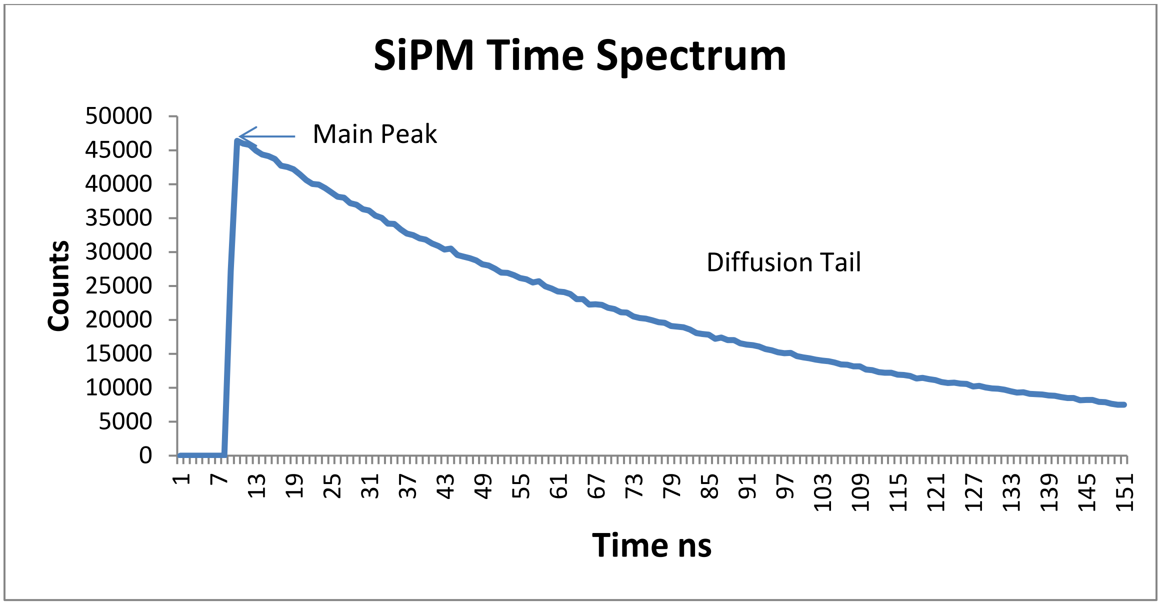

Figure: 7. 28 Time spectrum for SiPM with light pulse given in table 7.3

Time spectrum corresponding to that shown in Figure: 7.19, with channel cut (20 to 100), is also given in Figure: 7.29 where the events conditioned by the cut are shown blue. As previously shown the condition to impose by channel cut allows selecting most of the events coming from the light and essentially free from dark noise. More detail is provided in the next section.

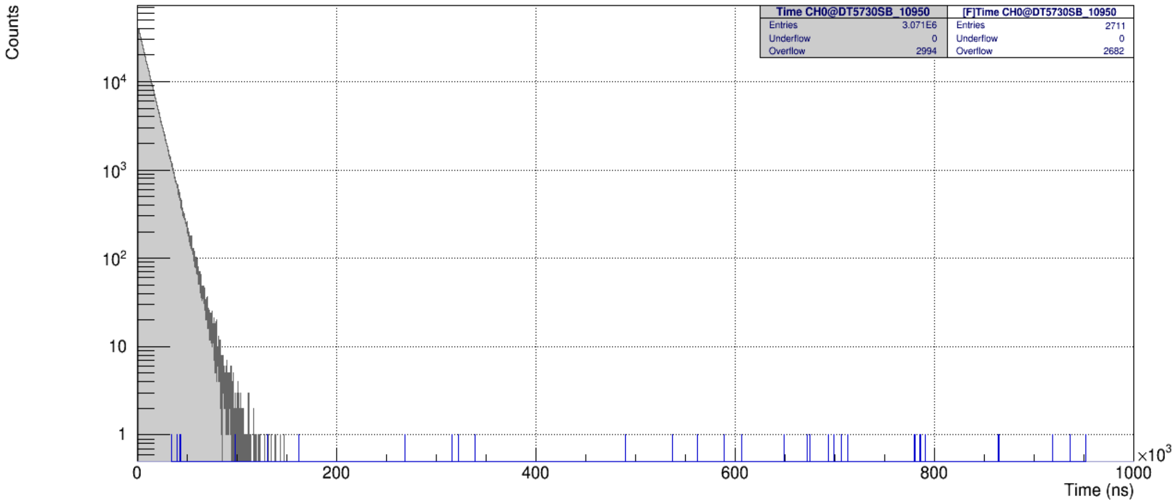

Figure: 7. 29 Same of graph in fig 7.28 in compass with blue marked events corresponding to the channel cut selecting pulses of light only

7.3.3.6. Time Spectrum at Different Pulse Height Threshold

The time spectrum is actually the exponential combination of all the histograms concerning to both dark noise and light. In order to study in detail the behavior of the time spectrum, we have measured this latter for different pulse height thresholds, set in leading edge. In particular, we have collected time spectra for different values of lsb (least significant bit, 1 lsb = 0.49 mV). They are shown in Figure: 7.30. It is observed that increasing the threshold value upto a certain limits, the time spectrum acquires a less steep exponential behavior which appear to be nearly uniform for high thresholds. As in our measurement the value of threshold of 20 lsb allow to significantly reducing the dark noise, the time spectrum corresponding to this threshold represents the best compromise to obtain a reasonable ratio between counts coming from light pulses and dark noise pulses.

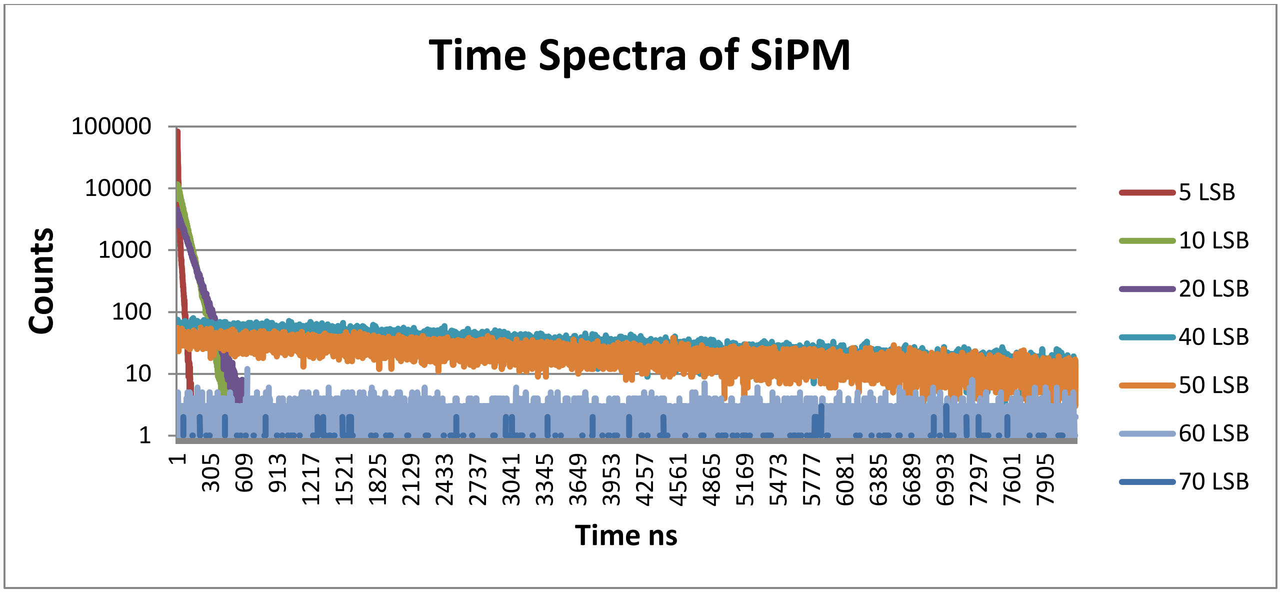

Figure: 7. 30 SiPM Time Spectra at different Thresholds

For further understanding, consider Figure: 7.31(a) and (b) where the pulse height spectrum and the corresponding time spectrum are shown respectively, with SiPM in the dark. Here we have also selected on the first spectrum the second peak (the selected area is shown in blue). The time spectrum conditioned by the selection on the first one, is also shown in blue in Figure: 7.31 b. From this fig we observed that without any selection of the pulse height spectrum, the time spectrum has a steep exponential distribution, while this distribution becomes wider for the selected events. The width will be even larger for the events corresponding to the third peak.

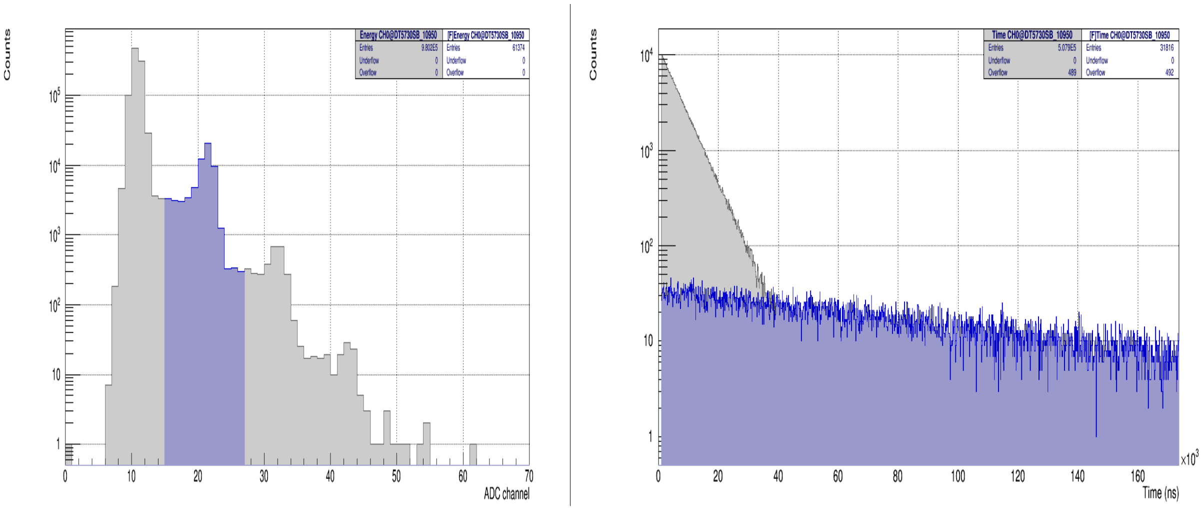

Figure: 7. 31 (a) Energy Spectrum of SiPM (left), (b) Corresponding Time spectrum (logarithmic) with same energy cut for second peak.

7.3.3.7. Dead Time Evaluation

When a pulse is processed by an analog chain block, the maximum read-out rate is limited by the need to complete the processing of the current pulse before being able to process a successive valid signal. When the processing time of a pulse is larger than the time interval before the arrival of the next pulse, the analog chain is "temporarily blind" and misses one or more successive pulses. The actual live counting time is therefore smaller than the total counting time, and the difference between total time and live counting time is called "Dead time". The Digital MCA (multi channel analyzer) read out capability is rather independent from the ADC sampling time and processing speed as well as from the signal width, and in general allows for higher counting rates than the analog chain. The digital MCA dead time is provides also information on the relationship between total measurement time and live counting time values. The CoMPASS software is able to automatically evaluate the dead-time including the contributions of *pileup events*, saturation events, and Trigger Hold-Off (see Sec. Dead time evaluation in CoMPASS [81]).

CoMPASS provides dead time evaluation based on the data coming from the board and allows the user to have access to the data to evaluate the dead time. CoMPASS indeed allows the user to save the *Raw* acquisition data, i.e. including the saturations and pileup events usually not included in the spectra but required to provide the dead time estimation. Following the procedure given in the manual we have calculated percentage of dead time for Dark noise at 53 V bias voltage, using the following formula:

$$1-\frac{(\mathrm{OCR}\ +\ \mathrm{events\_discarded\_by\_user\_selection}\ +\ \mathrm{saturation\_events})}{ICR} \tag{7.7}$$

where both ICR (Input count rate) and OCR (output count rate) are corresponding actual number of events.

Using the measured values ICR = 173 KHz, OCR = 32 KHz and other values equal to zero as no saturation and discarded events were present, we calculated value of the dead time 0.81% without any applied cut, as shown in Figure: 7.32.

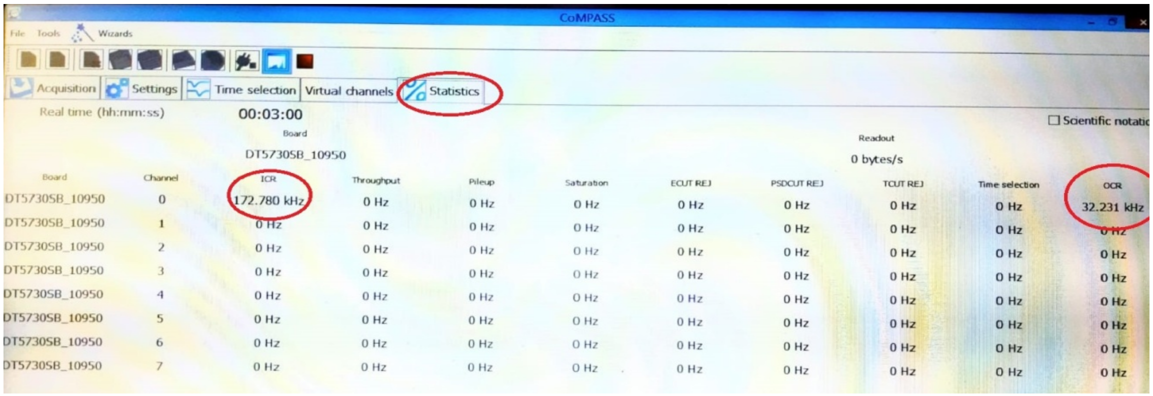

Real time (hh:mm:ss) 00:03:00

Board DT5730SB_10950

Readout 0 bytes/s

Board	Channel	ICR	Throughput	Pileup	Saturation	ECUT REJ	PSDCUT REJ	TCUT REJ	Time selection	OCR
DT5730SB_10950	0	172.780 kHz	0 Hz	0 Hz	0 Hz	0 Hz	0 Hz	0 Hz	0 Hz	32.231 kHz
DT5730SB_10950	1	0 Hz	0 Hz	0 Hz	0 Hz	0 Hz	0 Hz	0 Hz	0 Hz	0 Hz
DT5730SB_10950	2	0 Hz	0 Hz	0 Hz	0 Hz	0 Hz	0 Hz	0 Hz	0 Hz	0 Hz
DT5730SB_10950	3	0 Hz	0 Hz	0 Hz	0 Hz	0 Hz	0 Hz	0 Hz	0 Hz	0 Hz
DT5730SB_10950	4	0 Hz	0 Hz	0 Hz	0 Hz	0 Hz	0 Hz	0 Hz	0 Hz	0 Hz
DT5730SB_10950	5	0 Hz	0 Hz	0 Hz	0 Hz	0 Hz	0 Hz	0 Hz	0 Hz	0 Hz
DT5730SB_10950	6	0 Hz	0 Hz	0 Hz	0 Hz	0 Hz	0 Hz	0 Hz	0 Hz	0 Hz
DT5730SB_10950	7	0 Hz	0 Hz	0 Hz	0 Hz	0 Hz	0 Hz	0 Hz	0 Hz	0 Hz

Figure: 7. 32 Compass Statistics Tab showing ICR and OCR values recorded by SiPM under dark

In Figure: 7.33 we have shown the evaluated dead time when a selection is applied on the first peak/histogram, the discarded events are also given in the figure.

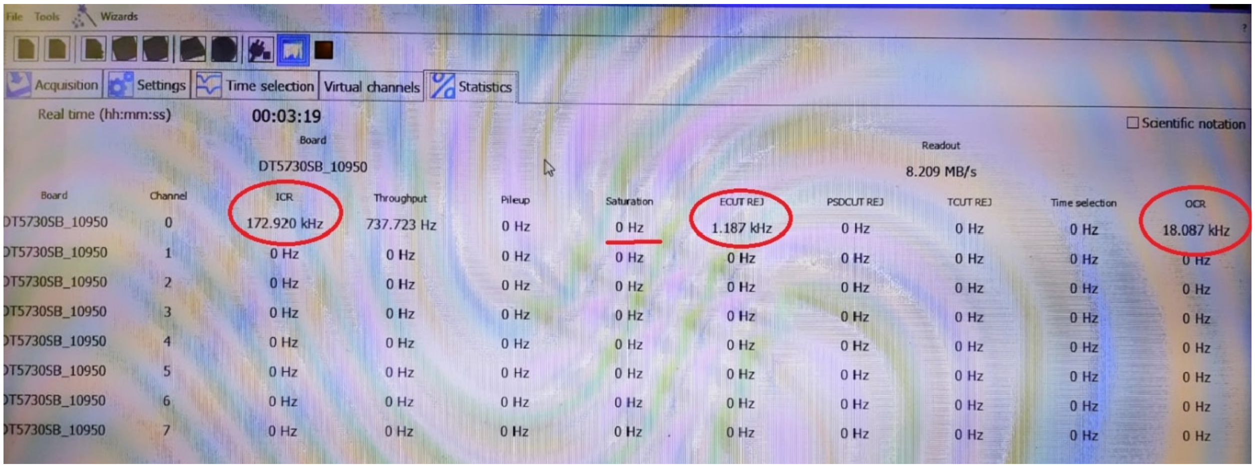

Real time (hh:mm:ss) 00:03:19

Board DT5730SB_10950

Readout 8.209 MB/s

Board	Channel	ICR	Throughput	Pileup	Saturation	ECUT REJ	PSDCUT REJ	TCUT REJ	Time selection	OCR
DT5730SB_10950	0	172.920 kHz	737.723 Hz	0 Hz	0 Hz	1.187 kHz	0 Hz	0 Hz	0 Hz	18.087 kHz
DT5730SB_10950	1	0 Hz	0 Hz	0 Hz	0 Hz	0 Hz	0 Hz	0 Hz	0 Hz	0 Hz
DT5730SB_10950	2	0 Hz	0 Hz	0 Hz	0 Hz	0 Hz	0 Hz	0 Hz	0 Hz	0 Hz
DT5730SB_10950	3	0 Hz	0 Hz	0 Hz	0 Hz	0 Hz	0 Hz	0 Hz	0 Hz	0 Hz
DT5730SB_10950	4	0 Hz	0 Hz	0 Hz	0 Hz	0 Hz	0 Hz	0 Hz	0 Hz	0 Hz
DT5730SB_10950	5	0 Hz	0 Hz	0 Hz	0 Hz	0 Hz	0 Hz	0 Hz	0 Hz	0 Hz
DT5730SB_10950	6	0 Hz	0 Hz	0 Hz	0 Hz	0 Hz	0 Hz	0 Hz	0 Hz	0 Hz
DT5730SB_10950	7	0 Hz	0 Hz	0 Hz	0 Hz	0 Hz	0 Hz	0 Hz	0 Hz	0 Hz

Figure: 7. 33 Compass Statistics Tab showing ICR and OCR values recorded by SiPM under dark with cut for single peak

Finally, using the measured values ICR = 173 KHz, OCR = 18 KHz and Discarded events = 1.1 KHz the determined dead time percentage is 0.89%. Similarly, applying a selection on the second peak as shown in Figure: 7.31 we obtained value of dead time 0.98 % with counting rate of 1000 Hz applying E cut, for ICR = 173 kHz, OCR = 137 Hz.

7.4. Conclusions and Future Perspectives

In the near past, SiPM have got quick development in nuclear and particle physics research and experimentations. This adoption is determined by capabilities and properties of SiPMs that deal with the requirements of contemporary particle and nuclear physics research. These properties are, insensitivity to magnetic fields, fine photon detection efficiency, low bias voltages and a very little and compact size. These characteristics present the foundation for novel ideas in detector systems combined with the progress in modern microelectronics, which facilitate the production of detector systems with large numbers of electronics channels, based on optical readout. SiPMs can not only replace classical photomultipliers and other light detectors but also make possible new applications which were not possible before, particularly in systems having large numbers of electronic channels and/or stringent space limitations.

The applications of SiPMs in particle discrimination and veto systems can be generally categorized in three groups of detector technologies: 1) Cherenkov detectors, where SiPMs are used to detect the Cherenkov light directly, 2) Plastic scintillators-based charged particle and shower detectors where SiPMs are utilized to detect scintillation light, and 3) time-of- flight detectors.

Conclusively, keeping in mind all the analysis mentioned above, SiPM has the potential to replace the PMTs used in Cherenkov Detector UA9 Experiment at CERN as it is already used in [84].

The main purpose of all the above analysis and discussion is to go deep in understanding the basic parameters of the signal recorded by SIPM. This study can be considered as a starting point to realize a real time monitoring system in the framework of a future update of the Cherenkov detector at UA9. In particular, such a system would unify the process of algorithm development and system implementation just like done in real time framework for Thomson scattering experiment [85]. An important feature of Real-Time Framework realized in the said experiment is the possibility to configure accurately the deployment of an application by varying input and output data sources as well as parameters without recompiling the application.

CONCLUSIONS

Improved beam collimation systems for the Large Hadron Collider (LHC) at CERN are one of the important requirements for its future upgrade. In this respect, the use of crystal based collimators represents an excellent solution for both ion and proton beams, as these collimators allow reducing the system contribution to the machine impedance. Using the concept of bent crystal channeling, quality work with promising results has been carried out in numerous beam tests in UA9 experiment at Super Proton Synchrotron (SPS), at CERN.

The main goal of this dissertation was to design a prototype for real time monitoring of crystal based collimation system to upgrade in the future the present one, based on a Cherenkov detector and other related instruments. Following this goal, we have characterized various types of crystals to check its potential for collimation systems in LHC and SPS. In particular, the crystals STF123, STF126, ACP83 and ACP85 have been analyzed, obtaining very similar results to those reported in the literature[49]. The efficiency and the deflection angle (at ±4 *μrad* angular cuts) of crystal STF126 were obtained as (68.0 ± 0.2) % and (50.5 ± 0.2) *μrad* , respectively. Similarly, for crystal ACP85 the obtained values for these quantities were (67.2 ± 0.2) % and (50.1 ± 0.2) *μrad* respectively. Radiation hardness tests of some crystals were also carried out to check the potential of crystals to work inside high radiation environment. These tests confirmed a considerable reduction in efficiency of crystals after neutron irradiation; for example, crystal STF126 efficiency decreased from (66 ± 2) % to (60 ± 2) % after exposing to 2.5 x 10^{21} neutrons/cm^2.

Extensive studies of Cherenkov detectors were carried out for the understanding of its sensor and electronics readouts to find a suitable alternative sensor for working in that environment. The detection of Cherenkov light produced by proton while passing through the fused silica; is currently performed in the UA9 apparatus by classical PMTs, which are placed relatively far from the detector because of high radiation. In the present work a Zinc Oxide (ZnO) sensor on Silicon substrate has been employed to test and characterize its possible use, having this material the ability to detect the UV-Vis light (Cherenkov light occurs in this range). We found, on the basis of preliminary tests, that ZnO Photo sensor has the ability to work under high radiation environment, as it hasn't shown any major changes or damages to the gamma (~ 1 MeV) and alpha radiations of ~ 5 MeV, this latter losing almost 99.9 % energy inside the compound. The only change that has been observed is the response and recovery times. These changes don't represent a major problem, and can be handled by using various shapes and thicknesses of this material. The rise and fall times for the photocurrent were measured as 22 ps and 8 ns also, showing that, as deposited, ZnO thin film photodetectors (metal–semiconductor–metal MSM etc..) can be used for applications needed for low light level (pulses of nanoseconds) detection and fast operation[69]. Although ZnO material appears very promising, the results obtained with gamma and alpha particle irradiations must be complemented with high energy neutron irradiation before using it as a sensor in high radiation areas.

In addition to ZnO, Silicon Photomultiplier (SiPM) was also tested and its signals analyzed for two main purposes:

(1) Due to its high Photon Detection Efficiency (PDE) and low response and recovery time, the SiPM can be also used as an alternative option to the current classical PMTs in Cherenkov at UA9.

(2) To go deep in acquiring and handling the signals from these sensors, as a starting point to realize a real time monitoring system in the framework of a future update of the Cherenkov detector at UA9. In particular, such a new system would unify the process of algorithm development and system implementation just as done in real time framework for Thomson scattering experiment [85]. An important feature of Real-Time Framework realized in the cited experiment is the possibility to configure accurately the deployment of an application by varying input and output data sources as well as parameters without recompiling the application.

This work provides a base for future investigations and upgrading of the detection techniques for real time monitoring of crystal based collimation systems in particle accelerators.

BIBLIOGRAPHY

1. STARK, J., et al., *JR STARK.* 1912.
2. Wille, K., *The physics of particle accelerators: an introduction*. 2000: Clarendon Press.
3. Le Duff, J. *Longitudinal beam dynamics in circular accelerators*. in *Cas 5 Cern Accelerator School 5 General Accelerator Physics Course*. 1992. Cern.
4. Taratin, A., *Particle channeling in a bent crystal.* PPN, 1998. **29**(5): p. 437-462.
5. Biryukov, V.M., Y.A. Chesnokov, and V.I. Kotov, *Crystal channeling and its application at high-energy accelerators*. 2013: Springer Science & Business Media.
6. Guidi, V., L. Lanzoni, and A. Mazzolari, *Study of anticlastic deformation in a silicon crystal for channeling experiments.* Journal of Applied Physics, 2010. **107**(11): p. 113534.
7. Baricordi, S., et al., *Shaping of silicon crystals for channelling experiments through anisotropic chemical etching.* Journal of Physics D: Applied Physics, 2008. **41**(24): p. 245501.
8. Caballero, R., et al., *Derivation of the Moliere simultaneous distribution between the deflection angle and the lateral displacement.*
9. Lindhard, J., M. Scharff, and H. Schiott, *K. Dan. Vidensk. Selsk, Mat.* Fys. Medd, 1963. **33**(1).
10. Mirarchi, D., W. Scandale, and S. Redaelli, *Crystal implementation in SixTrack for proton beams.* 2018.
11. Hasan, S., *Bent silicon crystals for the LHC collimation: studies with an ultrarelativistic proton beam*. 2007, Insubria U., Como.
12. Tsyganov, E., *Estimates of cooling and bending processes for charged particles penetration through a monocrystal, Fermilab preprint TM-682, Fermilab, Batavia, 1976.* Fermilab Preprint TM-684. Fermilab, Batavia, 1976.
13. Ivanov, Y.M., A. Petrunin, and V.V. Skorobogatov, *Observation of the elastic quasi-mosaicity effect in bent silicon single crystals.* Journal of Experimental and Theoretical Physics Letters, 2005. **81**(3): p. 99-101.
14. Chesnokov, Y.A., V. Maisheev, and I. Yazynin, *Volume capture and volume reflection of ultrarelativistic particles in bent single crystals.* arXiv preprint arXiv:0808.1486, 2008.
15. Taratin, A. and W. Scandale, *Volume reflection of high-energy protons in short bent crystals.* Nuclear Instruments and Methods in Physics Research Section B: Beam Interactions with Materials and Atoms, 2007. **262**(2): p. 340-347.
16. Scandale, W., et al., *Probability of inelastic nuclear interactions of high-energy protons in a bent crystal.* Nuclear Instruments and Methods in Physics Research Section B: Beam Interactions with Materials and Atoms, 2010. **268**(17-18): p. 2655-2659.
17. Scandale, W., et al., *Volume reflection dependence of 400 GeV/c protons on the bent crystal curvature.* Physical review letters, 2008. **101**(23): p. 234801.
18. Bagli, E., et al., *A topologically connected multistrip crystal for efficient steering of high-energy beam.* Journal of Instrumentation, 2012. **7**(04): p. P04002.
19. Mirarchi, D., *Crystal collimation for LHC*. 2015, Imperial College London.
20. Rossi, R., et al., *Crystal collimation cleaning measurements with proton beams in LHC*. 2016.
21. Scandale, W., et al., *First results on the SPS beam collimation with bent crystals.* Physics Letters B, 2010. **692**(2): p. 78-82.
22. Scandale, W., et al., *Optimization of the crystal assisted collimation of the SPS beam.* Physics Letters B, 2013. **726**(1-3): p. 182-186.
23. Redaelli, S., et al., *First observation of ion beam channeling in bent crystals at multi-TeV energies.* The European Physical Journal C, 2021. **81**(2): p. 1-7.

24. Scandale, W., et al., *Observation of channeling for 6500 GeV/c protons in the crystal assisted collimation setup for LHC.* Physics Letters B, 2016. **758**: p. 129-133.
25. Mirarchi, D., et al., *Design and implementation of a crystal collimation test stand at the Large Hadron Collider.* The European Physical Journal C, 2017. **77**(6): p. 1-13.
26. Biino, C., et al., *The influence of radiation damage on the deflection of high-energy beams in bent silicon crystals*. 1996.
27. Lechner, A. *Assessment of the thermo-mechanical response and damage to a silicon crystal subject to high-intensity beam impact*. 2014. tech. rep., UA9 Collaboration meeting.
28. Scandale, W., et al., *Beam steering performance of bent silicon crystals irradiated with high-intensity and high-energy protons.* The European Physical Journal C, 2019. **79**(11): p. 1-5.
29. Ahdida, C., et al., *SHiP Experiment-Progress Report*. 2019.
30. EDDA, G., K. CORNELIS, and I. EFTHYMIOPOULOS. *CERN, 1211 Geneva 23, Switzerland email: eddalgschwendtner (a) cern ch*. in *Astroparticle, Particle and Space Physics, Detectors and Medical Physics Applications: Proceedings of the 11th Conference, Villa Olmo, Como, Italy, 5-9 October 2009*. 2010. World Scientific.
31. Natochii, A., *Detectors developments for the UA9 experiment at the CERN SPS*. 2019, Paris Saclay.
32. Montesano, S. and W. Scandale. *Apparatus and experimental procedures to test crystal collimation*. in *Conf. Proc.* 2012.
33. Scandale, W., et al., *The UA9 experimental layout.* Journal of Instrumentation, 2011. **6**(10): p. T10002.
34. Piselli, E., et al. *CERN-SPS Wire Scanner impedance and wire heating studies*. in *Proceedings of IBIC2014*. 2014.
35. Pesaresi, M., et al., *Design and performance of a high rate, high angular resolution beam telescope used for crystal channeling studies.* Journal of Instrumentation, 2011. **6**(04): p. P04006.
36. French, M., et al., *Design and results from the APV25, a deep sub-micron CMOS front-end chip for the CMS tracker.* Nuclear Instruments and Methods in Physics Research Section A: Accelerators, Spectrometers, Detectors and Associated Equipment, 2001. **466**(2): p. 359-365.
37. Coughlan, J., et al., *The CMS tracker front-end driver.* 2003.
38. Fraser, M., et al., *Experimental results of crystal-assisted slow extraction at the SPS.* arXiv preprint arXiv:1707.05151, 2017.
39. Velotti, F., et al., *Reduction of resonant slow extraction losses with shadowing of septum wires by a bent crystal.* Proc. of IPAC’17, 2017.
40. fur Metallforshung, M., *Second Status Report on RD22.* 1994.
41. Afonin, A., et al., *High-efficiency beam extraction and collimation using channeling in very short bent crystals.* Physical review letters, 2001. **87**(9): p. 094802.
42. Carrigan Jr, R., et al., *Beam extraction studies at 900 GeV using a channeling crystal.* Physical Review Special Topics-Accelerators and Beams, 2002. **5**(4): p. 043501.
43. Dabagov, S., et al., *journal homepage: www. elsevier. com/locate/nimb.*
44. Taratin, A., *Particle channeling in a bent crys-.* Phys. Part. Nucl. 29(5), 437{462, 1998.
45. Scandale, W., et al., *Observation of focusing of 400 GeV/c proton beam with the help of bent crystals.* Physics letters B, 2014. **733**: p. 366-372.
46. Harden, F., et al. *Hiradmat: A facility beyond the realms of materials testing*. in *Journal of Physics: Conference Series*. 2019. IOP Publishing.
47. Lechner, A., et al. *Robustness test of a silicon strip crystal for crystal-assisted collimation studies in the LHC*. in *Conf. Proc.* 2013.
48. Zhovkovska, V., *Characterisation of the bent silicon crystals and study of the inelastic nuclear interactions of 180 GeV/c pions in bent crystals at the UA9 experiment*. 2018.

49. Zhovkovska, V., *Characterisation of the bent silicon crystals*. 2018.
50. Addesa, F.M., *In-vacuum Cherenkov light detectors for crystal-assisted beam manipulations*. INFN, Rome.
51. Gasior, M., et al., *Introduction to beam instrumentation and diagnostics.* arXiv preprint arXiv:1601.04907, 2016.
52. Laface, E., et al., *Crystal Collimation efficiency measured with the Medipix detector in SPS UA9 experiment*. 2010.
53. Taborelli, M., *Codification of surface cleanliness levels*. 2013, SOP-AS-01.
54. Puill, V., et al., *The CpFM, an in-vacuum Cherenkov beam monitor for UA9 at SPS.* Journal of Instrumentation, 2017. **12**(04): p. P04029.
55. Wigmans, R. and R. Wigmans, *Calorimetry: Energy measurement in particle physics*. Vol. 107. 2000: Oxford University Press.
56. Delagnes, E., *Documentation of the samlong chip.* 2011.
57. Breton, D. and J. Malmii, *WaveCatcher Family User's Manual.* 2017.
58. Lee, J.-H., K.-H. Ko, and B.-O. Park, *Electrical and optical properties of ZnO transparent conducting films by the sol–gel method.* Journal of crystal growth, 2003. **247**(1-2): p. 119-125.
59. Shohany, B.G. and A.K. Zak, *Doped ZnO nanostructures with selected elements-Structural, morphology and optical properties: A review.* Ceramics International, 2020. **46**(5): p. 5507-5520.
60. Wang, Z.L., *Zinc oxide nanostructures: growth, properties and applications.* Journal of physics: condensed matter, 2004. **16**(25): p. R829.
61. Boruah, B.D., *Zinc oxide ultraviolet photodetectors: rapid progress from conventional to self-powered photodetectors.* Nanoscale Advances, 2019. **1**(6): p. 2059-2085.
62. Caglar, M., Y. Caglar, and S. Ilican, *The determination of the thickness and optical constants of the ZnO crystalline thin film by using envelope method.* Journal of optoelectronics and advanced materials, 2006. **8**(4): p. 1410.
63. Yakuphanoglu, F., et al., *The effects of fluorine on the structural, surface morphology and optical properties of ZnO thin films.* Physica B: Condensed Matter, 2007. **394**(1): p. 86-92.
64. Van, L., M. Hong, and J. Ding, *Structural and magnetic property of Co-doped–ZnO thin films prepared by pulsed laser deposition.* Journal of Alloys and Compounds, 2008. **449**(1-2): p. 207-209.
65. Kind, H., et al., *Nanowire ultraviolet photodetectors and optical switches.* Advanced materials, 2002. **14**(2): p. 158-160.
66. Soci, C., et al., *ZnO nanowire UV photodetectors with high internal gain.* Nano letters, 2007. **7**(4): p. 1003-1009.
67. Zheng, L., et al., *Large scale, highly efficient and self-powered UV photodetectors enabled by all-solid-state n-TiO 2 nanowell/p-NiO mesoporous nanosheet heterojunctions.* Journal of Materials Chemistry C, 2016. **4**(42): p. 10032-10039.
68. Ismail, A., et al., *Effect of low dose-rate industrial Co-60 gamma irradiation on ZnO thin films: Structural and optical study.* Microelectronics Reliability, 2020. **104**: p. 113556.
69. Çalışkan, D., et al., *Low dark current and high speed ZnO metal–semiconductor–metal photodetector on SiO2/Si substrate.* Applied Physics Letters, 2014. **105**(16): p. 161108.
70. Yan-Liang, M., et al., *Properties study of ZnO: Ga crystal on pulsed radiation detections.* Chinese Physics C, 2010. **34**(3): p. 354.
71. Buzhan, P., et al., *The advanced study of silicon photomultiplier*, in *Advanced Technology and Particle Physics*. 2002, World Scientific. p. 717-728.
72. Renker, D., *Geiger-mode avalanche photodiodes, history, properties and problems.* Nuclear Instruments and Methods in Physics Research Section A: Accelerators, Spectrometers, Detectors and Associated Equipment, 2006. **567**(1): p. 48-56.

73. *Department 40 "elementary particle physics" Moscow Russia (2011). http://pc3k40.exp.mephi.ru/,*. Available from: webpage, http://pc3k40.exp.mephi.ru/,.
74. Ninković, J., et al., *SiMPl—Novel high QE photosensor.* Nuclear Instruments and Methods in Physics Research Section A: Accelerators, Spectrometers, Detectors and Associated Equipment, 2009. **610**(1): p. 142-144.
75. Degenhardt, C., et al. *The digital silicon photomultiplier—a novel sensor for the detection of scintillation light*. in *2009 IEEE Nuclear Science Symposium Conference Record (NSS/MIC)*. 2009. IEEE.
76. Piatek, S. *SiPM Hamamatsu Corporation & New Jersey Institute of Technology, Technical Note, October 7, 2016*
77. Light, S.s., *Introduction to SiPM,TECHNICAL NOTE, SensL*
78. Eckert, P., et al., *Characterisation studies of silicon photomultipliers.* Nuclear Instruments and Methods in Physics Research Section A: Accelerators, Spectrometers, Detectors and Associated Equipment, 2010. **620**(2-3): p. 217-226.
79. Hamamatsu, *MPPCs for Precision Measurement* 2016.
80. CAEN, *730 Digitizer Family 16/8 Ch. 14-bit 500 MS/s Digitizer CAEN Electronic Instrumentation*.
81. CoMPASS, C., *User Manual UM5960 CoMPASS Multiparametric DAQ Software for Physics Applications Rev. 14 2021*
82. Lacaita, A., et al., *Observation of avalanche propagation by multiplication assisted diffusion in p-n junctions.* Applied physics letters, 1990. **57**(5): p. 489-491.
83. Buzhan, P., et al., *Silicon photomultiplier and its possible applications.* Nuclear Instruments and Methods in Physics Research Section A: Accelerators, Spectrometers, Detectors and Associated Equipment, 2003. **504**(1-3): p. 48-52.
84. Albrow, M., et al., *Quartz Cherenkov counters for fast timing: QUARTIC.* Journal of Instrumentation, 2012. **7**(10): p. P10027.
85. Kadziela, M., et al., *Evaluation of the ITER Real-Time Framework for Data Acquisition and Processing from Pulsed Gigasample Digitizers.* Journal of Fusion Energy, 2020. **39**(5): p. 261-269.
86. Rossbach, J. and P. Schmueser, *Basic course on accelerator optics*. 1993, P00011673.

APPENDIX A
Solution of the Equation of Motion

In this section a general solution of equation of motion (eq 1.2) is derived. This equation explains the particle's trajectory in the magnetic lattice of the particle accelerator. To derive its solution let's consider the reference system in figure 2.1 first. Hence the pointing vector to the particle can be written as:

$$\vec{r} = \hat{r} + x\hat{x} + y\hat{y} \tag{A.1}$$

Here $\hat{x}$ and $\hat{y}$ are unit vectors related to particle along its path/trajectory. Considering a small rotation *dθ* in the horizontal plane, it can be written that:

$$d\hat{x} = d\theta\hat{s}\,, \quad d\hat{s} = -d\theta\hat{x}\,, \quad d\hat{y} = 0 \tag{A.2}$$

The length of path is given by:

$$\begin{aligned} \dot{\hat{x}} &= \frac{d\hat{x}}{d\theta}\frac{d\theta}{dt} = \hat{s}\frac{1}{R}\,\dot{s} \\ \dot{\hat{s}} &= \frac{d\hat{s}}{d\theta}\frac{d\theta}{dt} = -\hat{x}\frac{1}{R}\,\dot{s} \\ \dot{\hat{y}} &= 0 \end{aligned} \tag{A.3}$$

Where the system origin linked with the particle traveled by, $d\hat{r} = \hat{s}ds \Rightarrow \dot{\hat{r}} = \hat{s}\dot{s}$, Let us now calculate the first and second derivatives of vector pointing to the particle as follows:

$$\begin{aligned} \dot{r} &= \dot{\hat{r}} + \dot{x}\,\hat{x} + x\dot{\hat{x}} + \dot{y}\hat{y} + y\dot{\hat{y}} \\ \dot{r} &= \hat{s}\dot{s} + \dot{x}\hat{x} + \frac{1}{R}\dot{s}\hat{s} + \dot{y}\hat{y} \\ \dot{r} &= \dot{x}\hat{x} + \dot{y}\hat{y} + \left(1 + \frac{x}{R}\right)\hat{s}\dot{s} \end{aligned} \tag{A.4}$$

Following the same way it could be derived also that:

$$\ddot{\vec{r}} = \left[\ddot{x} - \left(1 + \frac{x}{R}\right)\frac{\dot{s}^2}{R}\right]\hat{x} + \ddot{y}\hat{y} + \left[\frac{2}{R}\dot{x}\dot{s} + \left(1 + \frac{x}{R}\right)\ddot{s}\right]\hat{s} \tag{A.5}$$

Along the orbit s the particle position has a unique value at any *t*, it is hereby the replacement of time derivative in orthogonal plane is possible as:

$$\begin{gathered}\dot{x} = \frac{dx}{ds}\frac{ds}{dt} = \acute{x}\dot{s} \\ \ddot{x} = x''\dot{s}^2 + \acute{x}\ddot{s}\end{gathered} \tag{A.6}$$

Therefore, equation A.4 and A.5 turn into:

$$\begin{gathered}\dot{r} = x'\dot{s}\hat{x} + y'\dot{s}\hat{y} + \left(1 + \frac{x}{R}\right)\dot{s}\hat{s} \\ \ddot{\vec{r}} = \left[x''\dot{s}^2 + x'\ddot{s} - \left(1 + \frac{x}{R}\right)\frac{\dot{s}^2}{R}\right]\hat{x} + (y''\dot{s}^2 + y'\ddot{s})\hat{y} + \left[\frac{2}{R}x'\dot{s}^2 + \left(1 + \frac{x}{R}\right)\ddot{s}\right]\hat{s}\end{gathered} \tag{A.7}$$

Thus equation 1.2 can be written as:

$$\ddot{\vec{r}} = \frac{e}{m}\begin{pmatrix} -\left(1 + \frac{x}{R}\right)\dot{s}B_y \\ \left(1 + \frac{x}{R}\right)\dot{s}B_x \\ x'\dot{s}B_y + y'\dot{s}B_x \end{pmatrix} \tag{A.8}$$

The effect of magnetic field on longitudinal velocity of the particles can be neglected because of their ultra relativistic regimes, therefore by combining A.7 and A.8 we get:

$$\begin{gathered}x''\dot{s}^2 + x'\ddot{s} - \left(1 + \frac{x}{R}\right)\frac{\dot{s}^2}{R} = -\frac{e}{m}\left(1 + \frac{x}{R}\right)\dot{s}B_y \\ y''\dot{s}^2 + y'\ddot{s} = \frac{e}{m}\left(1 + \frac{x}{R}\right)\dot{s}B_x\end{gathered} \tag{A.9}$$

Assuming slow variation of longitudinal velocity ($\ddot{s} \approx 0$) and using $p = mv$, equation A.9 can be written as:

$$\begin{gathered}x'' - \left(1 + \frac{x}{R}\right)\frac{1}{R} = -\frac{e}{p}\frac{v}{\dot{s}}\left(1 + \frac{x}{R}\right)B_y \\ y'' = \frac{e}{p}\frac{v}{\dot{s}}\left(1 + \frac{x}{R}\right)B_x\end{gathered} \tag{A.10}$$

By Geometry:

$$v = \left(1 + \frac{x}{R}\right)\dot{s} \tag{A.11}$$

Suppose a particle got little deviation from its nominal momentum $= p_0 + \Delta p$, it is possible to write in first approximation:

$$\frac{1}{p} = \frac{1}{p_0}\left(1 + \frac{\Delta p}{p_0}\right) \tag{A.12}$$

By expanding the magnetic field in series, and using only the linear terms, it is feasible to write in first estimation:

$$\begin{aligned} \frac{e}{p_0}B_y &= \frac{1}{R} - kx, \\ \frac{e}{p_0}B_x &= -ky \end{aligned} \tag{A.13}$$

Here we assumed that dipole fields are acting in horizontal plane, 1/R and k are the energy invariant dipole and quadrupole strength respectively [86]. Therefore, using the relation in equations A.11, A.12 and A.13 in equation A.10, it gives:

$$\begin{gathered} x'' - \left(1 + \frac{x}{R}\right)\frac{1}{R} = -\left(\frac{1}{R} - kx\right)\left(1 + \frac{x}{R}\right)^2\left(1 + \frac{\Delta p}{p_0}\right) \\ y'' = -ky\left(1 + \frac{x}{R}\right)^2\left(1 + \frac{\Delta p}{p_0}\right) \end{gathered} \tag{A.14}$$

As x<<R, y<<R and Δp/p << 1, therefore we can consider only linear terms in first approximation gives:

$$\begin{gathered} x''(s) + \left(\frac{1}{R^2(s)} - k(s)\right)x(s) = \frac{1}{R(s)}\frac{\Delta p}{p_0} \\ y''(s) + \ k(s)y(s) = 0 \end{gathered} \tag{A.15}$$

Equations in A.15 are the general solutions of the equation of motion of a particle in a circular machine and for particles with the nominal momentum, turn into equation 1.4

Acknowledgements

I acknowledge the generous financial support from the **Ministry of University Research Italy** and the **Department of Physics, Federico II University of Naples** for this research project.

I am extremely thankful to my supervisors, Prof. Pasquale Arpaia and Prof. Giovanni La Rana for their supervision, patience, and regular support. I have benefited greatly from their wealth of knowledge and painstaking editing. I am extremely grateful to them for accepting me as a student and keeping believe in me over the years. I will always remain in debt to both of them.

Many thanks to Prof. Salvatore Capozziello (PhD Coordinator), a humble man with an intellectual personality who always available to support and guide to me in all administrative issues.

A special thanks to the section of **INFN Napoli** and to Prof. Emanuele Vardaci for providing me with a well furnished laboratory to carry out my research activities during the critical period of the corona emergency.

I am very thankful to the **UA9 Experiment at CERN,** especially Prof. Walter Scandale and Dr. Francesca Galluccio who provided me the opportunity to learn and work in the outstanding environment of UA9 experiment at CERN. I really appreciate the efforts of Francesca Galluccio to solve all my research and administrative related issues with a smiling face. I am very grateful to my advisors, Marco Grattini and Roberto Rossi who always answered very politely and guided me almost in all analysis procedures.

I am fortunate to have been a part of Instrumentation and Measurement Lab, **IST Lisbon Portugal** for which I am really thankful to Prof. Pedro Ramos.

I also acknowledge **STMicroelectronics Arzano Naples** for providing me with the internship opportunity. Here, I have to mention my advisor, Mr. David and my colleague, Mr. Giuseppe Caiazzo for their continuous backup and help to understand the concept of microcontrollers.

My heartfelt thanks to my friend Dr. Muhammad Hilal (Postdoc South Korea) for his sincere support and in time back up to complete this task within time.

I would like to thank Engr. Umberto Cesaro and Engr. Nicola Mocaldi, Department of Electrical Engineering and Informations Technology, from the first day of my PhD to the accomplishment of this task; these two persons were my nightmare that used to push me forward.

A special thanks to all friends that I am lucky to have, which I cannot list here because too much space would be needed, and given my memory I could forget someone for sure. However, a particular acknowledgement goes to Abid Ali, who encouraged me when I felt disheartened and stood by my side through the entire journey of this PhD.

Most importantly, I am grateful to my family and their unconditional, unequivocal, and loving support. No doubt, this PhD would not be possible without the support of my beloved brothers, Naqeem uddin, Naseer Uddin and Noor ul Islam. My mother, my wife and my sisters' prayers and support made me confident and hence today, Alhamdulillah, I have the result of all these people's efforts in the shape of this degree, love you all.

Zahoor ul Islam